VIRTUAL CONSTRAINT CONTROL OF POWERED PROSTHETIC LEGS:

UNIFYING THE GAIT CYCLE

by

David Quintero

APPROVED BY SUPERVISORY COMMITTEE:

____

Robert D. Gregg, IV, Chair

____

Nicholas Fey

____

James P. Schmiedeler

____

Mark W. Spong

____

Stephen Yurkovich

To Sofía and Olivia

VIRTUAL CONSTRAINT CONTROL OF POWERED PROSTHETIC LEGS: UNIFYING THE GAIT CYCLE

by

DAVID QUINTERO, BS, MS

DISSERTATION

Presented to the Faculty of

The University of Texas at Dallas

in Partial Fulfillment

of the Requirements

for the Degree of

DOCTOR OF PHILOSOPHY IN

MECHANICAL ENGINEERING

THE UNIVERSITY OF TEXAS AT DALLAS

May 2018

ACKNOWLEDGMENTS

This is my last section to write as part of this dissertation and in my opinion it is one of the most important. It has been over a decade since setting a goal to complete a doctoral dissertation, and there are a number of people I need to acknowledge that have impacted my life to get me to this point. First, I want to thank my family for their continuous love and support in helping me reach my goals. I have to acknowledge my mother for always instilling in me the importance of an education, for that is one thing no one can take away from you as a person. My father who throughout my life has taught me the importance of a hard work ethic that led me to achieving this milestone by witnessing you work day in day out at your job without complaints. It gave me the belief that I can achieve my own career goals no matter the challenges ahead. A part of this dissertation work is dedicated to you. I would like to thank my sister for helping me through all the tribulations I have experienced in my life, and when I am down she has been there to do all she can to help me get back up and keep pushing forward. She has always exemplified unselfishness in thinking of others before herself. Without a doubt I wouldn't be able to go through this doctoral program without your help and support, so I thank you.

I wouldn't be able to complete this dissertation work in the robotics field without key individuals. During my time at Stanford, I have to first thank Mark Cutkosky and Yong-Lae Park for taking me in as a young man who had no experience in robotics and for just giving me an opportunity to be involved in research. In life that goes a long way. Then to Kenneth Salisbury and Vic Scheinman for their helpful discussions about robotics and making me believe I can contribute to this field. I also want to thank Reuben Brewer and Kevin Loewke for taking the time to answer questions I had on research and showing me the ropes to becoming a robotics researcher. I was like a sponge during our Friday coffee shop breaks from the lab, where I would listen deeply to our discussions about research and being a roboticist. I want to acknowledge Machiel Van der Loos for introducing me to rehabilitation robotics, which defined my area of interest within the robotics field. Lastly, I want to thank Günter Niemeyer for exemplifying what it means to be a great teacher, which led me to my enjoyment of studying controls.

At The University of Texas at Dallas, I absolutely need to acknowledge my advisor Robert Gregg for not just his guidance in research but his continuous support for allowing me to get to this point in completing my dissertation. I smile thinking back of our paths crossing which led me to your lab and realize the milestones we were able to accomplish in research over the years. To my committee members for their encouragement and providing me their time to discuss about my research. A special thanks to Mathukumalli Vidyasagar ("Sagar") for our long, friendly discussions about the past, present, and future of controls. I could listen to you for hours upon end passing down your knowledge on controls, which gave me great appreciation for the impact you have made within the field. To members of Robo𝕋ec Lab for making the lab environment enjoyable to work at; specifically to Aykut Satici, Hasan Poonawala, and Olalekan Ogunmolu for having great discussions of what entails for the future of robotics and how do we fit in. To members of the Locomotor Control Systems Laboratory for their support during my research work. Especially to Anne Martin for teaching me the standard for how to be a professional researcher and to be successful at it. To Dario Villarreal for his work on the phase variable and helping with human subject experiments. But more importantly when I hit hardships during my work, he always put faith in me that I would overcome the challenges and continue forward. To the lab research engineers over years: Yonathan Chatzinoff, Aaron Plauche, and Christopher Nesler. When the robotic leg was down, your technical support made experiments possible. Thank you to all the lab interns I had the pleasure to work with and mentor over the years. One specifically is Daniel Lambert for whom I could rely on in getting things done during crunch time. I owe a great deal for his time and effort in helping to get the leg ready for experiments. It wouldn't be possible without his help. I see a bright future ahead of him, and I hope he learned a lot from being part of the lab as I have learned a lot from him. I would like to acknowledge collaborators at UTSouthwestern Medical Center, Susan Kapp and Leslie Gray, for assisting with amputee subject experiments and giving me insight for how our work can translate to a clinical application.

Por fin a mi señora. Tu amor y apoyo durante mi programa de doctorado me dio el empujòn final para hacer esto. Gracias por todo lo que has hecho por mi. No podrìa completar este viaje sin ti.

April 2018

VIRTUAL CONSTRAINT CONTROL OF POWERED PROSTHETIC LEGS:

UNIFYING THE GAIT CYCLE

David Quintero, PhD
The University of Texas at Dallas, 2018

Supervising Professor: Robert D. Gregg, IV, Chair

The lower limb amputee population is gradually increasing, primarily due to complications from vascular diseases. The vast majority of lower limb amputees use mechanically passive prosthetic legs, which are unable to provide energy input at the joints and can only dissipate energy during locomotion. To improve amputee gait, powered prosthetic legs are in development. Several control methods have been proposed for these devices, but almost all of them divide the gait cycle into multiple, sequential periods with different controllers. This results in many patient-specific control parameters and switching rules that must be tuned for a specific ambulation mode, such as a desired walking speed or slope. The different periods of gait could potentially be unified over the entire gait cycle by virtual kinematic constraints that are enforced using a torque control scheme. The prosthetic control method proposed as part of this dissertation work unifies the different periods of gait through virtual constraints that are driven by a human-inspired phase variable. A phase variable is a kinematic quantity corresponding to an unactuated degree of freedom that evolves monotonically during steady walking, thus representing the progression through the gait cycle. The unified controller was designed systematically by method of virtual constraints, which was implemented within an amputee biped walker model for different walking speeds. To validate this control strategy even further, a powered knee-ankle prosthesis was designed and built during the course of

this dissertation work for experimental validation. The mechanical design and real-time control of the powered prosthesis is presented. Experiments were conducted with multiple above-knee amputee subjects walking across various speeds and inclines, while no control parameters were tuned. This verified that our unified control scheme can work seamlessly and efficiently for multiple amputee users, and also, for different ambulation modes without retuning the controller. Furthermore, this work has taken a step forward to providing a solution of the technical challenges for powered knee-ankle prostheses to be used in a clinical setting. An intuitive clinical user interface was developed for clinicians to change the prosthesis control based on their clinical insight and expertise. We performed a case study with a clinician adjusting the virtual constraint design on the prosthesis, which resulted in improvement of the amputee's gait symmetry using our control strategy.

TABLE OF CONTENTS

ACKNOWLEDGMENTS v

ABSTRACT viii

LIST OF FIGURES xiii

LIST OF TABLES xxii

CHAPTER 1 INTRODUCTION 1

1.1 Background of Prosthetic Leg Technology 2

1.2 Control Strategies for Powered Prosthetics 4

1.3 Dissertation Outline 6

CHAPTER 2 PROSTHESIS UNIFIED PHASE-BASED CONTROL DESIGN AND SIMULATION 8

2.1 Method of Virtual Constraints in Biped Robots 9

2.2 Unified Virtual Constraint Control 10

2.3 Prosthesis Control for an Amputee Biped Model 13

2.3.1 Amputee Biped Model 13

2.3.2 Partial Feedback Linearization for a Powered Prosthesis 16

2.3.3 Perspective of Piecewise HZD vs Unified Virtual Constraints 19

2.3.4 Simulation Results 21

2.3.5 Discussion 27

CHAPTER 3 DESIGN AND REAL-TIME CONTROL OF A POWERED PROSTHESIS 29

3.1 Prosthesis Mechanical Design 30

3.2 Prosthesis Electronics & Sensing 34

3.3 Real-Time Control System Architecture 36

3.3.1 Real-Time Human-Inspired Phase Variable Algorithms 38

3.3.2 Preliminary Results on Real-Time Human-Inspired Phase Variable . . 45

3.3.3 UTD Leg Control Loops 50

3.3.4 From Rhythmic to Volitional Control 57

3.4 Prosthesis Performance Evaluation 61

3.4.1 Benchtop Performance 61
3.4.2 Preliminary Able-Bodied Subject Experiments with Fixed Virtual Constraints 66
3.4.3 Gait Speed Classifier Experiments 70
3.4.4 Discussion 73
CHAPTER 4 TRANSFEMORAL AMPUTEE SUBJECT EXPERIMENTS USING UNIFIED CONTROL ON A POWERED PROSTHESIS 76
4.1 Initial Setup and Tuning 77
4.1.1 Experimental Setup and Protocol 78
4.2 Amputee Experimental Results 79
4.2.1 Normal Level-Ground Walking 80
4.2.2 Variable Speeds 83
4.2.3 Variable Inclines 86
4.3 Discussion 89
4.3.1 Advantages of the Control Method 89
4.3.2 Limitations of the Study 91
CHAPTER 5 DEVELOPMENT AND CASE STUDY OF A CLINICAL INTERFACE 93
5.1 Overview of a Clinician Control Interface 93
5.1.1 Manipulation of Desired Joint Kinematics 94
5.1.2 Initialization of Interface Joint Kinematics 96
5.1.3 Features for Virtual Constraint Manipulation 97
5.1.4 Safety Considerations 100
5.2 Example of Clinical Tuning for a Powered Prosthesis 101
5.2.1 Initialization Setup 101
5.2.2 Joint Kinematic Adjustment 102
5.2.3 Clinical Tuned Control Implementation 106
5.3 Clinical Tuning Experiment 107
5.3.1 Experimental Setup & Protocol 107
5.3.2 Experimental Results 109
5.4 Discussion 120

5.4.1 Convergence of Spatial-Temporal parameters increases gait fluidity . 120
5.4.2 Clinical tuning influences limb loading 120
5.4.3 Compensation moves from the ankle to the hip 121
5.4.4 Metrics for overall gait pathology 122
CHAPTER 6 CONCLUSION 124
APPENDIX A UTD LEG 1 DESIGN BUILD OF MATERIAL 127
APPENDIX B UTD LEG 1 KINEMATIC ANALYSIS 129
APPENDIX C UTD LEG 1 MATLAB/SIMULINK CONTROL SYSTEM 134
REFERENCES 143
BIOGRAPHICAL SKETCH 154
CURRICULUM VITAE

LIST OF FIGURES

1.1 Hanger Limb [1] 4

1.2 Mechanical Above-Knee Prosthesis [74] 4

1.3 Ottobock C-Leg [73] 4

1.4 Vanderbilt Leg [91] 4

2.1 Schematic of the unilateral, transfemoral amputee model [61]. The prosthesis is shown in black and the human segments is shown in gray. The generalized coordinates used in the model are indicated with q terms. Angle q_1 is unactuated and angles q_{2-6} have ideal actuators. 14

2.2 Virtual constraints by DFT and Bézier polynomial (Bez) for the knee (left) and ankle (right) during normal human walking (N). Because Bézier virtual constraints are defined in a piecewise manner, their normalized phase variable goes from 0 to 1 twice per stride. For comparison, the Bézier phase variable has been scaled and shifted to match the DFT phase variable. The DFT function repeats the gait cycle for phase variable values $s_P < 0$ and $s_P > 1$, i.e., the ranges of $-0.5 \leq s_P < 0$ and $0.5 \leq s_P < 1$ are identical. In contrast, the piecewise Bézier polynomials for stance (St) and swing (Sw) diverge to undesirable trajectories on both sides of the design region. 22

2.3 The simulated trajectories of the prosthetic knee (left) and ankle (right) with both the DFT and Bézier controllers for three different walking speeds (matched with the human speed) plotted against the DFT normalized phase variable. The DFT and Bézier response is almost identical in all cases. 24

2.4 The simulated phase portrait for the prosthetic knee (left) and ankle (right) for three different walking speeds (matched with human) with the DFT and Bézier controllers. The DFT gaits closely match the reference Bézier gaits. As expected, the greatest deviations occur near impacts. The rolling motion of the curved foot results in a slightly larger ankle orbit for slow walking than normal walking with both controllers. 24

2.5 The simulated tracking errors of the prosthetic knee (left) and ankle (right) for both the unified DFT and piecewise Bézier controllers during steady-state walking with mixed speeds. The normal matched speed error is also shown for comparison. Both controllers have similar error at the start of the stance period (phase variable near 0), but the DFT controller has significantly less error at the start of the swing period (phase variable near 0.5). Note: N-S = normal walking (prosthesis) and slow walking (human), N-N = normal walking (prosthesis) and normal walking (human), and N-F = normal walking (prosthesis) and fast walking (human). . . 27

2.6 The simulated torques of the prosthetic knee (left) and ankle (right) for the mixed case of the human at slow speed and the prosthesis at normal speed with the Bézier feedback linearizing controller (N-S Bez-Fk Lin), the DFT feedback linearizing controller (N-S DFT-Fk Lin), and the DFT impedance controller (N-S DFT-Imp). The torques of the impedance controller approximate the feedback linearizing controllers throughout the gait cycle. The torque impulses after impacts are caused by discontinuities in velocity from the impulsive impact model, which do not occur during human walking. 28

3.1 The UTD powered knee-ankle prosthesis: CAD rendering and key components (left) and manufactured version (right). A timing belt connects each motor to a linear ball screw, which the ball screw translational motion drives a lever arm to produce a joint torque. 32

3.2 A CAD rendering of the FSR placement between two 3D printed neoprene rubber material located above the prosthesis' foot female pyramid adapter and below the ankle's lever arm mount. 35

3.3 UTD Powered Prosthesis Leg Embedded System routing of the offboard power source to the motor drivers and sensors on the leg. Sensor feedback signals are routed to the dSPACE processor for real-time control computation. Hardware safety components are included during leg operation with power solid-state relays and an operator Emergency Stop (E-Stop) button. 36

3.4 Photo of human subject walking on a treadmill while wearing an IMU sensor on the thigh with a sagittal plane orientation. Thigh angle measurement follows the righthand rule. 39

3.5 A depiction of the phase variable $\varphi(t)$ measured from the circular orbit (thick green line) with a polar radius r (dashed black line) within the thigh phase portrait $(\theta_x(t), \dot{\theta}_y(t))$ coordinates. The ellipse (red line) displays the predefined minimum and maximum X/Y coordinates (black dots) as well as its length of semi-axes c and d. A schematic for how start and stop detection method from Section 3.3.1 is used for a sequence of events. If a subject were to stop walking, the signal travels off the circular orbit (1. Stop path, dotted green line) to inside the ellipse (2. Stop point, red dot) near the origin. When the subject decides to continue walking then the orbital path continues (3. Continue path, dash-dot blue line) to the last recorded phase variable value to complete the stride along the circular orbit. 41

3.6 Top: the thigh angle (Raw) measured by the IMU (dotted blue line) compared against two filtered options: 1) a second order Butterworth (Butter) low-pass filter with a cutoff frequency of 5 Hz (dashed red line) and the Interpolating (Interp) filter method (solid green line). Bottom: the thigh velocity (numerically differentiated thigh angle) and the two filtered options. Signal disturbances from ground impact are observed in the thigh velocity (e.g., $t \approx 1.3$ and 2.6 seconds). The Interpolating filter provides a more smooth signal than the Butterworth filter. Data is from 3 mph treadmill speed test. 47

3.7 The raw thigh orbit (Raw) compared to the interpolated filtered, shifted/scaled thigh orbit (Interp + Shift/Scale) in the phase plane for 20 continuous strides at 3 mph. Applying the shift and scale algorithm produces a circular orbit shape, in contrast to the raw non-circular orbit. 48

3.8 The normalized phase variable $\varphi_{norm}(t)$ vs. time across various treadmill speeds (1-9 mph) for 20 consecutive gait strides. Each phase variable curve represents the mean for that particular speed with ± 1 standard deviation (shaded gray region, difficult to observe due to small variance). Toe-off is marked (red star) at the moment when the minimum thigh angle occurred. Horizontal red dashed lines give the lower and upper bounds of these events across the various speeds, demonstrating the ability of the phase variable to predict these events despite differences in timing. The slower speeds (1-3 mph) have a nonlinear phase trajectory due to a longer time duration in stance compared to swing, whereas faster speeds ($\geq$ 4 mph) produce a linear phase trajectory due to a more even stance/swing split [116]. 50

3.9 The phase portrait of $\dot{\theta}_y(t)$ vs. $\theta_x(t)$ across various treadmill speeds (1-9 mph) each having 20 consecutive gait strides. The polar radius r can be correlated to the subject's gait speed. Speeds $\leq$ 4mph produced a circular orbit from 0 to 2π (i.e., 0% to 100% gait cycle). At 5 mph, the subject transitioned from fast walking to running, where more forceful ground impacts can be observed in the IMU measurements due to the flight phase. This produced a non-circular form after impact with intersection of other orbits at different speeds, as shown in the first quadrant for 5-6 mph. 51

3.10 Treadmill speed vs. mean polar radius r (Data) with regression line $v(r)$ (Fit). Note the error bars (horizontal blue lines) are ± 1 standard deviation from the mean (red dots). 52

3.11 The control architecture for the prosthesis comprises an outer and inner loop. The outer loop computes the desired joint torques (Eq. 3.10) needed to enforce the virtual constraints (Eq. 3.9) based on the mechanical phase variable (Eq. 3.7). The desired knee torque $\tau_{\mathrm{d}k}$ is converted to current commands for the knee motor driver (u_k^A) using an inverse model of the knee actuator. The current commands for the ankle motor driver (u_a^A) are computed by an inner loop (Eq. 3.13) that provides closed-loop torque control with a friction compensator. 52

3.12 A phase portrait of the thigh angle ϕ and its integral Φ with the thigh phase angle ϑ measured about the circular orbit to determining the phase variable. Each axis crossing of the phase angle will contain either a max or min value of the thigh angle or its integral to determining the phase variable shift and scale factors (see Eq. 3.7). 54

3.13 Phase plane of the thigh angle $\phi_x(t)$ vs. its integral $\Phi_y(t)$ during prosthetic leg experiments (Section 3.4.2). The phase plane has been scaled by z and shifted by (γ, Γ) to achieve a circular orbit across the stride, which improves the linearity of the phase variable $\vartheta(t)$. 54

3.14 Phase variable block diagram of each major component computed. The raw hip angle measured ($\phi(t)$) from the IMU is feed through an integrator ($\Phi(t)$) with a reset condition for when the circular orbit has completed within the phase portrait. Then the parameters ($\phi(t), \Phi(t)$) are sent to compute the minimum/maximum and the shift/scale values from the phase portrait x-y axis . The atan2 function is evaluated ($\vartheta(t)$) prior to the safety subsystems of the monotonic filter and start/stop detection algorithms, which then outputs the normalized phase variable s_h. 55

3.15 A finite state machine for using a piecewise phase variable for performing stance or swing for either forward or backward walking. The blue circles refers to Eq. 3.14 and yellow circles refers to Eq. 3.15. Between each state there are transition rules that consist in evaluating s_{st} about ankle push-off threshold s_{po}, FSR sensing for ground foot contact (HI) or no contact (LO), or thigh velocity $\dot{q}_h$ changing sign during preswing. 59

3.16 An example representation of a Viscous friction with Coulomb friction versus velocity effect (left). Actual motor torque versus motor rate performed on the Maxon motor (right) closely resembles the friction force element model on the left. 62

3.17 Left Column: Knee (top) and Ankle (bottom) angular position step response. The dotted black line is the desired command at 0.1745 radians and the solid red line is the joint actuation response output. Right Column: Knee (top) and Ankle (bottom) angular position step duty cycle response. The dotted black line is the desired step commands at multiple positions and the solid red line is the joint actuation response output. 63

3.18 Left: Commanded versus measured angular position of a sinusoidal frequency sweep for the ankle joint. The pink dashed line is the desired command and the black solid line is the joint actuation response output. Right: Frequency spectrum analysis between the commanded signal and the measured signal for the ankle joint. 64

3.19 Empirical results of closed-loop frequency response of UTD Leg 1 ankle (left) and knee (right). 65

3.20 Photo of able-bodied human subject walking on the powered prosthesis through a leg-bypass adapter during treadmill experiment. The IMU can be seen attached to a red mount on the bypass adapter. 66

3.21 The normalized phase variable over raw time per stride for 40 continuous strides at various walking speeds (1 to 3 mph). The phase variable is monotonic and approximately linear for all strides, where the slope of the trajectory depends on the walking speed. Flat regions can be observed between 0 and 0.4 sec in a few trajectories, which are the result of a zero-order hold to enforce monotonicity during non-steady walking motions (i.e., the first few steps after starting from rest). 68

3.22 The normalized phase variable over normalized time per stride at various walking speeds (1 to 3 mph). The average trajectory (blue solid line) and ±1 standard deviation (shaded region) are computed across 40 continuous strides. The phase variable is strictly monotonic and approximately linear across the gait cycle. . . 69

3.23 The desired joint trajectory and the virtual constraint by DFT with $K = 10$ (see Eq.2.6) for the knee (left) and ankle (right) with normal walking (NW) speed for an entire gait cycle. The reference data from [116] is indicated with solid lines and the virtual constraint is indicated with broken lines. Note, the knee angle is defined from the thigh to the shank and the ankle angle is defined from the shank to the foot (minus 90 deg). Both angles follow the right-hand rule. 70

3.24 Joint kinematics of the prosthetic knee (top) and ankle (bottom) over the phase variable at various walking speeds (1.0 to 3.0 mph). The black dashed line is the average commanded angle for each joint. The red solid line is the average measured angle for each joint. The shaded regions represent ±1 standard deviation about the mean. The averages and standard deviations are taken over 40 continuous strides. The control system reasonably tracked the commanded angles from the virtual constraints, which were designed from healthy human data in Fig. 3.23. 71

3.25 Joint kinematics of the prosthetic knee (top) and ankle (bottom) over normalized time at various walking speeds (1.0 to 3.0 mph). The black dashed line is the average commanded angle for each joint. The red solid line is the average measured angle for each joint. The shaded regions represent ±1 standard deviation about the mean. The averages and standard deviations are taken over 40 continuous strides. 71

3.26 The commanded motor currents from the controller for the knee (top) and ankle (bottom) over the phase variable at various walking speeds (1.0 to 3.0 mph). The knee requires the most current during the swing period (phase variable between 0.6 to 1.0), and the ankle current peaks during late stance (phase variable between 0.5 to 0.6) as powered push-off injects energy to propel the prosthetic leg into swing motion. Note, push-off occurs around phase variable of 0.6. 72

3.27 Prosthesis phase variable vs. time for a consecutive sequence of strides at slow (SW, 1.5 mph), normal (NW, 2.0 mph), and fast (FW, 2.5 mph) speeds with the autospeed classifier. The mean SW, NW, and FW phase trajectories (thick lines) are shown for reference. 74

3.28 Prosthetic joint angles for a consecutive sequence of strides at slow (SW, 1.5 mph), normal (NW, 2.0 mph), and fast (FW, 2.5 mph) speeds with the autospeed classifier. The mean SW, NW, and FW joint trajectories (thick lines) are shown for reference. 74

4.1 Photo of transfemoral amputee subject wearing the powered knee-ankle prosthesis. The IMU sensor is mounted on the pylon between the residual limb socket and the prosthetic knee joint (in the sagittal plane). 78

4.2 Phase portrait of the prosthetic leg (measured joint angular positions versus velocities) over 20 consecutive strides of steady-state, level-ground walking at the comfortable speed (about 2.0 mph) for amputee subjects TF01 (a), TF02 (b), and TF03 (c), compared with averaged able-bodied data (AB) [116]. Note that the prosthetic joints follow similar orbits to the able-bodied data. 80

4.3 Powered prosthesis joint kinematics/kinetics for TF01 level-ground walking at 2.0 mph, averaged over 20 consecutive strides with ±1 standard deviation shown by shaded regions. The commanded (Cmd) and measured (2.0 mph) joint angles are shown over normalized time (a–b) and over the phase variable (c–d). The estimated joint torques (e–f) and powers (g–h) are normalized by subject mass and compared with averaged able-bodied data (AB) over the phase variable [116]. The knee torque is estimated with the measured motor current and the knee actuator model, and the ankle torque is estimated with the measured linear force and ankle kinematic model (Fig. 3.11). The phase variable over time (i) is strictly monotonic and nearly linear, where the most variance occurs during early and mid stance. Box plots of mechanical work per stride (j) show the median (red line), 25th percentile (bottom of box), 75th percentile (top of box), distribution bounds (black whiskers), and outliers (red plus markers). Ankle work is positive, knee work is negative, and total work is near zero as expected from able-bodied walking [116]. 81

4.4 Powered prosthesis joint kinematics/kinetics for TF02 level-ground walking at multiple speeds with slow, normal, and fast kinematics, averaged over 15-20 consecutive strides. The measured joint angles over phase (a–b) demonstrate that faster speeds produce a larger range of motion. The estimated joint torques (c–d) and powers (e–f) are normalized by subject mass and plotted over phase, demonstrating more torque and power at faster speeds. The phase variable over time (g) is monotonic with a steeper slope (i.e., shorter time duration) for faster speeds. Box plots of mechanical work per stride (h) show the median (red line), 25th percentile (bottom of box), 75th percentile (top of box), distribution bounds (black whiskers), and outliers (red plus markers) for each speed condition. Ankle work and total work increase with walking speed as expected [116]. 84

4.5 Powered prosthesis joint kinematics/kinetics for TF02 level-ground walking at multiple speeds with fixed normal-speed kinematics, averaged over 15-20 consecutive strides. The measured joint angles (a–b), normalized joint torques (c–d), and normalized joint powers (e–f) are more appropriate for slow and normal speeds than the fastest speed. The phase variable over time (g) adapts appropriately with all speeds, having a steeper slope (i.e., shorter time duration) for faster speeds. Box plots of mechanical work per stride (h) show the median (red line), 25th percentile (bottom of box), 75th percentile (top of box), distribution bounds (black whiskers), and outliers (red plus markers) for each speed condition. Ankle work and total work are appropriate for slow and normal walking but insufficient for the fastest speed [116]. 85

4.6 Powered prosthesis joint kinematics/kinetics for TF02 walking on multiple ground slopes at 2.0 mph with slope-specific kinematics, averaged over 10-20 consecutive strides. The measured joint angles over phase (a–b) exhibit more stance ankle dorsiflexion and stance knee flexion/extension for steeper inclines. The estimated joint torques (c–d) and powers (e–f) are normalized by subject mass and plotted over phase. The phase variable over time (g) has a consistent, linear trajectory across ground slopes (i.e., similar time durations). Box plots of mechanical work per stride (h) show the median (red line), 25th percentile (bottom of box), 75th percentile (top of box), distribution bounds (black whiskers), and outliers (red plus markers) for each slope condition. 87

4.7 Powered prosthesis joint kinematics/kinetics for TF03 walking on 7.5 deg incline at 2.0 mph, averaged over 9 consecutive strides with ± 1 standard deviation shown by shaded regions. The commanded (Cmd) and measured (7.5 deg) joint angles are shown over normalized time (a–b) and over the phase variable (c–d). The commanded signals have some variance at the end of the stride due to the use of a rate limiter as a safety feature. The estimated joint torques (e–f) and powers (g–h) are normalized by subject mass and shown over the phase variable. The phase variable over time (i) is strictly monotonic and nearly linear. Box plots of mechanical work per stride (j) show the median (red line), 25th percentile (bottom of box), 75th percentile (top of box), distribution bounds (black whiskers), and outliers (red plus markers). 88

5.1 Clinician control interface with default knee (top) and ankle (bottom) angular position trajectories with respect to gait cycle, fitted to Catmull-Rom spline from Winter's dataset for normal walking [116]. Dragging the control points (blue dots) smoothly adjusts the joint trajectories. Commonly used features such as Save and Patient Information are easily accessible through large buttons. 101

5.2 Patient information dialog displays the subject ID, gender, height, weight, age, time post-amputation, amputated leg, and leg measurements. 102

5.3 CCI Help window guides the user through common actions, such as editing trajectories and analyzing the kinematics. 103

5.4 Flow diagram for the clinician graphical user interface. Setup begins with either opening an existing patient file or creating a new file with Patient Information. The user adds or deletes control points and adjusts the trajectories as desired. When finished tuning, the user saves the modified trajectories and exports the design for virtual constraint control to the powered prosthesis. 104

5.5 Quick tuning buttons allow for easily adjusting ankle push-off and knee flexion during swing. The plus (+) and minus (-) buttons increase and decrease the amplitude of the angular position, and the left (<) and right (>) buttons move the transition earlier and later in the gait cycle, both respectively. 104

5.6 Case study of increasing ankle push-off and shifting earlier in the gait cycle. The modified ankle angular position (top blue dashed line) has more push-off range occurring earlier than the original trajectory (top red solid line). The modified ankle angular velocity (bottom blue dashed line) has a larger magnitude than the original angular velocity (bottom red solid line) as a result of the increased push-off amplitude. 105

5.7 Sample user adjustment beyond safety limits. The user drags the cursor (pointer) to move the original control point (black circle) to a new location (red cross). Safety features restrict the modification to the furthest safe control point location (blue circle with yellow center). 106

5.8 Block diagram of clinician input into the joint angle trajectories design process. Clinician visual feedback and other comparison metrics as described in Section 5.1.3 allow the tuning process to reach better performance for the patient. 106

5.9 Photo of a transfemoral amputee subject wearing the powered knee-ankle prosthesis. Reflective markers placed on the amputee's lower limbs to collect kinematic data during walking trials from a motion capture system. 107

5.10 Clinician joint kinematic design for Controller 1 (Ctrlr 1) in blue dotted line and Controller 2 (Ctrlr 2) in red solid line versus the Baseline controller in black dashed line over phase variable. The knee (top) trajectories had very minor adjustment with the Baseline and Controller 1 remained the same (on top of each other), and Controller 2 was slightly shifted in phase to the left for earlier swing. The ankle (bottom) trajectories each had some variance from Baseline controller with increase in ankle push-off between $s_h = 0.5$ to 0.78, where Controller 2 had the largest push-off difference and earlier start of push-off occurring at $s_h = 0.42$. Both controllers have an increase in plantarflexion to have the foot give higher loading response ($s_h = 0.075$) after heel strike ($s_h = 0.0$). All these trajectories were exported from the CCI tool into the prosthesis virtual constraint controller for experimentation. 112

5.11 Powered prosthesis measured signals over consecutive strides for a forward walking trial when the amputee is using the Baseline controller in black dashed line and the clinician Controller 2 (Ctrlr 2) in blue solid line. Baseline and Controller 2 were separate test trials, so the results are compared by having their time sequence aligned with respect to their first phase variable measurement (see Fig. 5.12). The knee angular position (top left) for both controllers have similar responses with the exception of a phase shift, likely from the increase ankle push-off (top right) for Controller 2. FSM states (bottom left) shows that each state was achieved in sequence with some states occurring in longer duration. Thigh position (bottom right) gives larger magnitude when ankle push-off is increased using Controller 2 ($t = 2.25$ to 3.1 s). 113

5.12 The phase variable measurement over time shows Controller 2 (Ctrlr 2) compared to Baseline occurring faster with respect to time as the amputee is getting aided assistance from increase in ankle push-off along gait. 114

5.13 This figure shows vertical normalized GRF for Controller 2 with respect to units of Body Weight (BW). The blue solid line refers to the prosthetic side (Controller 2 Pros.) and in black dashed line is the intact side (Controller 2 Intact). The initial sharp peak on the prosthetic side is due to impact force before loading and the relative peak on the intact side at $t = 1.0$ s corresponds with the subject's vault. The difference in duration is a good representation of the difference in stance time between the prosthetic and intact limbs. 116

5.14 Intact leg foot progression angle in the sagittal plane over a gait cycle that identifies the peak angle of plantarflexion (thin black lines) in the single support period (shaded region) using the powered leg to illustrate the method of vaulting quantification. The subject is trying to create as much space as possible for toe clearance during contralateral swing period. 117

B.1 UTD Leg 1 schematic for declaring mechanism parameters of angles and lengths to derive kinematic equations. 130

C.1 UTD Leg 1 Control System: Model Main 135

C.2 UTD Leg 1 Control System: Phase Variable Main 135

C.3 UTD Leg 1 Control System: Phase Variable Subsystems 136

C.4 UTD Leg 1 Control System: Virtual Constraint DFT Coefficients 137

C.5 UTD Leg 1 Control System: Virtual Constraint Outer and Inner Control Loops 137

C.6 UTD Leg 1 Control System: User Interface Control Options 138

C.7 UTD Leg 1 Control System: Joint Torque Estimation Main 139

C.8 UTD Leg 1 Control System: Joint Torque Lever Arm Angle Estimate 139

C.9 UTD Leg 1 Control System: Sensors Main 140

C.10 UTD Leg 1 Control System: Power Safety 140

C.11 UTD Leg 1 Control System: Piecewise Phase Variable Finite State Machine . . 141

C.12 UTD Leg 1 Control System: dSPACE Control Interface 141

C.13 UTD Leg 1 Control System: dSPACE Measurement Interface 142

LIST OF TABLES

2.1 Fitting Statistics of DFT Design 20

2.2 Maximum Eigenvalues with Unified Prosthetic Controller 26

3.1 Powered Prosthesis Design Specifications 31

3.2 Step Response Characteristics for UTD Prosthetic Leg 63

4.1 Characteristics of Transfemoral Amputee Subjects 77

4.2 Ranges of Activities Performed by Transfemoral Amputee Subjects 77

5.1 Spatial-Temporal Parameter Results 114

5.2 Analysis of Ground Reaction Forces 115

5.3 Quantifying Gait Pathology 118

5.4 Overall Gait Performance Evaluation 119

A.1 UTD Leg 1 Bill of Materials 127

A.1 Continued UTD Leg 1 Bill of Materials 128

CHAPTER 1

INTRODUCTION

The United States of America (USA) has a higher rate of lower extremity amputations compared to other developed countries [90]. In fact, the number of lower limb amputations is expected to increase in the USA to 58,000 per year by 2030 [21]. Dysvascular disease, either by atherosclerosis or with diabetes, is a systematic disease and increases more for older population [13]. About 64% of the amputees from this older population (65 years or older) were amputated from having these dysvascular diseases [127]. Two main types of lower limb amputees are transfemoral (above-knee) and transtibial (below-knee). Nearly all use a non-powered, mechanically passive prosthesis for daily locomotion activities. In general, when using a passive prosthesis the lower limb amputee gait is less stable [68] and requires more metabolic energy than able-bodied gait [24]. This limits an amputee's ability to efficiently perform various ambulation modes, such as walking at variable speeds or on slopes. Furthermore, the biomechanical compensations required to walk with these passive devices generally cause joint discomfort and back pain during daily usage [101, 96, 88].

A lower limb prosthesis that provides input power at the joints from a powered actuation system could potentially restore the biomechanical function of the missing leg muscles. This could enable improved amputee gait for a variety of daily activities, such as walking at variable speeds more efficiently. Fortunately, powered prosthetic legs are in development [109, 80]. These powered devices require highly sophisticated control strategies, particularly for multi-joint legs, to perform various activities in a natural and safe manner [109]. Generally these control schemes are designed for specific ambulation modes (e.g., level ground walking, ramp ascent/descent, stair ascent/descent, etc.), where the controller needs to be retuned per amputee subject. Furthermore, the majority of the controllers currently in development have a time-variant control scheme, where they consist of multiple controllers along the gait cycle with switching rules between them. When perturbed, this control approach could switch to the wrong state and use the wrong controller, which may increase an amputee's risk of falling. This dissertation work will explore using a continuous phase-based controller that is unified over the gait cycle and the advantages and disadvantages it has performing different locomotion tasks.

1.1 Background of Prosthetic Leg Technology

The evolution of lower extremity prosthesis technology dates back to the 19th century. The aftermath from the American Civil War produced a large number of amputees, which increased the demand for prosthetic devices. A confederate soldier named James E. Hanger, who was one of the first reported amputees of the war who later created his own prosthesis known as the Hanger Limb [41]. This prosthesis was manufactured from barrel staves and metal that featured hinged joints at the knee and ankle (Fig. 1.1) [5]. In the 1970's, the design scope of a lower limb prosthesis focused on reducing mechanical friction of the components and allowing the task of walking less straining for the user during gait. This carried forward in the 1990's as prosthetic legs were designed from lighter metallic materials and composites. Majority of prosthetic knee systems were a single hinge joint mechanical design (Fig. 1.2) [74]. The prosthetic ankle-foot generally consisted of a non-articulated foot, such as the Solid-Ankle Cushioned Heel (SACH) Foot [103]. The prosthetic foot was molded from neoprene or urethane that made it light with minimal energy release for propulsion.

From the late 1990's to today prosthetic legs became much lighter, made of plastic, aluminum and composite materials to provide amputees more functionality for prosthetic devices. The release of a microprocessor knee provided above-knee amputees more capability to mimic the movements of the knee for more of a natural looking gait. The microprocessor knee has a pneumatic/hydraulic cylinder to add resistance to the joint, while software and sensors are used to adjust the damping of the knee joint depending where the amputee is along the gait. During the stance period, the knee joint has resistance increased to restrict flexion, while during the swing period resistance is lowered to allow knee flexion and extension for ground clearance until the next heel strike. One of the most popular microprocessor knees is the Ottobock C-Leg (Fig. 1.3) [73]. The prosthetic ankle-foot has advanced from new materials with using carbon fiber springs to store and release energy as the foot transitions towards push-off. The longer the carbon fiber foot is the more energy it can store that can increase foot propulsion during push-off. A common prosthetic ankle-foot is the Freedom Innovations Sierra [22].

In general, commercially available prostheses have difficulty in performing various ambulation modes. Inclines and stairs are challenging to perform, particularly stairs as an amputee tends to go step by step, one stair at a time. Similarly for inclines of ramp ascent, the knee would collapse due to the body weight of the individual. The underlying issue is the knee and ankle joints do not provide active power to perform biomechanical functions for different ambulation modes. This encourages current and future development of powered prosthesis to improve amputee's quality of life [27].

Lower limb powered prostheses can consist of an active power ankle only, knee only, or both knee and ankle. Actuator designs can vary from planetary gears, linear ball screws, timing belts, harmonic drives, etc. with brushless direct current (BLDC) motors [80]. There are knee prostheses that use a hybrid design approach by a spring between a motor and a linear ball screw known as a Series Elastic Actuator (SEA) [82] with a clutch transmission [93]. It provides the advantage of the SEA to store energy in a spring and reduce motor peak torque, while the clutch produced low electric power consumption from the motor while still providing the necessary reaction torque. There are ankle prostheses that use SEA design as well [6, 8]. For a multi-joint (knee-ankle) prosthesis, Vanderbilt University has designed a family of knee-ankle prostheses, with their most recent version shown in Fig. 1.4 [58]. Other institutions have developed powered knee-ankle prostheses with different actuation systems for transfemoral amputees [23, 81, 117]. The main design objective is to mimic the muscle activation produced about the joints of an intact leg. However, these prostheses likely require sophisticated control strategies to reject disturbances and allow amputees to ambulate in a natural and safe manner [109].

Figure 1.1. Hanger Limb [1]

Figure 1.2. Mechanical Above-Knee Prosthesis [74]

Figure 1.3. Ottobock C-Leg [73]

Figure 1.4. Vanderbilt Leg [91]

1.2 Control Strategies for Powered Prosthetics

Powered prosthetic legs that provide actuation at the joints could potentially improve amputee gait. To date, there have been several control methods implemented on actuated lower limb prostheses. The study of biomechanics classifies human gait into specific intervals over the gait stride (e.g., heel strike, midstance, toe off, etc.) [77]. Generally, powered prosthesis controllers mimic this ideology by using a different controller for each period of gait based on predefined transition criteria. In the most common approach, a finite state machine switches between joint impedance controllers based on the period of gait [104, 18, 6, 18, 108]. However, the Proportional-Derivative (PD) gains and switching rules for each period must be carefully tuned for each user and activity, such as ascending/descending ramps [105] or stairs [59]. These multiple controllers with many control parameters can potentially require hours of tuning to adapt a powered prosthetic leg for just a single lower limb amputee [100]. Another impedance-based approach is to encode artificial reflexes from a neuromuscular model in the controller [6]. This method still requires a finite state machine to adjust the control policy or parameters depending on the gait period. In considering safety, finite state machines can also end up in the wrong state after a perturbation, resulting in unexpected leg behavior that can lead to a fall.

These different periods of gait could potentially be unified by virtual kinematic constraints that are enforced using a torque control scheme [115, 102, 64, 89, 10, 40, 69, 125, 39, 32, 61, 63]. Virtual constraints typically define desired joint trajectories as polynomial functions of a mechanical phasing variable. A phase variable is a time-invariant, kinematic quantity corresponding to an unactuated degree of freedom that evolves monotonically during steady walking, thus representing the progression through the gait cycle. This phase-based control method was originally developed to control underactuated bipedal robots, such as MABEL [102], ERNIE [64], and ATRIAS [89]. If the biped is pushed forward (or backward), the phase variable increases (or decreases), which in turn speeds up (or slows down) the step. The controller is therefore able to automatically react to disturbances, which increases the robustness of the gait. This would be advantageous for a prosthesis controller by allowing the prosthesis to react to disturbances in a predictable manner that may resemble the response of a human leg [33, 113].

Previous work at the Rehabilitation Institute of Chicago developed a virtual constraint controller for a transfemoral (above-knee) powered prosthesis that used the center of pressure

(COP) as the phase variable during the stance period [34, 32, 31]. Because the COP is only defined during stance, the prosthesis switched to a sequential impedance-based controller during swing. Recently, the virtual constraint control method was extended to the swing period of the prosthesis, although separate controllers were still defined for the stance and swing periods [61]. This dissertation extends powered prosthesis phase-based control even further by designing virtual constraints that are unified for continuous control over the entire gait cycle.

1.3 Dissertation Outline

This dissertation covers multiple stages of a research investigation from design and control of a powered prosthesis to experimentation and verification of the theoretical work. Chapter 2 discusses the theoretical derivation of the prosthesis controller and validation in simulation. Furthermore, a background information is given for the methods of virtual constraints used in bipedal robots and how the control strategy can be applicable for powered prosthesis. The design of virtual constraints unified over gait for a powered prosthesis is validated using a amputee biped model simulator to show stability with human interaction disturbance from varying speeds. Moreover, the unified controller is compared with a piecewise controller used in biped walkers. Chapter 3 describes the design and control implementation of The University of Texas at Dallas (UTD) first generation powered prosthesis. Design requirements are presented to meet able-bodied normal walking conditions from both a kinematic and kinetic standpoint. The real-time control system is also described to explain the phase-based control and its implementation with only onboard sensors. Then a discussion of a control approach when performing non-rhythmic movement when using the powered prosthesis. Chapter 4 provides the experimental results for both able-bodied and amputee subjects. A series of tests were performed over treadmill that consist of different ambulation modes between various speeds and slopes. The test results will demonstrate the powered prosthesis using our unified control approach allow subjects to ambulate in a similar manner to healthy able-bodied subject, while requiring minimal control tuning. Chapter 5 shows a clinical user interface designed to allow clinicians in adjusting the prosthesis' virtual constraints for both knee and ankle based on their own professional expertise. This provides the capability of a multi-joint powered prosthesis to be used in a clinical setting with our control scheme. Chapter 6 gives a conclusion of this dissertation effort and suggests future work to continue the research of unified control for powered prostheses.

CHAPTER 2

PROSTHESIS UNIFIED PHASE-BASED CONTROL DESIGN AND SIMULATION

Control theory research of biped robots has been performed over numerous decades since the early 1960s. Biped robots can be considered as biomimetic systems, where their purpose is to imitate human locomotion. They are meant to ambulate over level ground, rough terrain, ramps, stairs, etc. Several control strategies have been implemented for biped robot locomotion for those various ambulation scenarios. Two main categories for implementing bipedal locomotion control can be categorized as either time-variant or time-invariant control. The method of virtual constraints for biped robots is a time-invariant, phase-based control strategy that has produced stable walking and running with the use of a mechanical variable also known as a phase variable. Biped robots can continuously progress over gait with parametric functions over a phase variable for each joint to produce locomotion. This emerging control technology from the biped robot community can have advantages for use in lower limb prosthetics to replicate the biomimetic behavior for an amputee's gait.

The method of virtual constraints for biped robots will be discussed in Section 2.1. Then Section 2.2 will derive the design of virtual constraints for the purpose of controlling a powered knee-ankle prosthesis unified over the gait cycle. This provides a novel control strategy for amputee locomotion, which is the baseline control scheme of this dissertation work. Section 2.3 derives transfemoral amputee biped model used in simulation and applying feedback linearization to the output function for each joint, which is implemented in the biped simulation model. An investigation of the unified control approach versus an established virtual constraint method (i.e., Hybrid Zero Dynamics) is also evaluated to understand the validity of this method for powered prosthesis control.

2.1 Method of Virtual Constraints in Biped Robots

The method of virtual constraints is a time-invariant, feedback control technique that incorporates synchronization of kinematic motion constraints on a system instead of relying on hardware or physical constraints, such as complicated coupling of linkages [115]. The feedback controllers are based on the system's state variables in which virtual constraints are defined as output functions to synchronize the motion of the joints that are driven towards zero in the form of

$$y_i = q_i - h_i^d(\varphi_i(q_i)), \tag{2.1}$$

where q_i is the generalized coordinates, h_i^d is the desired functions for the generalized coordinates, and $\varphi_i(q_i)$ is parameterized variable that the virtual constraint is constrained. The variable $\varphi_i(q_i)$ is a function of the system states, which is known as the phase variable. The phase variable is a time-invariant, kinematic quantity that captures the motion of an unactuated degree of freedom and monotonically increases during stride. Designing virtual constraints for a biped robot, the progression of the biped through the stride is driven by the phase variable. If the biped is pushed forward (or backward), the phase variable increases (or decreases), which in turn speeds up (or slows down) the joint patterns. It is advantageous of applying virtual constraints for biped walking as the kinematics are parameterized over phase and not time.

Virtual constraints for biped robots are currently defined in a piecewise manner, separated by stance-to-swing transitions. These transitions are typically modeled as discontinuous impact events, which are considered when designing the piecewise virtual constraints. The method of Hybrid Zero Dynamics (HZD) encodes joint trajectories into polynomial functions that are invariant to these impact events (i.e., *hybrid invariant*), allowing a restriction of the hybrid dynamical system to the lower-dimensional HZD for stability analysis [115]. For a biped robot having sensory information and control actuation for both legs and at the hip, experimental implementation in biped robots such as RABBIT, MABEL, and ATRIAS have been proven successful [12, 102, 89]. However, the control architecture generally switches among event-based of individual controllers that can lead to stability issues from unexpected disturbances [55, 75, 118]. Applying these control techniques for powered prosthetics with humans in the loop, these individual controllers over the gait cycle can potentially lead to fails. Therefore, designing virtual constraint controllers with entire unification of the gait cycle can potentially reduce the risk of unwanted behavior response as compared to switching between different controllers.

2.2 Unified Virtual Constraint Control[1]

Partial unification of the gait cycle and its provable stability properties have motivated recent work in virtual constraint control of powered prosthetic legs [32, 61, 63], which similarly define separate controllers for the stance and swing periods. Humans move in a smooth, continuous manner over a periodic gait cycle. This smooth periodicity is lost across the discrete transitions of a finite state machine, even one that separates only stance and swing. To enable better control of powered prostheses, we propose a new class of virtual constraints that continuously parameterize periodic joint patterns is proposed based on the Discrete Fourier Transformation (DFT) [72]. These virtual constraints are defined from reduced-order frequency representations of the desired joint trajectories. Piecewise HZD polynomials for the knee and ankle are converted into unified DFT functions to leverage the provable stability properties of HZD while respecting the continuous, periodic nature of human walking. The DFT virtual constraints unify prosthetic control within the gait cycle and across gait cycles by repeating periodically over the phase variable.

[1]

Previous attempts at a phase-based control of powered prosthetic and orthotic devices have used data-driven joint patterns and/or a single actuator. The powered prosthetic ankle in [45] tracks able-bodied human data as a function of a tibia-based phase angle throughout the gait cycle. Our approach differs by defining a torque control law to enforce HZD-inspired virtual constraints, which are easily generated for multiple joints and tasks with provable stability properties [115, 61, 63]. The hip exoskeleton in [53] uses a phase variable to determine when to inject or dissipate energy in the gait cycle, which may not be sufficient to replicate joint kinematics in a prosthesis application. In contrast, virtual constraints produce the desired kinematics in the absence of biological limb motion.

In general, virtual constraints are time-invariant and depend on a phase variable that is unactuated and monotonic [115]. We require the phase variable to be monotonic over the complete stride in order to parameterize a joint's complete kinematic pattern. For this work, the phase variable was chosen as the horizontal hip position q_x (see Fig. 2.1) measured relative to a coordinate frame created at the impact transition from human contralateral stance to prosthesis stance. Other options for the phase variable could also be considered in this framework [113, 112]. For convenience the phase variable $\theta_P(q_P) = q_x$ was normalized between 0 and 1 using

$$s_P(\theta_P(q_P)) = \frac{\theta_P - \theta_P^+}{\theta_P^- - \theta_P^+}, \tag{2.2}$$

where the '+' signifies the start of the stance period for the prosthetic leg and the '$-$' indicates the end of its swing period. The variable s_P is equivalent representation to the phase variable φ_i defined in the general form from Eq. 2.1.

Taking advantage of the periodic kinematics observed in human gait [116], the method of DFT can be used to define a unified virtual constraint for each joint. Let $x[n]$ be a discrete signal representing N equally spaced samples of a desired joint trajectory over the phase variable. The DFT is a linear transformation of $x[n]$ into its discrete frequency components

$$X[k] = \sum_{n=0}^{N-1} x[n] W_N^{kn}, \quad k = 0, 1, ..., N-1 \tag{2.3}$$

where $W_N = e^{-j(2\pi/N)}$ [72]. Because the signal $x[n]$ is periodic, there are a finite number of discrete frequencies. This signal can then be reconstructed using Fourier Interpolation:

$$x[n] = \frac{1}{N} \sum_{k=0}^{N-1} X[k] W_N^{-kn}, \quad n = 0, 1, ..., N-1, \tag{2.4}$$

where $X[k] = \mathrm{Re}\{X[k]\} + j\,\mathrm{Im}\{X[k]\}$ and $W_N^{-kn} = \mathrm{Re}\{W_N^{-kn}\} + j\,\mathrm{Im}\{W_N^{-kn}\}$ in standard complex form. Because the joint kinematic signals are real numbers, only the real part of $x[n]$ remains after substitution of $X[k]$ and W_N^{-kn} in Eq. 2.4 (see [72]). Moreover, the signal reconstruction only requires frequency terms from $k = 0$ to $N/2$ (the Nyquist sampling frequency), beyond which the magnitudes of $X[k]$ and $X[N-k]$ are equal. This results in the following exact representation of the original sampled joint trajectory:

$$\begin{aligned} x[n] = {} & \frac{1}{2}\alpha_0 + \sum_{k=1}^{\frac{N}{2}-1} \Big[\alpha_k \,\mathrm{Re}\{W_N^{-kn}\} - \beta_k \,\mathrm{Im}\{W_N^{-kn}\}\Big] \\ & + \frac{1}{2}\alpha_{\frac{N}{2}} \,\mathrm{Re}\{W_N^{-\frac{N}{2}n}\}, \quad n = 0, 1, ..., N-1, \end{aligned} \tag{2.5}$$

where $\alpha_k = 2\,\mathrm{Re}\{X[k]\} \in \mathbb{R}$ and $\beta_k = 2\,\mathrm{Im}\{X[k]\} \in \mathbb{R}$ are the scalar coefficients based on the original signal.

The Fourier Interpolation in Eq. 2.5 is used to parameterize the trajectory function h_P^d in Eq. 2.11 for the entire stride. After computing the coefficients α_k and β_k from a desired joint trajectory (to be specified later), Eq. 2.5 is expressed as a summation of sinusoids using Euler's relationship ($e^{\pm j\Omega} = \cos\Omega \pm j\sin\Omega$) in W_N to obtain

$$h_P^d(s_P) = \frac{1}{2}\alpha_0 + \frac{1}{2}\alpha_{\frac{N}{2}} \cos(\pi N s_P) + \sum_{k=1}^{K} \Big[\alpha_k \cos(\Omega_k s_P) - \beta_k \sin(\Omega_k s_P)\Big], \tag{2.6}$$

where $\Omega_k = 2\pi k$ and K is the total number of frequencies (up to $N/2$) used to parameterize the virtual constraint. Eq. 2.6 h_P^d is inserted into Eq. 2.1 to define the virtual constraint output and it is unified over the gait cycle from the declared phase variable s_P as control for a powered prosthesis. Because Eq. 2.6 is composed of sine and cosine functions, the resulting virtual constraints are inherently periodic across the phase variable with a period of one.

2.3 Prosthesis Control for an Amputee Biped Model[2]

To validate the control approach using unified virtual constraints an amputee biped model was utilized. A rigid, multi-link biped model is derived, where the equation of motions aid in incorporating the nonlinear control technique of partial feedback linearization. Then an investigation on the method of virtual constraints by DFT versus piecewise HZD control using Bézier is compared to evaluate their advantages and disadvantage between them. Lastly, biped simulation results is described using these control approaches to understand the outcome and their significance for prosthesis control. Both matched and mixed walking speed controllers between the prosthesis and the human intact leg is simulated to act as a form of perturbation to the biped walker. Stability analysis is characterized using Poincaré section. A realistic control law to the prosthesis using an impedance controller is performed to simulate actual implementation of the control strategy to the physical system.

2.3.1 Amputee Biped Model

Consider the case of a unilateral, transfemoral amputee walking with a powered knee-ankle prosthesis. The planar biped model (Fig. 2.1) consists of seven leg segments plus a point mass at the hip to represent the upper body as in [61, 63]. The thigh and shank segments are modeled using rigid links with mass and inertia. Model parameters are given in [63]. The full model is divided into a prosthesis subsystem consisting of the prosthetic thigh, shank, and foot, and a human subsystem consisting of the contralateral thigh, shank, and foot, the residual thigh on the amputated side, and the point mass at the hip. It is assumed that the prosthetic thigh and residual human thigh are rigidly attached, so the interaction forces between them are equal and opposite. Rather than model all of the contact phases and

---

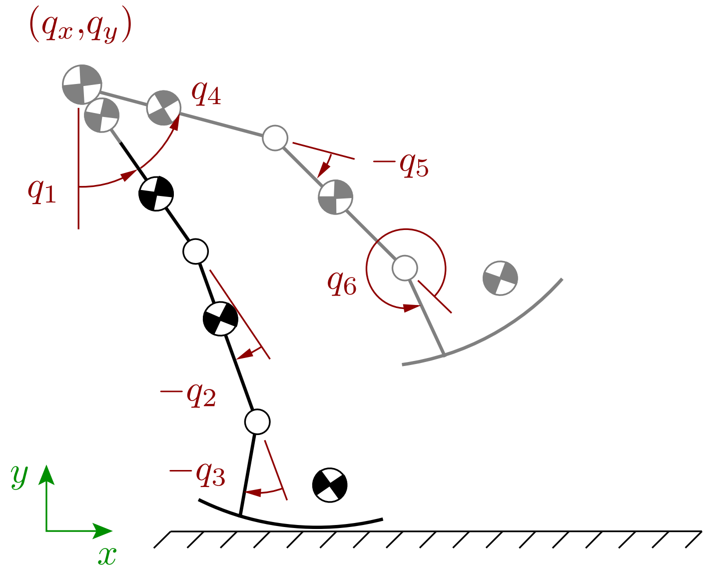

Figure 2.1. Schematic of the unilateral, transfemoral amputee model [61]. The prosthesis is shown in black and the human segments is shown in gray. The generalized coordinates used in the model are indicated with q terms. Angle q_1 is unactuated and angles q_{2-6} have ideal actuators.[3]

degrees of freedom of the foot, the function of the foot and ankle is modeled continuously using a circular foot [43, 42] plus an ankle joint to capture the stance ankle's positive work [65]. This foot model assumes rolling point contact, about which there is zero moment, so the ground reaction forces only contain tangential and normal components. Moreover, because the foot rolls without slip, the absolute angle q_1 is unactuated.

To describe the position and velocity of the biped, each subsystem has its own set of generalized coordinates. The configuration of each subsystem is described by the unactuated angle q_1, the Cartesian coordinates (q_x, q_y) of the hip, and the relative angles of the actuated joints. The actuated joint angles for the entire biped are q_2 to q_6. Thus, the generalized coordinates are $q_P = [q_1, q_2, q_3, q_x, q_y]^T$ for the prosthesis and $q_H = [q_1, q_4, q_5, q_6, q_x, q_y]^T$ for the human. Moreover, ideal actuators produce joint torques $u_P = [u_2, u_3]^T$ for the prosthesis and $u_H = [u_4, u_5, u_6]^T$ for the human.

For simulation, a stride starts just after the transition from contralateral stance to prosthesis stance and proceeds through the prosthesis stance period, an impact event, the contralateral stance period, and a second impact. The two stance periods can be modeled with continuous, second-order differential equations, and the two impact periods can be modeled using an algebraic mapping that relates the state of the biped at the instant before impact to the state of the biped after impact.

The equations of motion during the single-support period for each subsystem can written as [61, 63]

$$M_i\ddot{q}_i + C_i\dot{q}_i + N_i - E_i^T G_i = B_i u_i + J_i^T F, \tag{2.7}$$

where subscript i indicates the subsystem (P for the prosthesis and H for the human), q_i are the subsystem coordinates, M_i is the inertia matrix, C_i is the matrix containing the centripetal and Coriolis terms, N_i contains the gravity terms, E_i is a contact constraint matrix, G_i is the two-dimensional vector of the ground reaction forces, B_i relates the input torques to the generalized coordinates, J_i is the Jacobian matrix relating the socket interaction forces to the generalized coordinates, and F is the three-dimensional vector of interaction forces.

Solving for $\ddot{q}_i$ from the equations of motion (Eq. 2.7) gives

$$\begin{aligned}\ddot{q}_i = {} & M_i^{-1}(-C_i\dot{q}_i - N_i) + M_i^{-1}B_i u_i + M_i^{-1}J_i^T F \\ & + M_i^{-1}E_i^T G_i.\end{aligned} \tag{2.8}$$

Eq. 2.8 can also be written as a first-order state-space realization of the nonlinear system:

$$\dot{x}_i = f_i(x_i) + g_i(x_i)u_i + p_i(x_i)F + r_i(x_i)G_i, \tag{2.9}$$

where

$$x_i = \begin{bmatrix} q_i \\ \dot{q}_i \end{bmatrix}, \qquad f_i(x) = \begin{bmatrix} \dot{q}_i \\ -M_i^{-1}(C_i\dot{q}_i + N_i) \end{bmatrix},$$

$$g_i(x) = \begin{bmatrix} 0 \\ M_i^{-1} B_i \end{bmatrix}, \qquad p_i(x) = \begin{bmatrix} 0 \\ M_i^{-1} J_i^T \end{bmatrix},$$

$$r_i(x) = \begin{bmatrix} 0 \\ M_i^{-1} E_i^T \end{bmatrix}.$$

The generalized coordinates x_i are the states for the first-order nonlinear system (Eq. 2.9) with $f_i(x)$, $g_i(x)$, $p_i(x)$ and $r_i(x)$ as the vector field functions defining the full dynamic system.

The impacts can be modeled using equations of the form

$$q_i^+ \ = \ q_i^-, \qquad \dot{q}_i^+ \ = \ A_i \dot{q}_i^- + \Lambda_i \mathcal{F}, \tag{2.10}$$

where $\mathcal{F}$ is the socket interaction impulse that depends on the pre-impact state of both subsystems, and A_i and Λ_i are known matrices [61]. The superscripts '$-$' and '$+$' refers to the instants before and after impact, respectively.

2.3.2 Partial Feedback Linearization for a Powered Prosthesis

Virtual constraints encode the desired motions of actuated variables in output functions to be zeroed through control [115]:

$$y_{ij} = h_{ij}(q_i) = H_{0i} q_i - h_{ij}^d(\theta_i(q_i)), \tag{2.11}$$

where h_{ij} is a vector-valued function to be zeroed, H_{0i} is a matrix that maps the generalized coordinates to the actuated angles, h_{ij}^d is a vector-valued function of the desired joint angles (specifically the prosthetic knee q_2 and ankle q_3), and θ_i is the phase variable. The subscript j indicates which leg is in stance, with P indicating that the prosthesis is in stance and C indicating that the contralateral/human leg is in stance (and that the prosthesis is in swing). For the human, a separate output function is defined for the prosthesis single-support period and for the contralateral single-support period, and h^d_{Hj} is encoded using polynomials as in [61]. For the prosthesis, a single, unified output function h_P is defined for the entire stride, i.e., both the stance and swing periods of the prosthesis.

Various torque control methods can be utilized to regulate virtual constraint outputs. Bipedal robots typically enforce virtual constraints using partial (i.e., input-output) feedback linearization [115], which has appealing theoretical properties including exponential convergence [50], reduced-order stability analysis [115], and robustness to model errors [102]. For most of this simulation study, both the prosthesis and the human are controlled using feedback linearization [61, 32]. Note, however, that the prosthesis controller does not depend on the form of the human controller.

The first step in deriving the feedback linearizing controller is differentiating Eq. 2.11 twice and substituting in the equations of motion (Eq. 2.7) for $\ddot{q}_i$ to obtain the output dynamics [61]

$$\ddot{y}_{ij} = L^2_{f_i} h_{ij} + L_{g_i} L_{f_i} h_{ij} \cdot u_i + L_{p_i} L_{f_i} h_{ij} \cdot F + L_{r_i} L_{f_i} h_{ij} \cdot G_i, \tag{2.12}$$

where Lie derivative notation [50] has been used.[4] These terms are given by

$$\begin{aligned}
L^2_{f_i} h_{ij} &= \frac{\partial}{\partial q_i}\left(\frac{\partial h_{ij}}{\partial q_i}\dot{q}_i\right)\dot{q}_i - \frac{\partial h_{ij}}{\partial q_i} M_i^{-1}(C_i \dot{q}_i + N_i), \\
L_{g_i} L_{f_i} h_{ij} &= \frac{\partial h_{ij}}{\partial q_i} M_i^{-1} B_i, \quad L_{p_i} L_{f_i} h_{ij} = \frac{\partial h_{ij}}{\partial q_i} M_i^{-1} J_i^T \\
L_{r_i} L_{f_i} h_{ij} &= \frac{\partial h_{ij}}{\partial q_i} M_i^{-1} E_i^T.
\end{aligned}$$

The nonlinearities in the output dynamics are canceled by setting the desired output dynamics to $\ddot{y}_{ij} = v_{ij}$, for some PD controller v_{ij}, and solving for the required input torques:

$$u_{ij} = \alpha_{ij} + \beta_{ij} \cdot F + \gamma_{ij} \cdot G_i, \tag{2.13}$$

[4] A Lie derivative $L_f h := \nabla_x h \cdot f$ represents the change of a function $h(x)$ along a vector field $f(x)$. A second-order Lie derivative $L^2_f h = \nabla_x (L_f h) \cdot f$.

where F and G_i are known through measurement, and

$$\alpha_{ij} = [L_{g_i} L_{f_i} h_{ij}]^{-1}(v_{ij} - L_{f_i}^2 h_{ij}),$$

$$\beta_{ij} = -[L_{g_i} L_{f_i} h_{ij}]^{-1} \cdot L_{p_i} L_{f_i} h_{ij},$$

$$\gamma_{ij} = -[L_{g_i} L_{f_i} h_{ij}]^{-1} \cdot L_{r_i} L_{f_i} h_{ij}.$$

The control law (Eq. 2.13) depends on the stance leg (indicated by j) only through the output function h_{ij}. The human controller u_{Hj} will utilize different output functions between stance and swing according to [61]. However, for the prosthesis we will utilize a single output function h_P that does not change between stance and swing. Thus, we can define a unified control law for the prosthesis:

$$u_P = \alpha_P + \beta_P \cdot F + \gamma_P \cdot G_P. \tag{2.14}$$

It can be difficult to accurately measure the interaction forces F and the ground reaction forces G_P as well as accurately model the $\alpha_P/\beta_P/\gamma_P$ terms for the prosthesis, which may make implementing feedback linearization challenging. An alternative control approach is a linear output PD controller that does not require these modeling terms or force measurements, possibly at the cost of tracking accuracy [32]. In particular, we can approximate the desired feedback linearization by directly generating control torques with the linear input v_P used in Eq. 2.14. This input is usually defined as an output PD control law, which when used on its own can be interpreted as joint impedance control:

$$u_{imp} = -K_p(H_{0P} q_P - h_P^d(s_P)) - K_d(H_{0P} \dot{q}_P - \dot{h}_P^d(s_P)), \tag{2.15}$$

where K_p and K_d are gains to control stiffness and damping, respectively. Section 2.3.4 will display that this control law (Eq. 2.15) can reasonably enforce the unified virtual constraints with a proper choice of PD gains.

2.3.3 Perspective of Piecewise HZD vs Unified Virtual Constraints

The previous section shows how to encode a given trajectory into a unified virtual constraint but not how to design such a trajectory. In the prosthetic application it is desirable to leverage the provable stability properties of piecewise HZD designs [115, 102, 89, 10, 40, 69, 125] while respecting the continuous, periodic nature of human walking. Therefore, this section will convert the prosthetic HZD design from [61, 63] into continuous, unified DFT virtual constraints and discuss the fundamental differences between the two approaches.

HZD-based controllers are defined in a piecewise manner, where the virtual constraint depends on which leg is in stance. This allows the controller to respect the discontinuous impact dynamics (Eq. 2.10), so that if the error just before a properly timed impact is zero, the error just after impact will also be zero. This behavior is called hybrid invariance. Because the DFT parameterization is infinitely smooth and unified across impact events, it cannot be hybrid invariant. By definition these smooth trajectories cannot encode the velocity discontinuities across the impact model. However, the simulations in Section 2.3.4 will show that the unified DFT controller approximates the stability properties of the piecewise HZD design. Moreover, this section will demonstrate the benefits of the unified approach when the impact occurs earlier or later than expected (as is common with human variability [62]), which violates the hybrid invariance assumption of the original HZD design.

The piecewise HZD virtual constraints in [61, 63] are parameterized by the common Bézier polynomial form

$$h^d_{P,j}(s_P) = \sum_{i=0}^{Q} \frac{a_i Q!}{i!(Q-i)!} s_P^i (1-s_P)^{Q-i}, \tag{2.16}$$

where j indicates which leg is in stance, $Q = 5$ is the degree of the polynomial, a_i are the polynomial coefficients, and s_P is the normalized phase variable within stance or swing. Hybrid-invariant Bézier polynomials were designed for the knee and ankle to mimic certain features of human walking at various speeds [61, 63], and here we consider the 1.2 m/s design.

In order to create unified virtual constraints, the stance and swing Bézier polynomials were concatenated and sampled to provide one periodic sequence with $N = 1000$ equally spaced data points. The frequency terms $X[k]$ of this sequence were computed by the MATLAB fft function and then used to create the unified DFT function from Eq. 2.6. The DFT spectrum of these trajectories indicate that the magnitude is approximately zero between the 10^{th} frequency and the Nyquist sampling frequency ($N/2$). As a result, the DFT series can be truncated to reduce the number of coefficients in h_P^d and in turn reduce the computational complexity of the control law (Eq. 2.14 or 2.15).

Table 2.1. Fitting Statistics of DFT Design

	Knee		**Ankle**	
K value	r^2	RMSE (rad)	r^2	RMSE (rad)
5	0.999	2.23e-04	0.995	1.33e-04
10	1.000	6.14e-05	1.000	3.14e-05
$N/2$	1.000	4.50e-05	1.000	1.17e-05

To verify that the first 10 indices accurately represent the desired trajectories, virtual constraints were generated with $K = 5$, 10, and $N/2$, where K is the highest index k in Eq. 2.6. As expected the virtual constraints for $K = 10$ and $N/2$ are similar and more accurate than that of $K = 5$ (Table 2.1). The virtual constraints with $K = 5$ have coefficients of determination $r^2 > 0.995$, whereas the $K = 10$ case has $r^2 = 1.000$. In all cases, the root mean square error (RMSE) is less than 2.3e-04 rad. From this analysis we can conclude that a 5^{th}- or 10^{th}-order DFT function is sufficient to parameterize the 5^{th}-order Bézier polynomials, so the two approaches will have similar real-time computational costs.

The unified DFT parameterization of the piecewise HZD polynomials provides unique properties that are advantageous for the prosthetic application. The periodic DFT design parameterizes the knee and ankle trajectories across gait cycles, whereas the Bézier polynomials immediately diverge to unbounded values outside the design range of s_P (Fig. 2.2).

Therefore, the piecewise design requires very accurate detection of stance vs. swing, which can be difficult to measure from the limited sensors on a prosthetic leg. Moreover, the strict design range of the Bézier polynomials makes them more sensitive to drift in the phase variable, which must be reset back to zero after every impact event to avoid exceeding the design limits. Practical HZD implementations typically saturate the phase variable at the design limits to prevent undesirable angle commands [64]. In contrast, the DFT design is periodic over the phase variable, so this formulation transitions seamlessly to the next gait cycle. Thus, the phase variable does not necessarily have to be reset or saturated as the amputee transitions from one step to the next, which may simplify the control implementation and lead to more predictable behavior.

In conclusion, piecewise HZD polynomials can be converted to unified DFT virtual constraints with limited coefficients in the output function h_P^d. This method unifies not only a single stride but also periodic steady-state locomotion. In the DFT formulation, the phase variable may only need to be reset across short or long strides to ensure the following stride begins at the proper phase location (modulo the design range of the phase variable). Occasional resets in the phase variable may also be desirable in practice to prevent measurement drift.

2.3.4 Simulation Results

Evaluation of Piecewise HZD and Unified DFT

We began with the human and prosthesis HZD designs in [61, 63] for three speeds: normal walking at 1.2 m/s, slow walking at 0.8 m/s and fast walking at 1.6 m/s. Unified DFT virtual constraints were generated for the prosthesis at each speed based on the piecewise Bézier polynomials as described in Section 2.2. For comparison the prosthesis was simulated with either the piecewise HZD virtual constraints or the unified DFT virtual constraints. In all simulations the human part used the piecewise HZD controller for each walking speed

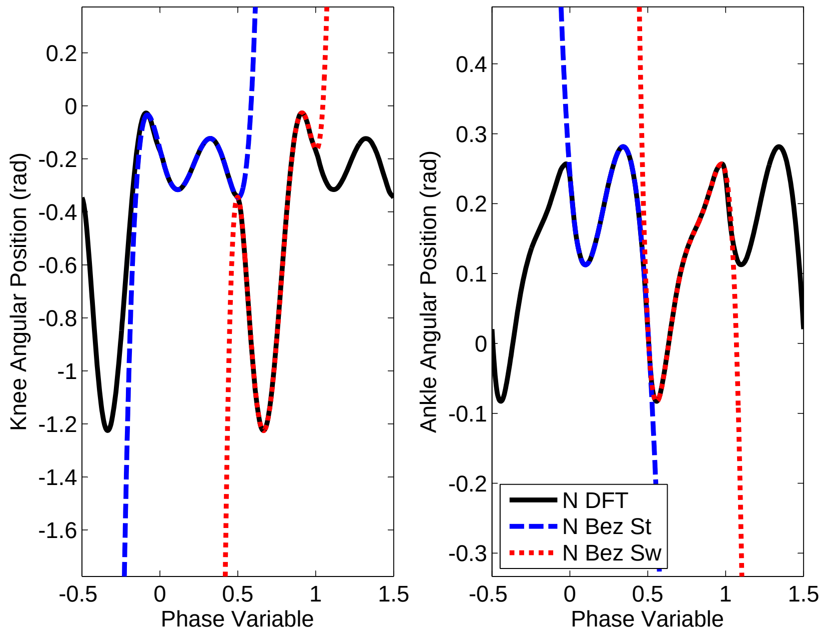

Figure 2.2. Virtual constraints by DFT and Bézier polynomial (Bez) for the knee (left) and ankle (right) during normal human walking (N). Because Bézier virtual constraints are defined in a piecewise manner, their normalized phase variable goes from 0 to 1 twice per stride. For comparison, the Bézier phase variable has been scaled and shifted to match the DFT phase variable. The DFT function repeats the gait cycle for phase variable values $s_P < 0$ and $s_P > 1$, i.e., the ranges of $-0.5 \leq s_P < 0$ and $0.5 \leq s_P < 1$ are identical. In contrast, the piecewise Bézier polynomials for stance (St) and swing (Sw) diverge to undesirable trajectories on both sides of the design region.

and did not change based on the form of the prosthesis controller. The piecewise HZD controllers reset the phase variable at every impact, whereas unified DFT controllers only reset the phase variable at the start of every prosthesis stance period. Both subsystems used the feedback linearizing torque control law (Eq. 2.13), for which the PD gains were manually tuned and held fixed for all simulations and prosthesis controllers.

Simulations were first performed for the idealized case when both the prosthesis and human had the same desired walking speed. The unified prosthetic controller for each speed tracked the reference HZD virtual constraints very accurately, even across impacts (Fig. 2.3). Small differences can be observed in the joint velocities (Fig. 2.4), particularly for the fast walking speed due to larger impact discontinuities. Despite the fact that the unified DFT controller was not hybrid invariant, it performed similarly to the piecewise HZD controller in the ideal case of exactly matched human and prosthesis intent.

Because the intent of the prosthesis and the amputee will rarely be perfectly coordinated, it is critical that the prosthesis reacts in a stable and predictable manner to mismatches in the desired walking speed. This is likely to be one of the greatest sources of variability from the human. To test robustness to speed perturbations, the prosthesis was held fixed at the normal walking speed while the human was set to either the slow or fast speed. Despite these disturbances, the biped system converged to steady-state walking for both prosthesis control formulations without any additional tuning. The interaction between the mismatched human and prosthesis resulted in somewhat unexpected changes in speed, although the fast human controller led to faster than normal walking (and reduced step durations) and the slow human controller led to slower than normal walking (and much longer step durations).

As expected, the mixed speed cases had more tracking error than the matched speed cases (Fig. 2.5). However, both prosthesis controllers zeroed the tracking error before every impact without requiring unrealistic joint angles or velocities. The two control formulations produced similar torque curves (Fig. 2.6), which will be discussed later.

In the mixed cases, the Bézier virtual constraints were no longer hybrid invariant, so one of the greatest advantages of the piecewise HZD controller was lost. The transition between strides tended to occur sooner than expected, resulting in discontinuities in the commanded joint angles and thus the tracking errors (and corrective torques). Both controllers had similar errors at the start of prosthesis stance (phase variable from 0 to 0.5), but the unified DFT controller had much smaller errors than the piecewise HZD controller at the start of prosthesis swing (phase variable from 0.5 to 1.0). The small DFT errors may be because the stance-to-swing transition was relatively smooth in velocity, resulting in better tracking from the smooth DFT controller. Further, the DFT phase variable was not reset at the stance-to-swing transition, so a shorter or longer step had less influence on the error. Because the

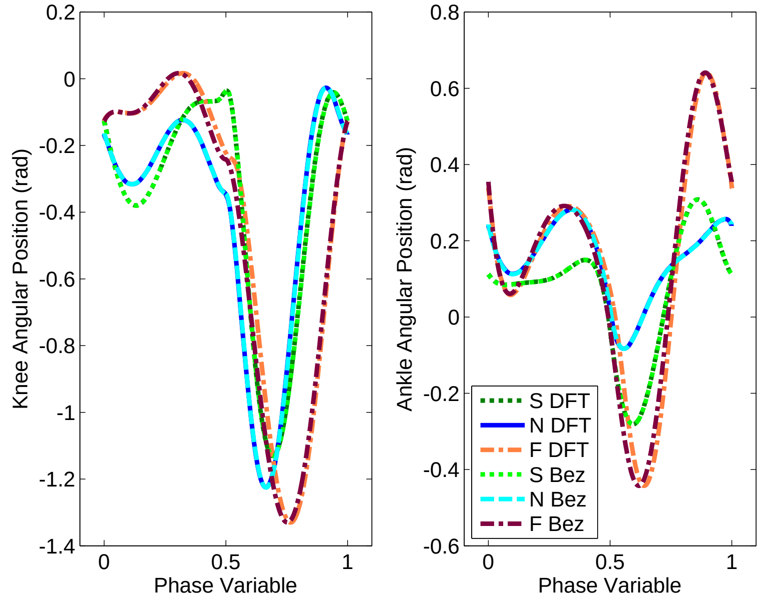

Figure 2.3. The simulated trajectories of the prosthetic knee (left) and ankle (right) with both the DFT and Bézier controllers for three different walking speeds (matched with the human speed) plotted against the DFT normalized phase variable. The DFT and Bézier response is almost identical in all cases.

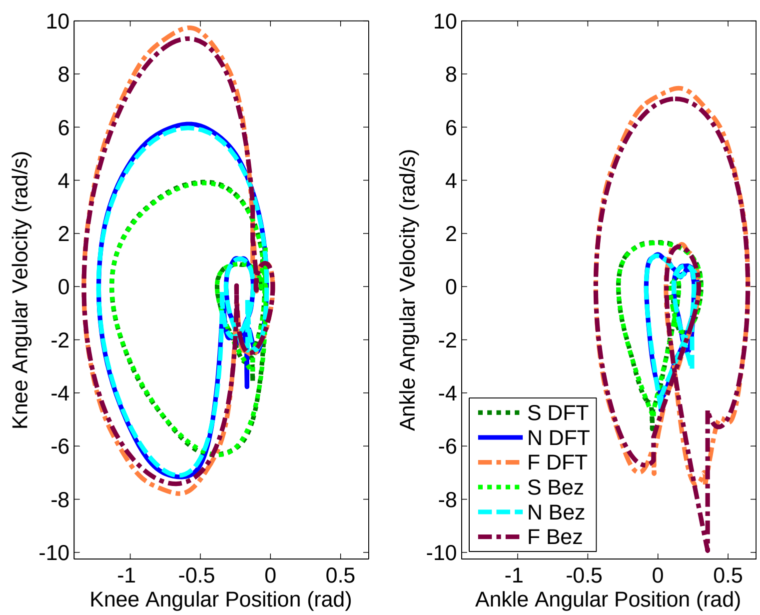

Figure 2.4. The simulated phase portrait for the prosthetic knee (left) and ankle (right) for three different walking speeds (matched with human) with the DFT and Bézier controllers. The DFT gaits closely match the reference Bézier gaits. As expected, the greatest deviations occur near impacts. The rolling motion of the curved foot results in a slightly larger ankle orbit for slow walking than normal walking with both controllers.

Bézier virtual constraints were defined in a piecewise manner, they were not continuous if the stance-to-swing transition occurred sooner than expected. As a result, the unified controller tracked the desired virtual constraint better than the piecewise HZD controller when the human and prosthesis intent was not exactly matched, as is likely to occur in reality.

Stability of Walking Gaits

The local orbital stability for both the matched and mixed speed controllers are analyzed using the method of Poincaré sections [115]. To do so, define the extended state vector from all of the prosthesis and human generalized coordinates as $x_e = (q_e^T, \dot{q}_e^T)^T$, where $q_e = [q_1, q_2, q_3, q_4, q_5, q_6, q_x, q_y]^T$. Walking gaits are cyclic and correspond to solution curves $x_e(t)$ of the hybrid system such that $x_e(t) = x_e(t+T)$, for all $t \geq 0$ and some minimal $T > 0$. These solutions, known as *hybrid periodic orbits*, correspond to equilibria of the Poincaré map $P : G_{\mathrm{P}} \rightarrow G_{\mathrm{P}}$, where the Poincaré section G_{P} is the set of states corresponding to prosthesis heel strike. The function $P(x_e)$ models two full steps of the biped, mapping the state from a prosthesis impact event to the subsequent prosthesis impact event. A periodic solution $x_e(t)$ then has a fixed point $x_e^* = P(x_e^*)$, about which the Poincaré map can be linearized to analyze local stability. If the eigenvalues are within the unit circle, then the discrete system is locally stable, and we conclude that the hybrid periodic orbit is also locally stable.

In ideal conditions, the hybrid-invariant Bézier polynomials enable an analytical proof of orbital stability with the lower-dimensional HZD [61, 63]. However, hybrid invariance is violated by any mismatch with the human controller, including the mixed speed cases. Moreover, by definition the unified virtual constraints do not satisfy hybrid invariance. Because the analytical HZD result cannot be utilized in these cases, we instead use the perturbation analysis procedure described in [29, 30] to numerically calculate these eigenvalues based on simulations. In all cases, the eigenvalues of the linearized map fall within the unit circle (Table 2.2). Thus, the gaits are orbitally stable in the matched and mixed speed cases.

Table 2.2. Maximum Eigenvalues with Unified Prosthetic Controller

	Human Model			
	Walking Speeds	**Slow**	**Normal**	**Fast**
Prosthetic Leg	**Slow**	0.774		
	Normal	0.717	0.760	0.639
	Fast			0.758

Simulated Walking with Impedance Controller

To apply the feedback linearizing control law (Eq. 2.14), the dynamics of the prosthesis must be known. Obtaining an accurate dynamic model of the physical system is a challenge in itself. With an uncertain dynamic model and limited sensory feedback for the prosthesis, feedback linearization may be difficult to implement experimentally. A more practical, model-independent implementation of the unified virtual constraints is joint impedance control (Eq. 2.15), which approximates the torque control inputs for the feedback linearizing controller.

This control law was implemented for the prosthesis of the amputee biped model. Noting that real actuators are torque-limited based on the motor and transmission, a saturation limit of ± 120 Nm was implemented for each actuated joint, which is representative of existing powered prosthetic legs designs [104, 6, 86]. Feedback linearization was still used for the human part of the model, which has been validated as a predictor of certain features of human walking [65, 62]. Using the method from Section 2.3.4, the impedance controller was shown to be locally exponential stable with similar eigenvalues to the feedback linearizing controller.

Fig. 2.6 compares the torques of the impedance controller against the feedback linearizing controllers for both DFT and Bézier in the mixed speed case of normal prosthesis and slow human. For the most part, the controllers produce similar torques. All controllers exhibit large torque spikes just after the discontinuous impact events. These spikes can only be achieved with ideal actuators in simulation, whereas a real actuator with dynamics

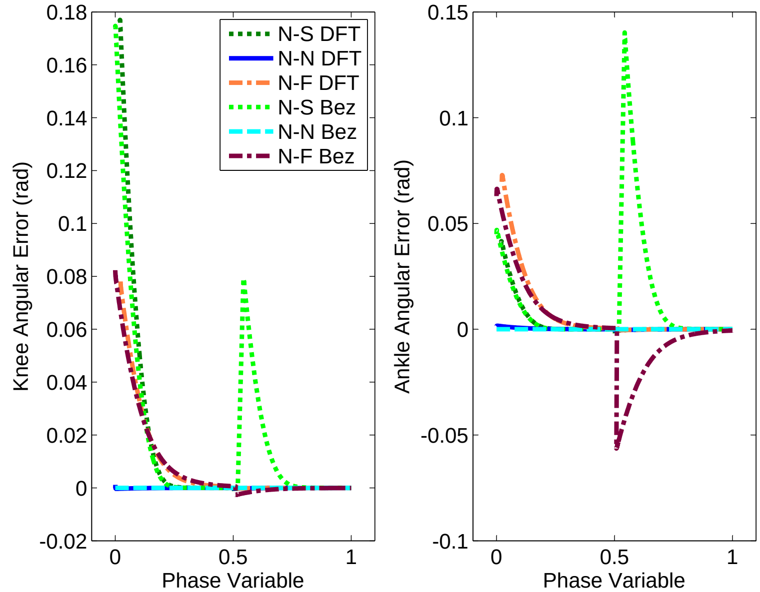

Figure 2.5. The simulated tracking errors of the prosthetic knee (left) and ankle (right) for both the unified DFT and piecewise Bézier controllers during steady-state walking with mixed speeds. The normal matched speed error is also shown for comparison. Both controllers have similar error at the start of the stance period (phase variable near 0), but the DFT controller has significantly less error at the start of the swing period (phase variable near 0.5). Note: N-S = normal walking (prosthesis) and slow walking (human), N-N = normal walking (prosthesis) and normal walking (human), and N-F = normal walking (prosthesis) and fast walking (human).

would smooth out these torques. More importantly, step transitions in human walking are continuous with a finite double-support period, so these discontinuities cannot occur in practice (see [32, 86]). This demonstrates the feasibility of a model-independent control method for practical implementation in a powered prosthesis.

2.3.5 Discussion

The unified controller eliminates the need to divide the gait into different periods with independent controllers. Since the DFT virtual constraint is periodic, the controller does not need to be reset at the start of each stride. The feasibility of the controller was demonstrated using simulations of an amputee walking model. Three distinct walking speeds were designed

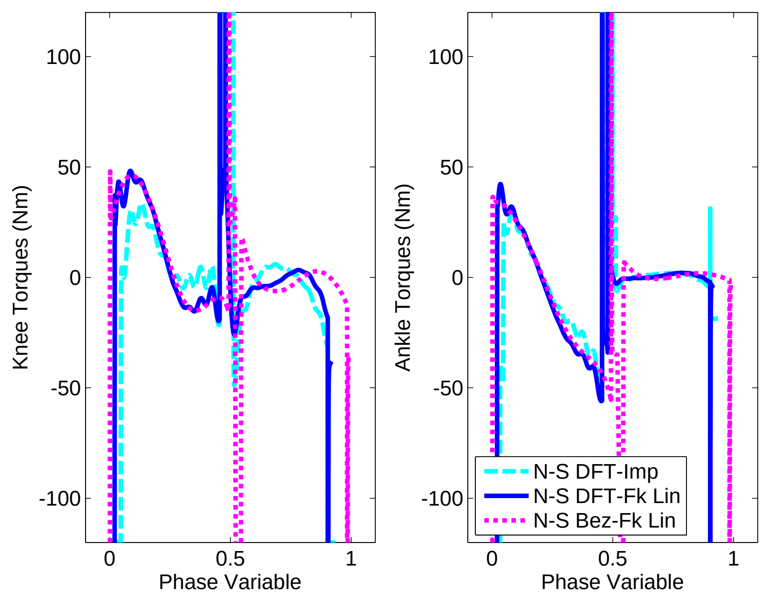

Figure 2.6. The simulated torques of the prosthetic knee (left) and ankle (right) for the mixed case of the human at slow speed and the prosthesis at normal speed with the Bézier feedback linearizing controller (N-S Bez-Fk Lin), the DFT feedback linearizing controller (N-S DFT-Fk Lin), and the DFT impedance controller (N-S DFT-Imp). The torques of the impedance controller approximate the feedback linearizing controllers throughout the gait cycle. The torque impulses after impacts are caused by discontinuities in velocity from the impulsive impact model, which do not occur during human walking.

that produced stable periodic gaits. Robustness to speed uncertainty was demonstrated by using a fixed prosthesis controller while the human controller was varied. This provides a basis of how the controller will function for a real system as generally the prosthesis and contralateral leg will be performing at different walking speeds between them. Furthermore, a model-independent impedance controller was also evaluated, demonstrating the viability of implementing the unified control method in hardware. This control strategy can be implemented on a powered knee-ankle prosthesis, which is investigated in Chapter 3. The unified virtual constraints could be defined for various activities with well-characterized joint kinematics (e.g., from able-bodied data [116, 20]). This is investigated experimentally with transfemoral amputee subjects performing various speeds and slopes for task-specific virtual constraint designs in Chapter 4.

CHAPTER 3

DESIGN AND REAL-TIME CONTROL OF A POWERED PROSTHESIS

Extensive epidemiologic surveys has been conducted worldwide, where it is predicted that every 30 seconds a lower limb is lost due to diabetes [7]. As the number of amputation increases, more sophisticated prosthetic devices are needed for the lower limb amputee population. Current prosthetic leg technology is very inefficient because it relies on amputee's motion to swing the thigh to lock the knee joint based on the passive leg design. A powered prosthesis leg design can emulate the lower limb muscular function to provide joint power that can relieve the overexertion amputees endure during gait and improve stability to reduce risk of falling. Furthermore, a passive leg is restricted in its functionality based on the limitation of its hardware, while a powered prosthesis can provide the appropriate biomechanical features observed during gait such as loading response of knee flexion at heel strike or ankle plantarflexion for push-off during pre-swing. The combination of the prosthesis mechanical design and control strategies assist in providing these biomechanical functions during locomotion. Chapter 2 discusses theoretical control methods that can be utilized to control the synchronization of a multi-joint powered prosthesis for human gait. To implement the control strategies on an actual control system, a UTD robotic leg test bed was designed and manufactured. All three discipline areas of mechanical, electrical, and software are utilized in designing a powered prosthetic leg with a real-time control system.

Section 3.1 presents the performance requirements and the mechanical design of UTD Leg 1. In Section 3.2 will explain the electronics portion of the prosthesis that include the real-time microprocessor, motor power amplifiers, and sensory feedback. Section 3.3 covers the control system design to perform real-time control of the powered prosthesis. Outer and inner control loops will be explained for how the control architecture was implemented to the prosthesis to perform subject experiments (see Chapter 4). The outer loop consists of the method of virtual constraints by DFT unified over the gait cycle with a human-inspired phase variable derived from the thigh motion. The inner loop involves a closed-loop torque control to increase system bandwidth and reduce tracking error. A standalone experiment with an able-bodied subject is explained to validate the phase variable prior to integrating the algorithms to the prosthesis controller.

In Section 3.3.4, the control scheme is altered for the formulation of volitional control that consist of a piecewise phase-based control to provide the amputee more capability using the prosthesis. This control scheme allows a transfemoral amputee to perform more daily locomotion activities that entail non-rhythmic motions in Chapter 5 with clinicians adjusting the controller. Lastly, Section 3.4 will report the control performance of the prosthesis with both benchtop experiments and preliminary experiments with able-bodied subjects.

3.1 Prosthesis Mechanical Design

The most advanced microprocessor controlled prostheses only provide variable damping at the joints, which does not include input power. Recent advancements of actuator and sensing technology has enabled a revolution of powered prostheses [58]. Such technology advancements include high power-to-weight ratio BLDC motors, high computation power in microprocessors, and small integrated circuit-based sensors (e.g., encoders, force sensors, etc.). Even with the recent technology advancements there are still very limited commercially available powered prostheses in the market. Therefore, developing a powered knee-ankle prosthesis was required to have a test bed for control implementation to validate our control schemes. Several challenges are presented to the design of a fully functional multi-joint powered prosthesis to be worn by human subjects for testing various control strategies.

To begin, several performance requirements were developed to define design constraints that the prosthesis must meet to output the expected performance conditions for control development. The overall design requirements of a powered prosthesis are based on the locomotion performance of an able-bodied [116, 77]. The prosthesis must include knee and ankle joints that replicate the range of motion to that of a human leg. Furthermore, the torques produced at the prosthetic joints must meet comparable torques produced by human joints during gait stride. The powered prosthesis is to support the static and dynamic loading experienced during normal walking. The device must have sensory feedback as part of the implementation of the control algorithms. For maintainability, this experimental test bed should primarily contain commercial off-the-shelf (COTS) parts in assembly and should be safe for human testing with nominal height and weight subjects [116]. This means structurally that it must be able to support the weight and forces of someone average sized using the prosthesis.

Table 3.1. Powered Prosthesis Design Specifications

	Knee	**Ankle**
Range of Motion	0° to -70°	-25° to 15°
Peak Torque	40 Nm	120 Nm
Peak Power	255 W	73 W

Primarily, the prosthesis should provide a platform for testing different control strategies to operate the leg. The weight constraint on the leg was set to be roughly 4.5 kg, which is a reasonable requirement by limitations of current COTS availability for high power-to-weight ratio motors and transmission components. The majority of the electronics are to be placed onboard with the microprocessor and power source located remotely with signals transmitted through tethered cable, so as to reduce the weight requirement of the system. Table 3.1 gives design specifications for the prosthesis based on an average human weight of 75 kg at normal walking speed in [116].

Taking the design specifications under consideration, several design concepts were considered between various rotary and linear actuator systems as well as a combination between the two for each joint. A pure rotation actuator has advantages in reaching high joint velocities, ease in obtaining the range of motion, and having backdrivability. However, similar

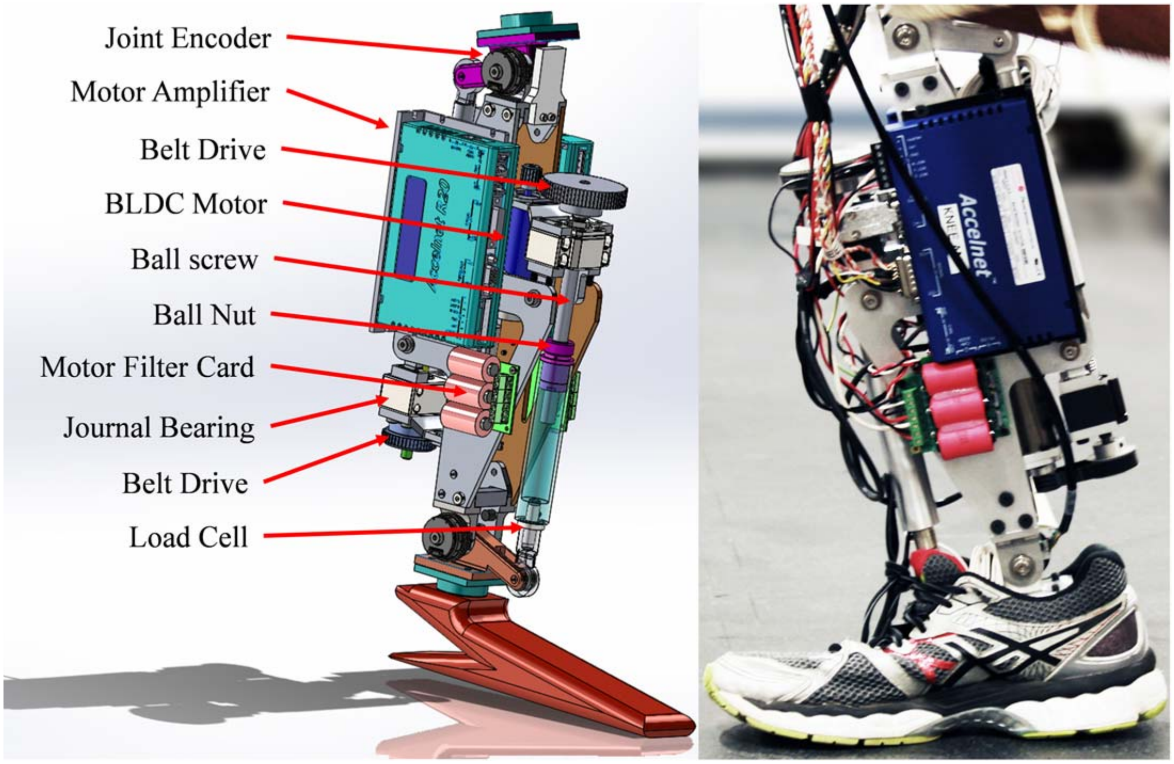

Figure 3.1. The UTD powered knee-ankle prosthesis: CAD rendering and key components (left) and manufactured version (right). A timing belt connects each motor to a linear ball screw, which the ball screw translational motion drives a lever arm to produce a joint torque.[1]

to the prosthesis in [58] it has limitation in torque output, where a custom rotary design would require a multistage transmission to obtain the desired torques. Furthermore, a rotary transmission contains more mechanical moving parts, which potentially would require more maintenance. Linear actuators are inherently a slower prime mover with limitation in joint range of motion, and generally have a high gear ratio which makes them non-backdrivable. Although, their high effective gear ratios from their force output can produce high joint torques. Relying heavily on weight considerations, maintainability, and achieving the torque requirements; a linear actuator design was the leading candidate for a first generation powered prosthesis at UTD. The design of the powered prosthetic leg can be seen in Fig. 3.1.

The powered prosthetic leg has a multi-stage drive system that provides the required torque needed at the knee and ankle joints while allowing users to achieve a normal gait. A high power-to-weight ratio Maxon three-phase BLDC Motor (Model: EC-4pole 30, Maxon Motor, Sachseln, Switzerland) is used capable of producing 200 W continuous power to the transmission. The motor output shaft is connected to a linear ball screw through a Gates GT3 timing belt drive with 7075 aluminum sprockets (with a 2:1 reduction at the knee and 4:1 at the ankle). A Nook 12 mm diameter, 2 mm lead ball screw (Model: PMBS 12x2r-3vw/0/T10/00/6K/184/0/S, Nook Industries, Cleveland, OH, USA) converts the sprocket's rotary motion into linear motion of the ball nut, which drives a lever arm to generate the joint torque. Although the resulting gear ratio is nonlinear depending on the joint angle, the average ratio is 360:1 at the knee and 720:1 at the ankle. The high gear ratio does give limitation with backdrivability and a high stiffness actuation system, but it surpasses the importance in producing able-bodied joint torques. Each ball screw is supported axially and radially by a Nook double bearing support journal (Model: EZBK10-SLB, Nook Industries, Cleveland, OH, USA). A motor mount with a rotational pivot was designed to eliminate buckling of the ball screw and increase its linear motion as it travels up/down to rotate the joint via the lever arm, providing the desired range of motion at each joint.

The outer structural plates are made out of 7075 aluminum alloy used mainly as a carrier for mounting the electronics. Hard stops at the end of the ball nuts were 3D printed from a polyjet material to eliminate ball screw travel beyond its intended range. Fig. 3.1 displays key design components of the actuation system for the powered prosthesis. Overall, the mass of the leg is 4.8 kg, which is comparable with other powered knee-ankle legs in the literature [105, 58, 80]. In Appendix A, shows the bill of materials used in fabricating the prosthesis and Appendix B derives the kinematics analysis for the given actuation system.

3.2 Prosthesis Electronics & Sensing

The powered prosthesis consists of a hardware system with multiple sensor signals fed back to a microprocessor for real-time computing. The offboard computation and power is provided to the powered leg through a tether. The microprocessor utilized for the prosthesis leg is a dSPACE Freescale OorIQ P5020, dual-core, 2 GHz processor (Model: DS1007, dSPACE GmbH, Paderborn, Germany) that provides real-time control and data acquisition at 1 kHz. A 35V/60A DC power supply (Model: 6673A, Agilent Technologies, Santa Clara, CA, USA) provides power to the onboard motor amplifiers. A separate DC power supply (Model: 1761, BK Precision, Yorba Linda, CA, USA) was used for low current output in powering the onboard sensors.

For low-level sensory components, each motor has an incremental, 3000 counts per turn quadrature encoder (Model: 2RMHF, Maxon Motor, Sachseln, Switzerland) measuring motor output shaft angular position. The motors are driven by a motor amplifier (Model: ADP-090-36, Copley Controls, Canton, MA, USA) to apply three-phase sinusoidal commutation for current control. The Maxon BLDC motors have low inductance value (terminal inductance phase to phase at 0.0163 mH), thus an inductance filter card (Model: BFC10010, Advanced Motion Controls, Camarillo, CA, USA) with 0.200 mH inductors per phase is embedded inline between the motor phase lines and the motor amplifier to increase the impedance load for the amplifier. This did increase the mass of the overall weight of the leg with each filter card weighing 0.21 kg. At the joints, an assembled high resolution, 4000 cycles per revolution optical encoder (Model: EC35-4000-4-375-H-D-DM-B, US Digital, Vancouver, WA, USA) mounted to the joint's output shaft measuring joint angular position. Joint velocities are computed numerically with a first-order low-pass Butterworth filter at 8 Hz cutoff frequency.

In order for the rigid ankle actuator to achieve compliant and forceful interaction with the ground [35, 36, 18], a uniaxial force sensor (Model: LCM200, Futek, Irvine, CA, USA)

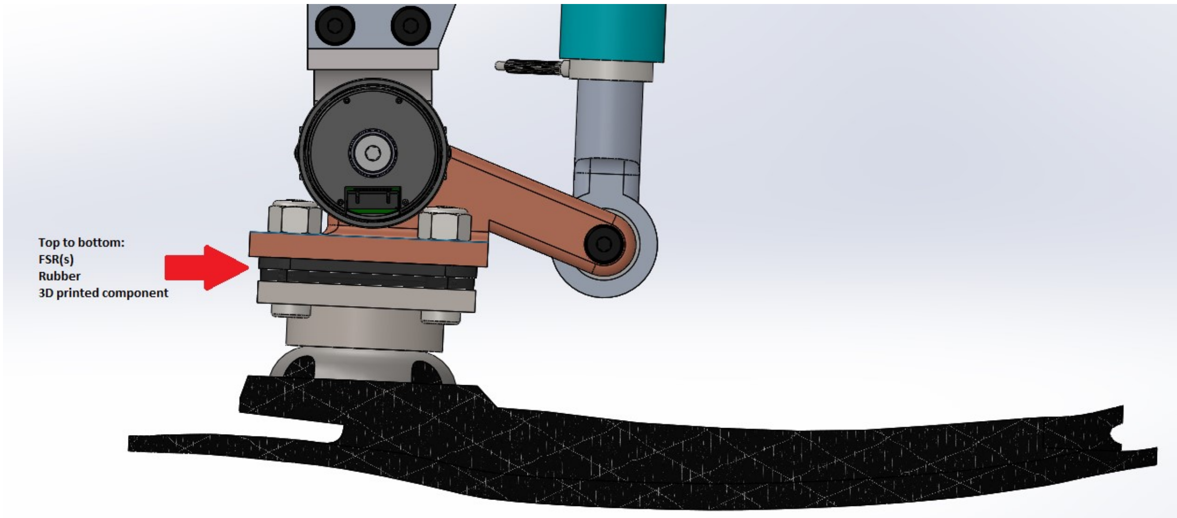

Figure 3.2. A CAD rendering of the FSR placement between two 3D printed neoprene rubber material located above the prosthesis' foot female pyramid adapter and below the ankle's lever arm mount.

is installed inline with the ankle's ball screw to provide feedback for a closed torque loop (Section 3.3.3). This force sensor is connected to an offboard analog amplifier (Model: CSG110, Futek, Irvine, CA, USA). A force sensor could not be used in the knee actuator due to off-axis overloading during peak knee flexion.

In order to compute the phase variable in Section 3.3.1, an Inertial Measurement Unit (IMU) (Model: 3DM-GX4-25, LORD MicroStrain, Williston, VT, USA) is mounted above the prosthetic knee in the sagittal plane to measure motion of the thigh. The IMU contains a triaxial accelerometer, gyroscope, and magnetometer. Dual onboard processors run an Adaptive Kalman Filter with a full-state dynamics model based on Newton's and Euler's equations of motion to compute real-time Euler Angles in the IMU coordinate frame at a sampling rate of 500 Hz. Velocities of the Euler angles are estimated with a low-pass filter to reduce sensor noise as in [51]. A force sensitive resistor sensor (FSR) (Model: FlexiForce A401, Tekscan Inc., Boston, Massachusetts, USA) is placed above the pyramid adapter of the prosthetic foot (see Fig. 3.2). An analog-to-digital converter produced a high FSR signal measurement as the leg is in stance period (i.e., the prosthesis foot contacts the ground),

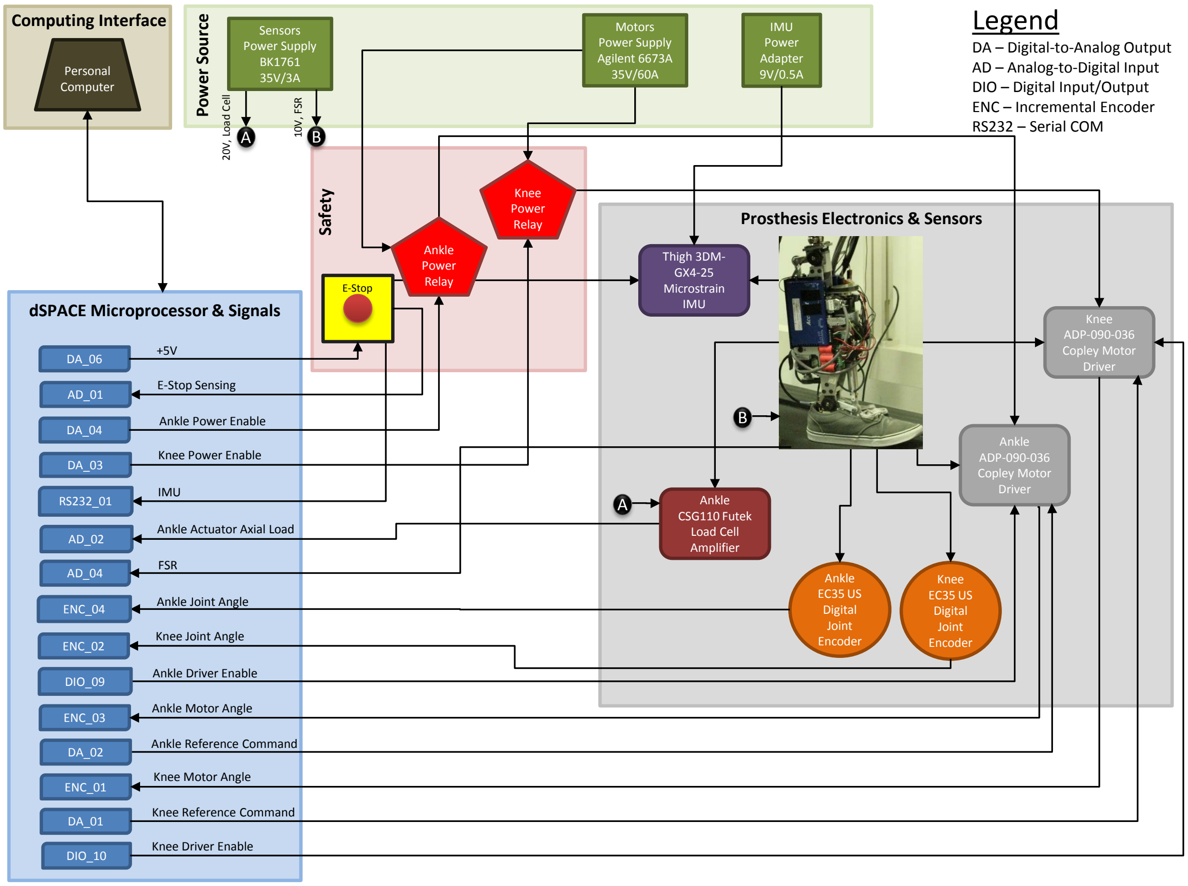

Figure 3.3. UTD Powered Prosthesis Leg Embedded System routing of the offboard power source to the motor drivers and sensors on the leg. Sensor feedback signals are routed to the dSPACE processor for real-time control computation. Hardware safety components are included during leg operation with power solid-state relays and an operator Emergency Stop (E-Stop) button.

while a low FSR measurement detects swing period (i.e., the prosthesis foot no longer has contact to the ground). This stance and swing detection is utilized for the control scheme in Section 3.3.4. Fig. 3.3 displays an embedded system flow diagram of the prosthesis.

3.3 Real-Time Control System Architecture

Currently, it is a challenge to provide a powered knee-ankle prosthesis in the commercial market due to the obstacles in developing a safe and viable control strategy. Even the most advanced microprocessor controlled prostheses only provide variable damping, but add no power to the users stride. For lower limb powered prostheses require sophisticated control methods due to high potential risk of amputees falling. Different control strategies are being investigated in several research institutions, so future efforts could bring this technology in the commercial market and allow amputees a better way of life in terms of mobility. Here at UTD, a research powered prosthetic test platform was designed and built to validate our control methods using virtual constraints by DFT proven in simulation (Section 2.3.4), which validated with amputee subjects.

Different control system designs have been developed for the powered prosthesis to achieve various amputee subject experiments in Chapters 4 and 5. Prior to implementing the virtual constraint controller, preliminary experiments were performed to verify real-time measurements of the phase variable in Section 3.3.1. This was performed with an able-bodied subject to verify the algorithms and their robustness across various speeds, as amputee subjects will perform different speeds when using the powered prosthesis. Then in Section 3.3.3, the control loops are described for the virtual constraint and closed-loop torque control used in amputee experiments. Lastly, Section 3.3.4 derives the phase-based control strategy to be implemented for the clinical study described in Chapter 5. The control algorithm for UTD Leg 1 is implemented in software using MATLAB/Simulink [66] and compiled to the dSPACE processor board for real-time control. Appendix C shows the main control subsystem models developed for control of the leg. Figs. C.12 and C.13 display the graphical user interface to operate the leg and data acquisition of the measurement signals, respectively.

3.3.1 Real-Time Human-Inspired Phase Variable Algorithms[2]

Several control subsystems were developed as part of the overall control system architecture. One important control subsystem involves the real-time phase variable algorithms as part of the virtual constraint (Eq. 2.1). The phase variable involves computing the thigh phase angle from the thigh phase portrait. The phase variable was incorporated as a standalone subsystem, so verification tests could be performed prior to subjects using the prosthesis.

This section proposes a real-time method using a single IMU sensor to measure the continuous phase variable that was originally proposed in the offline analysis of [113]. Signal processing algorithms are defined to estimate a monotonic, increasing phase variable that represents the progression from 0% to 100% of the gait cycle. Our results demonstrate appropriate changes in the rate of the phase variable and the ability to predict the stance-to-swing transition across multiple walking and running speeds (1-9 miles/hour). Moreover, the polar radius from the orbit within the thigh phase portrait provides a linear relationship for estimating the subject's walking speed during gait.

Continuous Gait Phase Variable

The continuous phase variable is constructed by the phase angle from the thigh phase portrait (i.e., phase plane of thigh velocity vs. angle). The raw thigh angle is measured from an IMU sensor (LORD MicroStrain, 3DM-GX4-25) mounted to a leg holster that is strapped to the thigh along the sagittal plane (see Fig. 3.4). The IMU sensor has a compact size of 36 mm x 36.6 mm x 11.1 mm and weighs 16.5 g. The sensor measures its own Euler angles sampled at 500 Hz.

The start of the phase angle occurs in the first quadrant of the phase portrait along the positive x-axis. The phase angle increases as it orbits a full revolution counter-clockwise in

[2] © 2018 IEEE. Reprinted, with permission, from D. Quintero, D. J. Lambert, D. J. Villarreal, and R. D. Gregg, Real-Time Continuous Gait Phase and Speed Estimation from a Single Sensor, IEEE Conference on Control Technology and Applications (CCTA), 2017.

Figure 3.4. Photo of human subject walking on a treadmill while wearing an IMU sensor on the thigh with a sagittal plane orientation. Thigh angle measurement follows the righthand rule.

the phase portrait, completing the gait stride at the fourth quadrant returning to the x-axis. The phase angle is computed using the four-quadrant $\text{atan2}(y, x)$ function, which is defined as the unnormalized phase variable

$$\varphi(t) = \text{atan2}(\dot{\theta}_y(t), \theta_x(t)). \tag{3.1}$$

More detail on the derivation and biomechanical implications of the phase variable can be found in [113]. The variables $\dot{\theta}_y(t)$ and $\theta_x(t)$ are the estimated thigh velocity and thigh angle signals, respectively, for constructing the thigh phase portrait. shift, negated thigh velocity $\dot{\theta}_y(t)$ are used in constructing the thigh phase portrait. These variables are shifted and scaled to enhance the linearity and monotonicity of the phase variable $\varphi(t)$ during a gait cycle (Section in 3.3.1).

Filters are designed to provide smooth input signals for real-time calculation of the phase variable $\varphi(t)$. An interpolating polynomial filter (Section in 3.3.1) filters the raw thigh angle measurement to mitigate unwanted disturbances observed from the IMU. The thigh angle and its velocity are shifted and scaled to compute the phase variable (Section in 3.3.1), which is then passed through a monotonic filter to further mitigate the effect of noise. Finally, to detect whether or not a subject is walking, a start and stop detection algorithm is implemented (Section in 3.3.1). Fig. 3.5 displays a schematic of the thigh phase portrait based on $(\theta_x(t), \dot{\theta}_y(t))$ coordinates as the phase variable $\varphi(t)$ is measured about the circular orbit during the gait cycle. The phase variable $\varphi(t)$ from Eq. 3.1 will compute the monotonic, increasing measurement of a subject as they progress through the gait cycle.

Interpolating Filter

The raw thigh angle IMU measurement can contain high frequency noise generated by impacts occurring at heel strike. Filters that help estimate joint angular position and velocity have proven to be particularly helpful in bipedal robots [115] and nonlinear control applications [15]. In the case of measuring the phase variable, the raw thigh angle can be estimated and filtered by applying a least squares method to fit an analytical function over a rolling data window [16]. This window length can be tuned in order to have minimal delay and reduce high frequency noise. Furthermore, the thigh velocity is estimated by taking the analytical derivative of the estimated thigh angle function to provide the signals in computing the thigh phase portrait. The benefits will be exploited in Section 3.3.2 showing results of the raw IMU measurement applying this filter method.

To compute the interpolating filter polynomial functions for both thigh angle and velocity from the method in [16], the raw thigh angle measurement $\psi(t)$ is stored in a vector of size based on the chosen window length W (in samples). Each row contains a polynomial function given in the following matrix equation form:

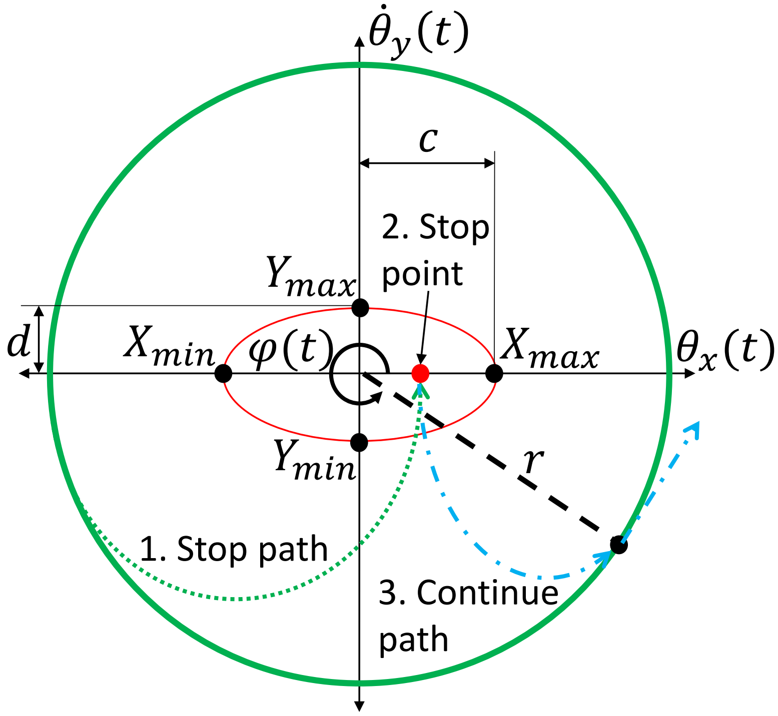

Figure 3.5. A depiction of the phase variable $\varphi(t)$ measured from the circular orbit (thick green line) with a polar radius r (dashed black line) within the thigh phase portrait ($\theta_x(t)$, $\dot{\theta}_y(t)$) coordinates. The ellipse (red line) displays the predefined minimum and maximum X/Y coordinates (black dots) as well as its length of semi-axes c and d. A schematic for how start and stop detection method from Section 3.3.1 is used for a sequence of events. If a subject were to stop walking, the signal travels off the circular orbit (1. Stop path, dotted green line) to inside the ellipse (2. Stop point, red dot) near the origin. When the subject decides to continue walking then the orbital path continues (3. Continue path, dash-dot blue line) to the last recorded phase variable value to complete the stride along the circular orbit.

$$\begin{bmatrix} 1 & 0 & \cdots & 0 \\ 1 & \Delta t & \cdots & (\Delta t)^N \\ \vdots & \vdots & \vdots & \vdots \\ 1 & W\Delta t & \cdots & (W\Delta t)^N \end{bmatrix} \begin{bmatrix} a_0(t) \\ a_1(t) \\ \vdots \\ a_N(t) \end{bmatrix} = \begin{bmatrix} \psi(t+(0-W)\Delta t) \\ \psi(t+(1-W)\Delta t) \\ \vdots \\ \psi(t+(W-W)\Delta t) \end{bmatrix},$$

where Δt is the time step between samples, N is the degree of the polynomial, and $[a_0(t), a_1(t), \ldots, a_N(t)] \in \mathbb{R}^{N+1}$ are the time-varying polynomial coefficients. Constraints are included to bias the new computed coefficients by equaling the terminal coefficients from the previous solved polynomial. This ensures continuity for consecutively generated polynomials with overlapping windows.

Solving for the unknown coefficients $a_i(t)$ for $i \in 0, \ldots, N$ by way of QR factorization [28] yields the interpolating polynomial functions

$$\theta(t) = a_0(t) + a_1(t)h + \ldots + a_N(t)h^N \tag{3.2}$$

$$\dot{\theta}(t) = a_1(t) + 2a_2(t)h + \ldots + Na_N(t)h^{N-1}, \tag{3.3}$$

where $h = (1 - \eta)W\Delta t \in (0, W\Delta t]$ defines the specified time within the window. The parameter $\eta \in [0, 1)$ is a user-defined delay based on the percentage of the window length W. Eq. 3.2 and Eq. 3.3 are the estimates for thigh angle and velocity, respectively.

Adaptive Phase Variable Shift and Scale

The linearity of the phase variable trajectory can be improved by making the orbit in the thigh phase portrait more circular. Both $\theta(t)$ and $\dot{\theta}(t)$ are shifted about the origin of the thigh phase portrait, and the angle $\theta(t)$ is scaled to match the amplitude of the velocity $\dot{\theta}(t)$ to provide a constant orbital radius. The min/max values of the filtered angle $\theta(t)$ and velocity $\dot{\theta}(t)$ are stored for computing the shift and scale by evaluating

$$\theta_{min}(t) = min\{\theta(\hat{t}) \mid \hat{t} \in [t_{\theta_{max}}, t)\}$$

$$\dot{\theta}_{min}(t) = min\{\dot{\theta}(\hat{t}) \mid \hat{t} \in [t_{\dot{\theta}_{max}}, t)\}$$

$$\theta_{max}(t) = max\{\theta(\hat{t}) \mid \hat{t} \in [t_{\theta_{min}}, t)\}$$

$$\dot{\theta}_{max}(t) = max\{\dot{\theta}(\hat{t}) \mid \hat{t} \in [t_{\dot{\theta}_{min}}, t)\},$$

where the min/max time values $(t_{\theta_{max}}, t_{\dot{\theta}_{max}}, t_{\theta_{min}}, t_{\dot{\theta}_{min}})$ correspond to the time a local extrema occurs for the thigh angle and velocity of the previous gait cycle. The minimum values are calculated over a time window starting from the previous gait cycle's maximum, and vice versa. For example, $\theta_{max}(t)$ is the maximum thigh angle from all samples stored in the time interval of $[t_{\theta_{min}}, t)$.

The shift and scale parameters from Eq. 3.1 are then computed by

$$\theta_x(t) = z(t) \cdot (\theta(t) + \gamma(t)) \tag{3.4}$$

$$\dot{\theta}_y(t) = -(\dot{\theta}(t) + \Gamma(t)), \tag{3.5}$$

where $z(t)$ is the scale parameter, and $\gamma(t)$ and $\Gamma(t)$ are the shift parameters calculated from the filtered thigh angle and velocity, respectively, by

$$z(t) = \frac{|\dot{\theta}_{max}(t) - \dot{\theta}_{min}(t)|}{|\theta_{max}(t) - \theta_{min}(t)|}, \quad \gamma(t) = -\left(\frac{\theta_{max}(t) + \theta_{min}(t)}{2}\right),$$
$$\Gamma(t) = -(\dot{\theta}_{max}(t) + \dot{\theta}_{min}(t))/2.$$

The negation in $\dot{\theta}_y(t)$ ensures that the phase portrait of the thigh angle orbits in a counter-clockwise direction. This establishes an increasing and monotonic phase variable from $\operatorname{atan2}(y, x)$. This derivation is based on placing the IMU on the right leg. If the IMU were to be placed on the left leg, then only negating $\theta_x(t)$ is required to produce an increasing and monotonic phase variable along the gait cycle.

Real-Time Start and Stop Detection

If a human subject were to instantly stop walking during a stride, small disturbances from the real-time thigh angle measurements can generate false orbits on the phase portrait, resulting in unwanted signals for the phase variable $\varphi(t)$. When stop walking event occurs the orbit will drive near the origin. Consequently, the phase variable will reset instead of holding the last phase variable value until the subject continues along completing the gait stride. Thus, a start and stop walking detection algorithm is implemented to handle this event, where the phase portrait coordinates $(\theta_x(t), \dot{\theta}_y(t))$ are compared to an elliptical boundary centered around the phase portrait origin.

The phase portrait coordinates in Eq. 3.4 and Eq. 3.5 can be compared to a predefined ellipse

$$\frac{(\theta_x(t) - X)^2}{c^2} + \frac{(\dot{\theta}_y(t) - Y)^2}{d^2} \leq 1, \tag{3.6}$$

where (X, Y) defines the center of the ellipse, and c and d represent the length of the major and minor semi-axes, respectively. These ellipse parameters are obtained from predefined minimum and maximum X/Y coordinates $\{X_{min},\ X_{max},\ Y_{min},\ Y_{max}\}$ with respect to the thigh phase portrait coordinates $(\theta_x(t), \dot{\theta}_y(t))$. The center of the ellipse and the semi-axes are evaluated as

$$X = (X_{max} + X_{min})/2, \quad Y = (Y_{max} + Y_{min})/2,$$
$$c = |X_{max} - X_{min}|/2, \quad d = |Y_{max} - Y_{min}|/2.$$

Fig. 3.5 gives a depiction of the ellipse and its parameters within the phase portrait.

If Eq. 3.6 produces a value less than or equal to one, then it indicates the human has stopped walking (stop detected). Algorithm 1 applies this condition in line 2 to ultimately hold the output phase variable $\varphi_f(t)$ (i.e., $\varphi_f(t)$ is the output of the start/stop logic with $\varphi(t)$ as the input) constant until walking resumes. To ensure continuity in $\varphi_f(t)$ after detecting walking, line 5 clears the *stopped* flag when the absolute error between $\varphi_f(t - \Delta t)$ and $\varphi(t)$ is less than $\Delta\varphi$, a predefined value of acceptable discontinuity. The monotonic filter in line 9 contains two inequalities for an acceptable decrease between the current and previous $\varphi_f(t)$ value, to allow the phase variable transition from 2π to 0 in the phase portrait at the start of a new gait cycle.

Normalizing the output of Algorithm 1 by $\varphi_{norm}(t) = \varphi_f(t)/2\pi$, gives a unit scaled version of the phase variable corresponding to 0 to 100% of the gait cycle. The parameter $\varphi_{norm}(t)$ is considered the final normalized phase variable output for gait phase detection.

Algorithm 1 : Start and Stop Detect with Monotonic Filter

Input: $\varphi(t)$
Output: $\varphi_f(t)$

```
Initialize φ_f(t) = φ(t), stopped = false;
if stop detected then
    stopped = true;
else
    if |φ(t) − φ_f(t − Δt)| ≤ Δφ then
        stopped = false;
    end if
end if
if stopped = true or −3π/2 < φ(t) − φ_f(t − Δt) < 0 then
    φ_f(t) = φ_f(t − Δt);
else
    φ_f(t) = φ(t);
end if
```

Gait Speed Estimate

An additional parameter within the phase portrait provides an estimate for gait cadence: the orbit's polar radius r. From the phase portrait $(\theta_x(t), \dot{\theta}_y(t))$ coordinates, the polar radius of the orbit is computed as $r = \sqrt{\theta_x(t)^2 + \dot{\theta}_y(t)^2}$. The polar radius has a linear correlation to the subject's gait speed. Section 3.3.2 will provide experimental results for how the phase variable and cadence estimate performed across multiple speeds.

3.3.2 Preliminary Results on Real-Time Human-Inspired Phase Variable[3]

An experimental setup and real-time data processing was the next step to verify the safety in using the phase variable algorithm prior to wearing the prosthesis. An able-bodied subject experiments demonstrate the ability of the phase variable to accurately parameterize gait progression for different walking/running speeds (1 to 9 miles/hour). Our results show that this real-time method can also estimate gait speed from the same IMU sensor.

Experimental Protocol and Setup

The experimental protocol for testing was reviewed and approved by the Institutional Review Board (IRB) at UTD. The experiment consists of an able-bodied subject walking on a treadmill with the IMU sensor mounted to the thigh along the sagittal plane (see Fig. 3.4). The measured IMU sensor signals were transmitted to a dSPACE DS1007 2 GHz processor, where the phase variable algorithms from Section 3.3.1 were programmed in MATLAB/Simulink for real-time computing.

The testing involved a human subject initially walking on a treadmill from rest to 1 mph (miles/hour). Treadmill speed was increased by 1 mph increments in a continuous sequence up to the subject's selected running speed (9 mph). For each speed, 45 seconds of data were recorded. The experiment ended with the subject returning back to a rest position.

Real-Time Thigh Angle and Velocity Results

The raw thigh angle $\psi(t)$ measured by the IMU sensor was processed using the interpolating filter from Section 3.3.1 (Fig. 3.6). The raw thigh angle $\psi(t)$ produced sharp cusps near the local maxima values, which are fully removed using the interpolated filtered thigh angle $\theta(t)$. The interpolated filtered thigh velocity $\dot{\theta}(t)$ removes the large impulses created from ground impacts as velocity crosses 0.0 rad/s. As a comparison, a second order (5 Hz cutoff) Butterworth low-pass filter is shown in Fig. 3.6. It can be seen the Butterworth filter fails to smooth out the impacts, which would result in a non-monotonic phase variable. Hence, the interpolated filter is the preferred filter method for this application. The amount of delay created by the interpolating filter is considered acceptable since it is less than the delayed reaction time from the reflex pathways of gait locomotion [120]. Applying the shift-and-scale method from Section 3.3.1, the orbit in the thigh phase portrait becomes circular, which yields a monotonically increasing phase variable through Eq. 3.1.

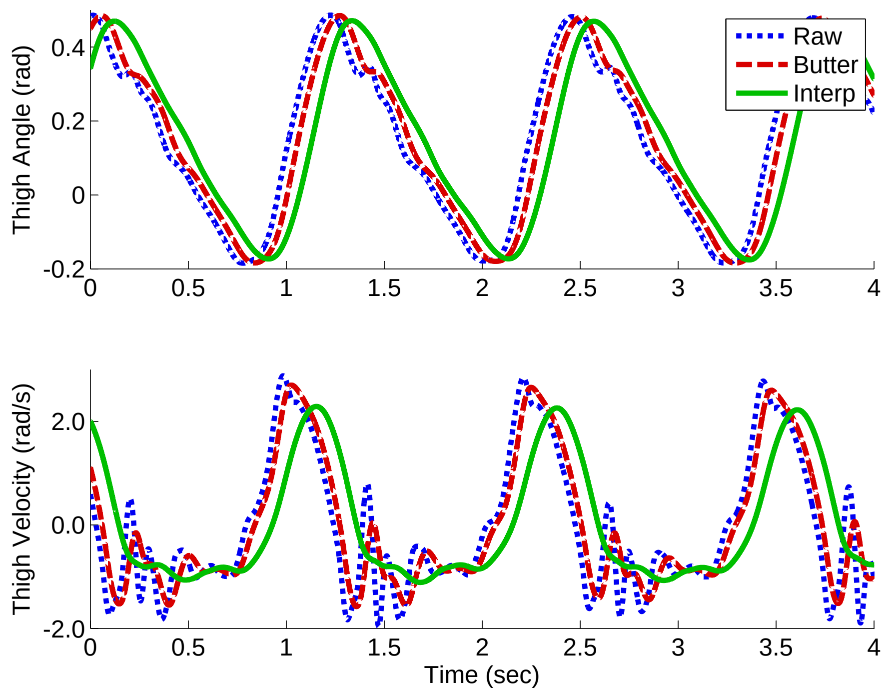

Figure 3.6. Top: the thigh angle (Raw) measured by the IMU (dotted blue line) compared against two filtered options: 1) a second order Butterworth (Butter) low-pass filter with a cutoff frequency of 5 Hz (dashed red line) and the Interpolating (Interp) filter method (solid green line). Bottom: the thigh velocity (numerically differentiated thigh angle) and the two filtered options. Signal disturbances from ground impact are observed in the thigh velocity (e.g., $t \approx 1.3$ and 2.6 seconds). The Interpolating filter provides a more smooth signal than the Butterworth filter. Data is from 3 mph treadmill speed test.

Applying the method from Section 3.3.1, the phase portrait from the raw thigh angle and velocity traces a stretched, distorted elliptical orbit (Fig. 3.7). This will produce a non-monotonic polar angle that is not useful for determining the phase of gait. However, including the shift and scale parameters (Eqs. 3.4 and 3.5) in the computation of the phase portrait coordinates produces a more defined circular orbit. This in fact yields a monotonically increasing phase variable function output (Eq. 3.1).

The resulting phase portrait forms a consistent circular orbit centered around the origin, with a minor indentation pattern in the lower quadrants. Notice that although the velocity magnitude decreases in this region, the polar angle continues to increase. Thus, the phase

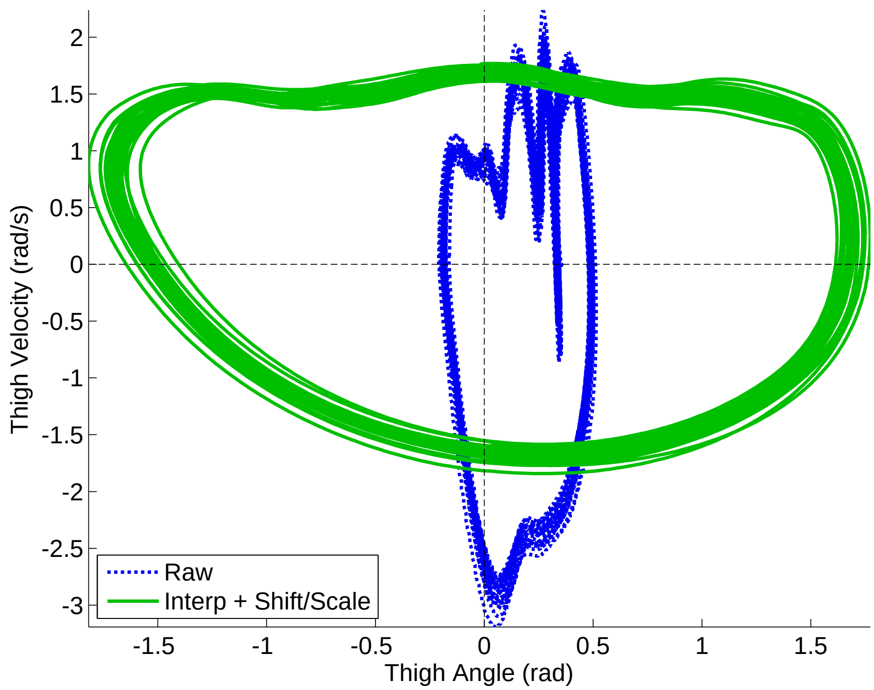

Figure 3.7. The raw thigh orbit (Raw) compared to the interpolated filtered, shifted/scaled thigh orbit (Interp + Shift/Scale) in the phase plane for 20 continuous strides at 3 mph. Applying the shift and scale algorithm produces a circular orbit shape, in contrast to the raw non-circular orbit.

portrait measurement using atan2 makes the phase angle $\varphi_m(t)$ less sensitive to velocity fluctuations during the center portion of the angle oscillations, and vice-a-versa.

Continuous Gait Phase Variable Across Varying Speeds

Fig. 3.8 shows the results of continuous, monotonic phase variables ($\varphi_{norm}(t)$) over time across gait speeds. The shaded region represents the standard deviation, which displays a tight tolerance against the mean showing consistency in the data over consecutive strides. As expected, the slower to normal walking speeds (1-3 mph) took longer time durations to complete gait strides compared to the faster speeds. The slower speed phase variables are not perfectly linear, which is expected as the subject's phase transitions are not uniformly paced throughout the gait cycle. The phase variable reflects the fact that each leg spends more time in stance than swing during slow to normal walking.

For the faster speeds (4-9 mph), the phase variable becomes increasingly linear as the stance and swing transition period becomes symmetrical over the gait cycle [116, 44]. Markers display the timing of toe-off (defined by the minimum thigh angle during stride), which coincides with the beginning of the swing period [77]. The slope increases from initiation of swing period (i.e., toe-off) and beyond, which indicates the subject's transition from stance-to-swing period [116, 77]. The lower and upper lines between 0.42 and 0.47, respectively, bound the phase variable values that were observed at the stance-to-swing transition across the different speeds. The phase variable consistently predicts stance-to-swing transition within these tight bounds despite wide changes in the timing of the transition across different speeds (indicated by the x-axis of Fig. 3.8).

Gait Speed Estimator

Fig. 3.9 displays the phase portrait for various gait speeds. The polar radius r is distinct for each speed along the orbit. Fig. 3.10 displays the linear relationship of treadmill walking speed versus the polar radius (with a coefficient of determination $R^2 = 0.994$). The least squares regression fit produces a function $v(r) = 2.45r - 1.13$ for estimating walking speed from polar radius. The variance of the estimate is reduced when using the mean polar radius from a single quadrant of the phase portrait (Fig. 3.10), where the fourth quadrant (phase angle between $3\pi/2$ and 2π) was chosen.

The experimental results produce a continuous measurement of gait phase that is reliable across multiple speeds. A real-time method using a single wearable IMU sensor on the thigh validated the phase variable that parameterizes the human gait cycle. A variation of this phase variable approach is used for controlling the powered knee-ankle prosthesis in a unified manner throughout the entire gait cycle [86].

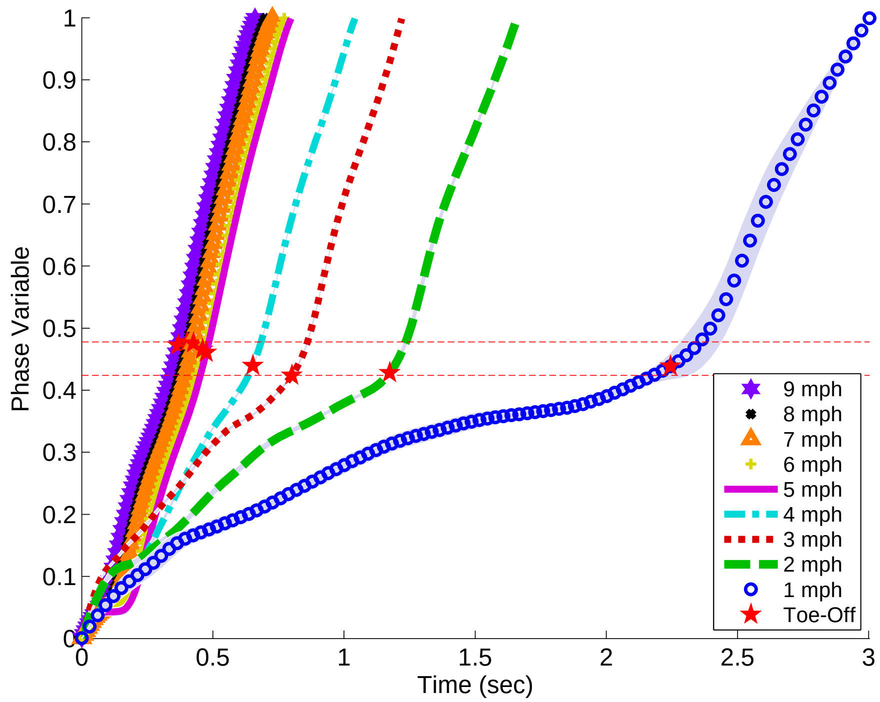

Figure 3.8. The normalized phase variable $\varphi_{norm}(t)$ vs. time across various treadmill speeds (1-9 mph) for 20 consecutive gait strides. Each phase variable curve represents the mean for that particular speed with ± 1 standard deviation (shaded gray region, difficult to observe due to small variance). Toe-off is marked (red star) at the moment when the minimum thigh angle occurred. Horizontal red dashed lines give the lower and upper bounds of these events across the various speeds, demonstrating the ability of the phase variable to predict these events despite differences in timing. The slower speeds (1-3 mph) have a nonlinear phase trajectory due to a longer time duration in stance compared to swing, whereas faster speeds ($\geq$ 4 mph) produce a linear phase trajectory due to a more even stance/swing split [116].

3.3.3 UTD Leg Control Loops[4]

This section presents the control scheme implemented on the powered knee-ankle prosthesis for amputee experiments. The outer loop performs high-level joint position control to enforce periodic virtual constraints parameterized by a human-inspired phase variable. We then

[4]© 2018 IEEE. Reprinted, with permission, from D. Quintero, D. J. Villarreal, D. J. Lambert, S. Kapp, and R. D. Gregg, Continuous-Phase Control of a Powered Knee-Ankle Prosthesis: Amputee Experiments Across Speeds and Inclines, IEEE Transactions on Robotics (TRO), Accepted January 2018.

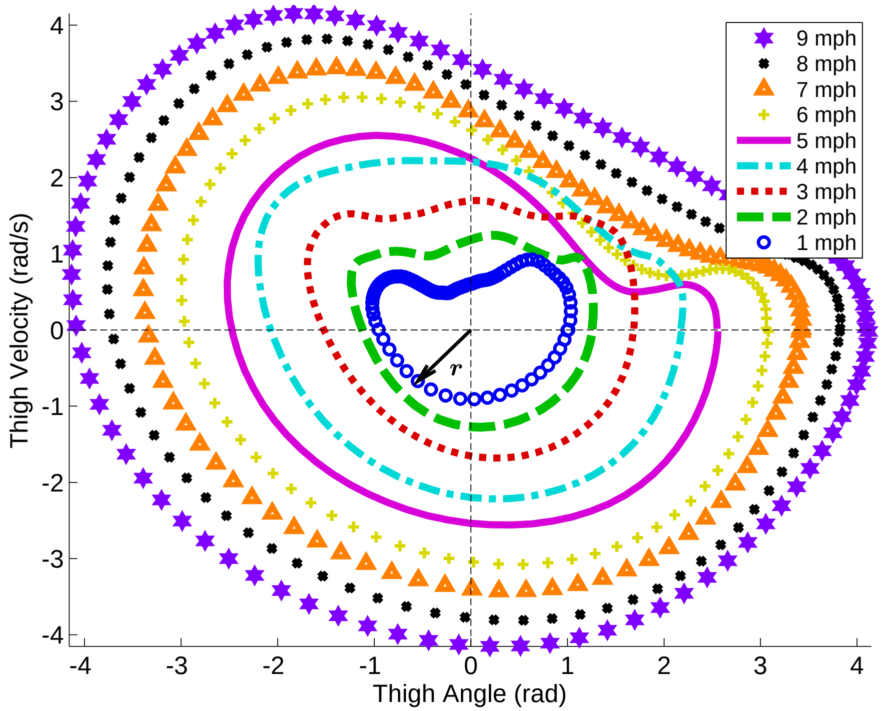

Figure 3.9. The phase portrait of $\dot{\theta}_y(t)$ vs. $\theta_x(t)$ across various treadmill speeds (1-9 mph) each having 20 consecutive gait strides. The polar radius r can be correlated to the subject's gait speed. Speeds $\leq$ 4mph produced a circular orbit from 0 to 2π (i.e., 0% to 100% gait cycle). At 5 mph, the subject transitioned from fast walking to running, where more forceful ground impacts can be observed in the IMU measurements due to the flight phase. This produced a non-circular form after impact with intersection of other orbits at different speeds, as shown in the first quadrant for 5-6 mph.

describe an inner loop that performs low-level torque control based on torque commands from the outer loop controller. These two control loops are depicted in Fig. 3.11.

Human-Inspired Phase Variable Implementation

The phase variable algorithms was motivated by a study in [113] showing that the thigh phase angle robustly parameterizes ipsilateral leg joint patterns during non-steady human walking, e.g., across perturbations. This choice of phase variable also has connections to biology, as hip motion is known to be a major contributor to synchronizing the leg joint patterns in mammals [92].

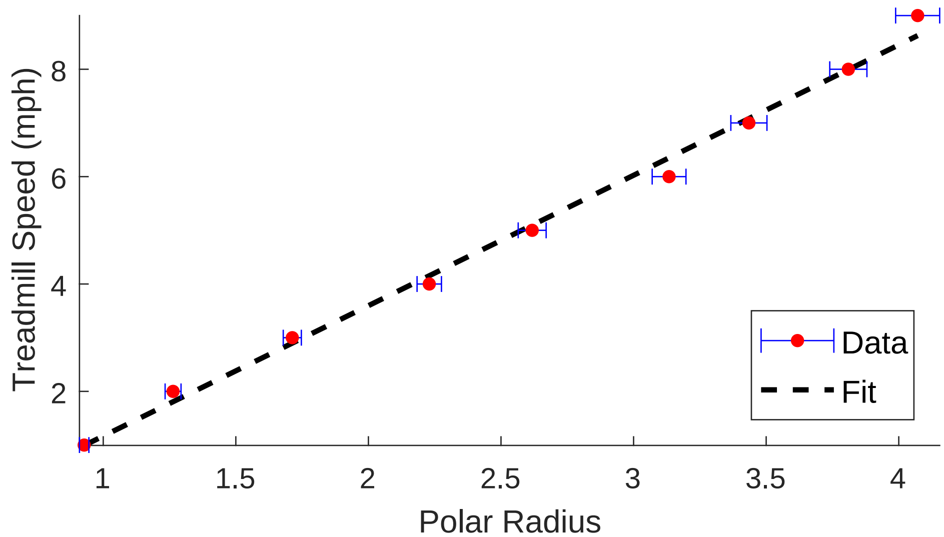

Figure 3.10. Treadmill speed vs. mean polar radius r (Data) with regression line $v(r)$ (Fit). Note the error bars (horizontal blue lines) are ± 1 standard deviation from the mean (red dots).

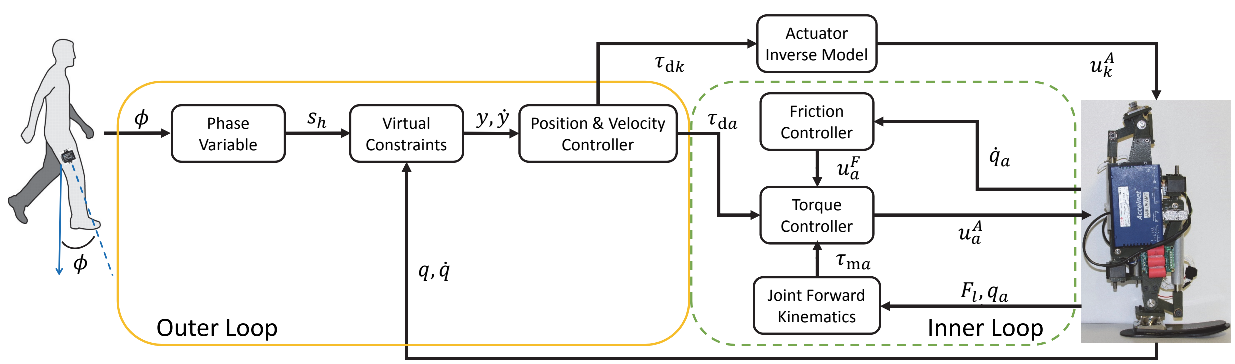

Figure 3.11. The control architecture for the prosthesis comprises an outer and inner loop. The outer loop computes the desired joint torques (Eq. 3.10) needed to enforce the virtual constraints (Eq. 3.9) based on the mechanical phase variable (Eq. 3.7). The desired knee torque τ_{dk} is converted to current commands for the knee motor driver (u_k^A) using an inverse model of the knee actuator. The current commands for the ankle motor driver (u_a^A) are computed by an inner loop (Eq. 3.13) that provides closed-loop torque control with a friction compensator.

Although the thigh phase angle can be easily computed offline from post-processed kinematic data [113], real-time computation presents a challenge for implementation in a prosthetic control system. With regards to derivation in Section 3.3.1, the thigh phase angle can be computed from the angular position and velocity [53, 45], but angular velocity is prone to noise and makes the control system relative degree-one [112]. We instead computed a phase angle $\vartheta(t)$ utilizing thigh angular position $\phi(t)$ and its integral $\Phi(t) = \int_0^t \phi(\tau)\, d\tau$. The thigh angle integral behaves as a low-pass filter to the IMU measurement, which provided additional smoothing of the phase angle signal from unwanted disturbances as experienced in the phase variable preliminary experiments in Section 3.3.2. All other algorithms in Section 3.3.1 remained the same with the exception of the thigh angular velocity being replaced with its thigh angle integral to give the following form:

$$\begin{aligned} \vartheta(t) &= \text{atan2}(\Phi_y(t), \phi_x(t)), \\ \phi_x(t) &= (\phi(t) + \gamma) \\ \Phi_y(t) &= z(\Phi(t) + \Gamma) \end{aligned} \tag{3.7}$$

where the scale factor z, the thigh angle shift γ, and the thigh integral shift Γ are given by

$$\begin{aligned} z &= \frac{|\phi_{max} - \phi_{min}|}{|\Phi_{max} - \Phi_{min}|}, \\ \gamma &= -(\frac{\phi_{max} + \phi_{min}}{2}), \quad \Gamma = -(\frac{\Phi_{max} + \Phi_{min}}{2}). \end{aligned}$$

These parameters center the thigh orbit around the origin and maintain an approximately constant orbital radius, which the linearity improves for the phase variable trajectory (see Fig. 3.12).

The integral is reset every gait cycle to prevent the accumulation of drift due to variation in thigh kinematics. The scale and shift parameters are recalculated every quarter gait cycle, i.e., at each axis crossing in the phase portrait. Because these updates occur when the phase angle radius is collinear with the axis, the phase angle calculation (Eq. 3.7) remains

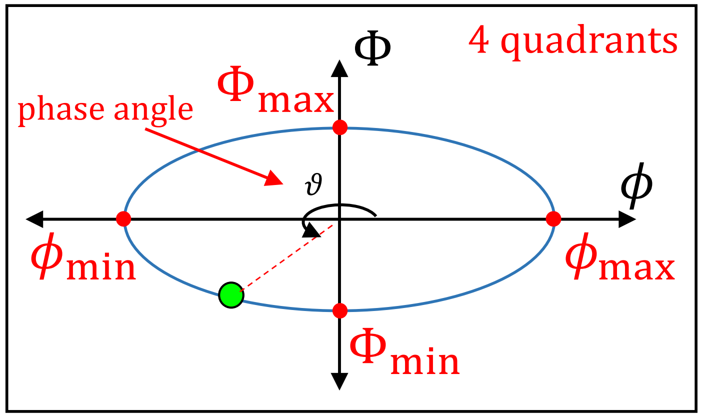

Figure 3.12. A phase portrait of the thigh angle ϕ and its integral Φ with the thigh phase angle ϑ measured about the circular orbit to determining the phase variable. Each axis crossing of the phase angle will contain either a max or min value of the thigh angle or its integral to determining the phase variable shift and scale factors (see Eq. 3.7).

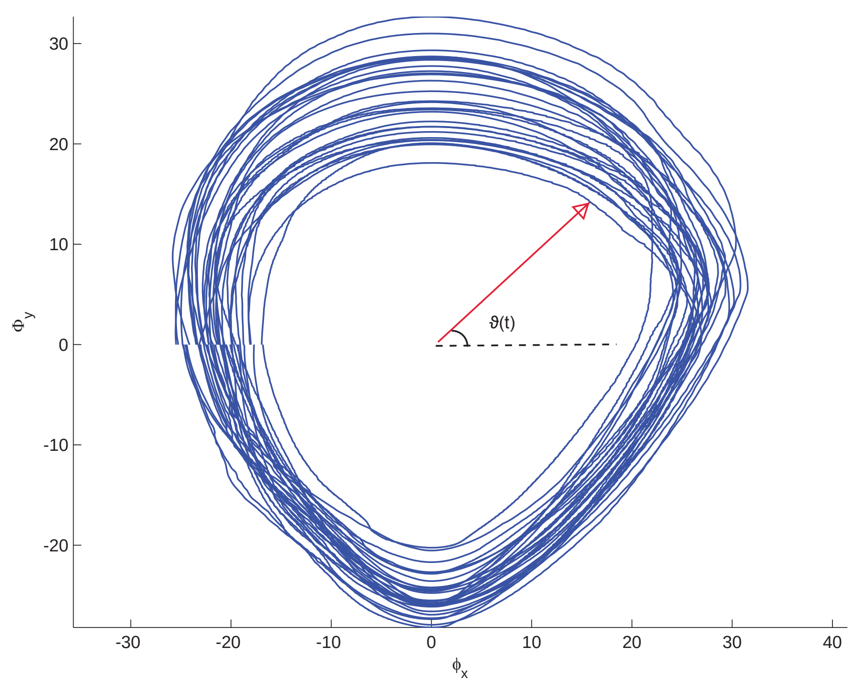

Figure 3.13. Phase plane of the thigh angle $\phi_x(t)$ vs. its integral $\Phi_y(t)$ during prosthetic leg experiments (Section 3.4.2). The phase plane has been scaled by z and shifted by (γ, Γ) to achieve a circular orbit across the stride, which improves the linearity of the phase variable $\vartheta(t)$.

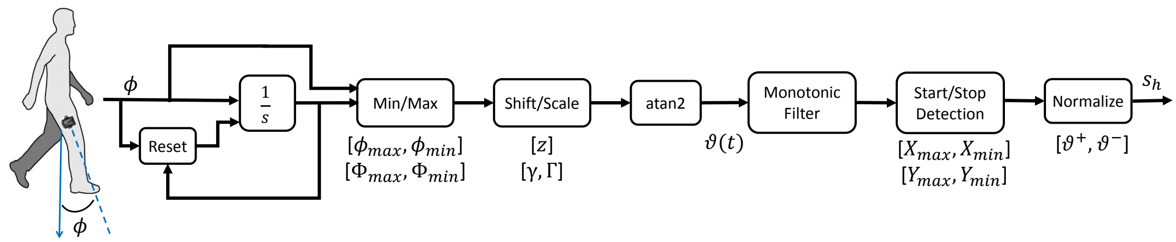

Figure 3.14. Phase variable block diagram of each major component computed. The raw hip angle measured ($\phi(t)$) from the IMU is feed through an integrator ($\Phi(t)$) with a reset condition for when the circular orbit has completed within the phase portrait. Then the parameters ($\phi(t), \Phi(t)$) are sent to compute the minimum/maximum and the shift/scale values from the phase portrait x-y axis . The atan2 function is evaluated ($\vartheta(t)$) prior to the safety subsystems of the monotonic filter and start/stop detection algorithms, which then outputs the normalized phase variable s_h.

continuous. Fig. 3.13 shows the scaled/shifted orbit in the thigh phase plane over several strides, where changes in circular orbit diameter are associated with changes in walking speed. Finally, the phase angle ϑ from Eq. 3.7 is normalized similar to Eq. 2.2 with the final normalized phase variable given as

$$s_h(\vartheta) = \frac{\vartheta - \vartheta^+}{\vartheta^- - \vartheta^+}, \tag{3.8}$$

constants $\vartheta^+ = 0$ and $\vartheta^- = 2\pi$. Fig. 3.14 displays a block diagram of the phase variable and the subsystems used to compute the final normalized value in s_h.

Outer Control Loop

The outer loop controller coordinates the knee and ankle patterns of the prosthetic leg by enforcing virtual constraints based on a common phase variable (see Fig. 3.11). Virtual constraints encode the desired motions of actuated variables in output functions to be zeroed through the control action [115]:

$$y_i = q_i - h_i^d(s_h), \tag{3.9}$$

where q_i is the measured angular position of joint i (with $i = k$ for the knee or $i = a$ for the ankle), and h_i^d is the desired joint angle trajectory as a function of the normalized phase variable $s_h \in [0, 1)$. Then the method described in Section 2.2 is used to design h_k^d and h_a^d, and s_h in Section 3.3.3 for application to the powered prosthesis.

Eq. 3.9 is considered the tracking error of the control system. Various torque control methods can be utilized to regulate this error. Bipedal robots typically enforce virtual constraints using input-output feedback linearization [115, 37, 102, 89, 10, 40, 64], which has appealing theoretical properties including exponential convergence [50], reduced-order stability analysis [115], and robustness to model errors [102]. However, to apply feedback linearization to a prosthesis, the dynamics of the prosthesis and the interaction forces with the human user and ground must be known [32, 61]. Identifying a sufficiently accurate model of the prosthetic leg is difficult, and measuring interaction forces requires expensive multi-axis load cells. Therefore, we utilize a model-free torque control method in this application, specifically output PD control [32, 85].

Output PD controllers typically have the form:

$$\tau_{di} = -K_{\mathrm{p}i} y_i - K_{\mathrm{d}i} \dot{y}_i, \tag{3.10}$$

where $K_{\mathrm{p}i} > 0$ is the proportional gain affecting the stiffness of joint i about its angular trajectory, and $K_{\mathrm{d}i} > 0$ is the derivative gain correcting velocity tracking error $\dot{y}_i$. Controlling both the position and velocity of the output is helpful for tracking the desired trajectories, but can create forceful interaction with the human user. More compliant, smooth behavior can be achieved by replacing $\dot{y}_i$ with the measured angular velocity $\dot{q}_i$ in Eq. 3.10. This was done in the knee controller for user comfort, but the ankle controller was left in the form of Eq. 3.10. This PD control method determines the joint torques needed to enforce the virtual constraints.

Inner Control Loop

The torque commands of the outer loop (Eq. 3.10) are converted into current commands for the BLDC motor drivers in two ways. The desired input current to the knee motor is determined by dividing the desired knee torque by the motor's torque constant (0.0136 Nm/A) and the estimated gear ratio between the motor and joint. To provide compliant and forceful interaction with the ground, the ankle torque command is enforced by a closed torque loop (the inner loop in Fig. 3.11). The torque loop compensates for the actuator dynamics and external loads to reduce torque tracking error. The torque loop has two parts: a Proportional-Integral (PI) controller based on torque feedback and a friction compensator to reduce the effects of the ball screw transmission.

The friction compensator is defined as a function of ankle joint velocity:

$$u_a^F(t) = (F_C + F_v|\dot{q}_a(t)|)\,\mathrm{sgn}(\dot{q}_a(t)), \tag{3.11}$$

where $F_C = 0.3$ is the Coulomb friction coefficient and $F_v = 0.01$ is the viscous friction coefficient of the ankle actuator. The torque PI controller is given by

$$u_a^\tau(t) = -K_\mathrm{p}^\tau\, e_a(t) - K_\mathrm{I}^\tau \int_0^t e_a(\sigma)\, d\sigma, \tag{3.12}$$

where $e_a = \tau_{\mathrm{m}a} - \tau_{\mathrm{d}a}$ is the ankle torque error between the measured torque $\tau_{\mathrm{m}a}$ and the desired torque $\tau_{\mathrm{d}a}$. The measured torque $\tau_{\mathrm{m}a}$ is determined by the ball screw linear force F_l and the angle of attack of the ball screw to the lever arm from the ankle joint forward kinematics (see Fig. 3.11). The torque proportional gain K_p^τ compensates for the current values of the error, while the torque integral gain K_I^τ reduces the offset between the measured and desired torques as error accumulates over time. Finally, the desired motor current

$$u_a^A = u_a^F + u_a^\tau \tag{3.13}$$

is sent to the ankle motor amplifier, which runs an internal current loop.

3.3.4 From Rhythmic to Volitional Control

This section discusses an altered version of the phase-based control scheme used in the clinical case study described in Chapter 5 for non-rhythmic motion. In general, human walking is a steady rhythmic motion during gait. Yet, during daily life there are non-rhythmic motion or, in other words, volitional locomotion performed by a human. Volitional locomotion activities may include swaying back/forth during stance or swing period, walking forward/backward transitions, ambulating over an obstacle, or performing such tasks as kicking a soccer ball. Some volitional control of powered prostheses involve a finite state machine approach with new impedance-based controllers and switching rules, while having a higher-level locomotion mode recognition to detect the volitional activity [122, 123]. Other approaches use electromyography (EMG) signals placed on the residual limb, where pattern recognition techniques are implemented to control the volitional movement of the prosthesis [38, 46]. Generally, EMG sensors are a time consuming task for probe placement, the sensors have dynamic noise from reading muscle activation, and intent recognition classifiers can give false detection by way of muscle fatigue from a subject. The method of virtual constraints can be applicable for performing overground volitional control activities.

The unified phase-based controller presented in Section 3.3.3 is tailored for rhythmic motion while capturing a periodic orbit in regards to thigh angle phase portrait to obtain a continuous sense of phase [113]. To handle volitional control activities, a piecewise holonomic phase-based control was developed for tailoring non-rhythmic motion. The aim was to incorporate a holonomic virtual constraint, where the desired joint kinematic trajectories of human data from [116] as well as described in Section 2.2 were parameterized against a piecewise phase variable defined from the motion of the thigh angle along gait. The piecewise manner comes from computing phase variables for the stance (s_{st}) and swing (s_{sw}) period in the following form:

$$s_{st}(q_h) = \frac{q_h^{max} - q_h}{q_h^{max} - q_h^{min}}\kappa \tag{3.14}$$

$$s_{sw}(q_h) = 1 + \frac{1 - s_{st}^f}{q_h^{max} - q_h^{min,f}}(q_h - q_h^{max}), \tag{3.15}$$

where q_h is the measured thigh angle, q_h^{max} and q_h^{min} are tunable maximum and minimum thigh angle, respectively, s_{st}^f is the last value of s_{st}, $q_h^{min,f}$ is the last value of q_h^{min}, and κ

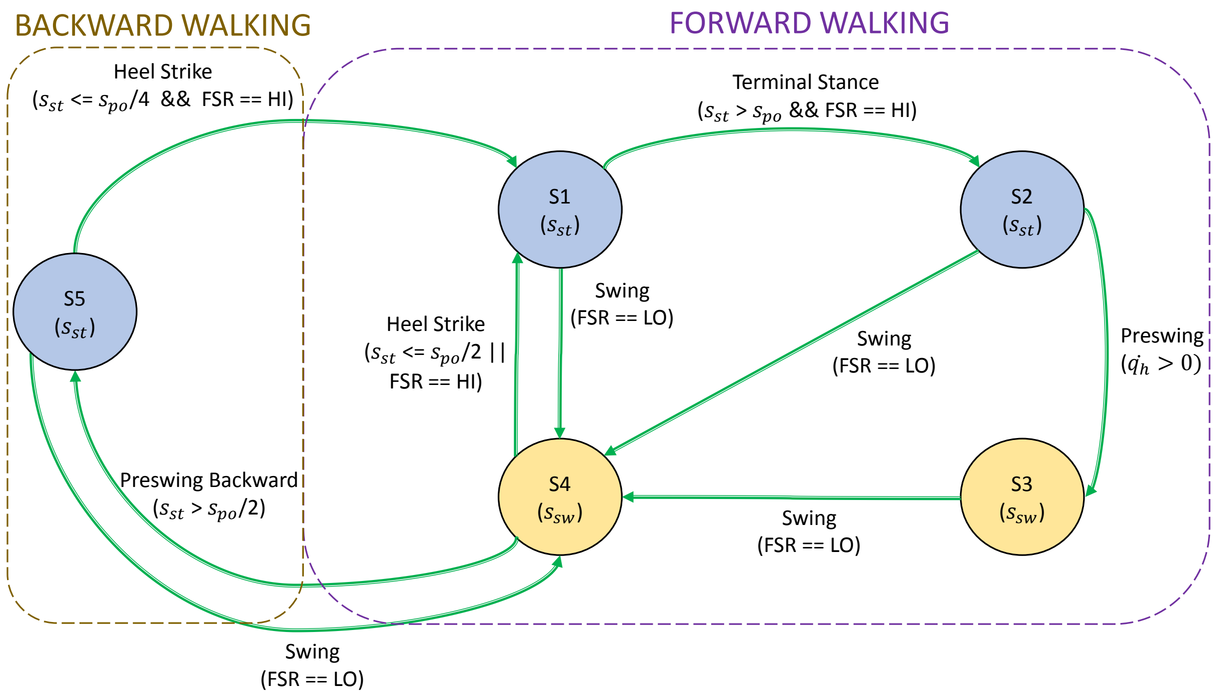

Figure 3.15. A finite state machine for using a piecewise phase variable for performing stance or swing for either forward or backward walking. The blue circles refers to Eq. 3.14 and yellow circles refers to Eq. 3.15. Between each state there are transition rules that consist in evaluating s_{st} about ankle push-off threshold s_{po}, FSR sensing for ground foot contact (HI) or no contact (LO), or thigh velocity $\dot{q}_h$ changing sign during preswing.

is a tune parameter for when s_{st} is at a minimum thigh angle q_h^{min} during gait. The main distinction to determine which phase variable to use comes from the FSR sensor presented in Section 3.2 for detecting when a subject is in stance or swing. When FSR is reading a high voltage threshold value (foot is in contact with the ground) it indicates the subject is in stance period (HI equals binary value of 1). If the FSR reads a low voltage threshold value then it indicates the subject is in swing period (LO equals binary value of 0). The high and low voltage threshold values are tuned to voltage readings when the subject is standing on the leg and when the leg is off the ground, respectively.

To utilize these phase variables for when a subject is in either stance or swing, a finite state machine was implemented. Fig. 3.15 represents a four state FSM (S1-S4) to perform the states of forward walking and an additional state (S5) for backward walking. The FSM transitions rules between states determine when a transition should occur to output the phase variable for either stance (Eq. 3.14) or swing (Eq. 3.15) control for the leg within the gait cycle. The forward walking states in Fig. 3.15 performs sequential transitions to complete a gait cycle with the ability to exit at any point to go to swing motion (S4). The FSM begins at state S1 for heel-strike with using Eq. 3.14 stance phase variable. As the FSR equals HI and s_{st} becomes greater than the predefined ankle push-off phase variable s_{po}, the transition from S1 to S2 occurs as the subject progresses towards terminal stance. Then as the subject approaches preswing to swing from the change in sign of thigh velocity $\dot{q}_h$, the phase variable output switches from using s_{st} to s_{sw}. The switch is a smooth transition as Eq. 3.15 has an adaptable parameter that captures the last stance phase variable value s_{st}^f from Eq. 3.14. Note, the transitions from S1 to S3 are intended to be unidirectional in its sequence. The benefit with this sequential approach is to have ankle push-off occur at the moment it should perform along gait as preswing initiates before entering swing period. From S3 the subject will transition to S4 while still in swing control before returning to S1 at heel-strike as the FSR goes HI to continue to the next stride. State S4 has significance that it is an exit strategy for the other states S1-S3 to transition into swing when FSR goes LO. This allows a subject to have volitional control at any point in stance to instantly transition to swing motion.

The underlying volitional control provides motion with regards to instant changes to performing either forward or backward walking. The state S5 takes in effect if a subject were to swing their thigh in a backward motion and then make contact to the ground, to then ambulate backwards bypassing the transition to S1 for forward walking sequence. S4 to S5 is focused on the region of s_{st} with regards to s_{po} in determining if the thigh is in backward motion while observing if s_{st} value has passed beyond the push-off threshold s_{po}. If backward motion occurs while being in state S5, the subject can continue to move backwards in stance control without approaching the value of s_{po} to perform push-off. To conclude, Eq. 2.6 is parameterized by the piecewise phase variable from Eqs. 3.14 and 3.15 for virtual constraint control, similar to the form in Eq. 3.9 described in Section 3.3.3. This control scheme will be utilized for experiments for non-rhythmic motion experiments for overground walking discussed in Chapter 5. The finite state machine subsystem was implemented in MATLAB/Simulink as part of the real-time control and can be seen in Fig. C.11.

3.4 Prosthesis Performance Evaluation

3.4.1 Benchtop Performance

The section covers benchtop testing performed on UTD Leg 1 prior to walking experiments. Several test cases were performed for characterizing the actuation system and quantifying the performance of leg. Characterization testing was limited to the ability to perform the test by way of test equipment availability while having the constraint of it not being a destructive test. Therefore, motor friction characterization and closed loop frequency response testing was able to be performed. Step responses and duty cycles were also performed to determine the transition responses of each joint actuator system.

Actuation Performance

Prior to installing the motors to the actuator assembly, a motor friction characterization test was conducted to aid in potential future work for modeling the system. The motor used for the leg (Section 3.1) was mounted to a vertical faceplate fixture in order to conduct the test. For identifying a friction model, a formula for the friction effect can be represented in the following form:

$$F_f(v) = F_s \,\mathrm{sgn}(v) + F_\sigma v,$$

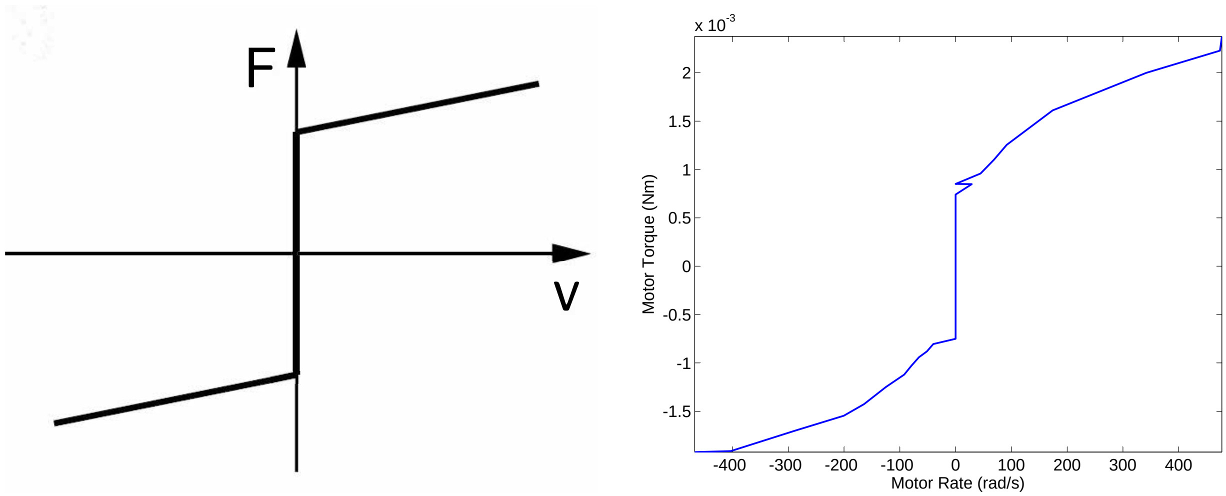

Figure 3.16. An example representation of a Viscous friction with Coulomb friction versus velocity effect (left). Actual motor torque versus motor rate performed on the Maxon motor (right) closely resembles the friction force element model on the left.

where F_s is the Coulomb friction parameter and F_σ is the viscous friction parameter [4]. The friction model defines the Coulomb parameter F_s as the normal force times the friction coefficient to produce a static friction. The viscous friction is a linear force with respect to the sliding velocity pressing surfaces together. The test consist of commanding a range of positive and negative motor torque values in torque control mode, while measuring motor rate. The empirical results in Fig. 3.16 can determine the friction parameters for F_f as $F_s = 0.76$ Nm and $F_\sigma = 0.00413$E-3 Nm-s, so its possible to use these parameters as part of the build-up of an actuator model to perform model-based control strategies.

For this is a first generation prototype, a full friction characterization test of the overall actuator could not be performed due to lack of test equipment availability and the potential of being a destructive test with large desired rate transitions. Future actuator characterization can be performed for UTD second generation Leg (Leg 2), which has recently been built in late 2017 [19]. Each joint for Leg 2 has a rotating actuator design with the ability to characterize the actuator system itself as it is can be a standalone subassembly unit. Leg 1

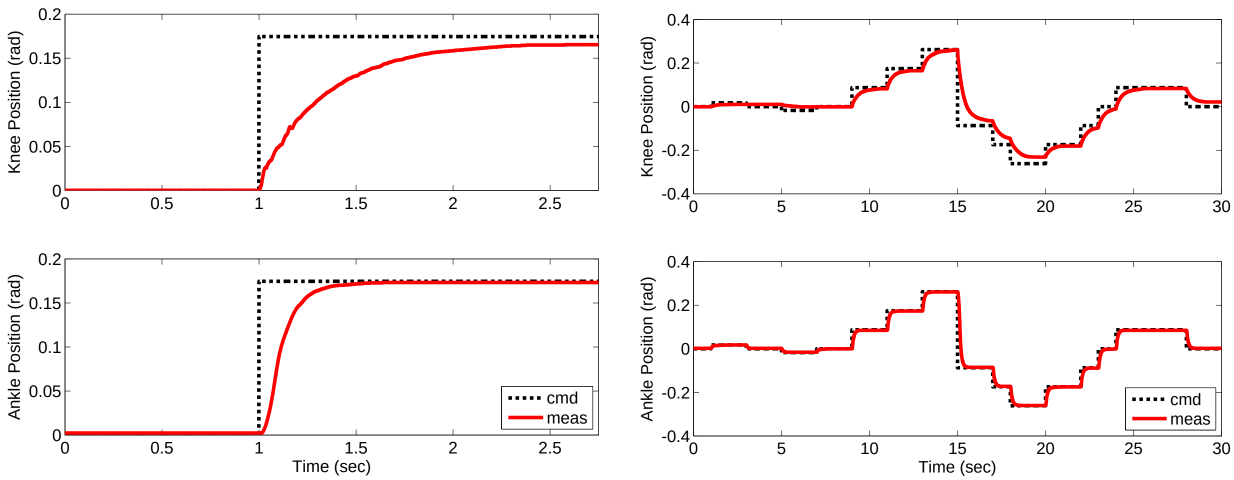

Figure 3.17. Left Column: Knee (top) and Ankle (bottom) angular position step response. The dotted black line is the desired command at 0.1745 radians and the solid red line is the joint actuation response output. Right Column: Knee (top) and Ankle (bottom) angular position step duty cycle response. The dotted black line is the desired step commands at multiple positions and the solid red line is the joint actuation response output.

was built as an entire assembly and does not have the ability for a single actuator subassembly unit to test.

Table 3.2. Step Response Characteristics for UTD Prosthetic Leg

	Knee	**Ankle**
Rise Time (sec)	0.917	0.205
Peak Time (sec)	2.57	1.64
Settling Time (sec)	-	1.48

To evaluate the system performance, a linear Proportional-Derivative (PD) controller was implemented in position mode to control the leg joints individually. The PD controller consist of a control law $u_{PD} = -K_p(\theta - \theta_d) - K_d\dot{\theta}$, where θ_d is the desired joint angular position, θ is the measured joint angular position, $\dot{\theta}$ is the measured joint angular velocity, K_p is the proportional gain affecting the stiffness of the joint, and K_d is the derivative gain behaving as a damping term. Gains were manually tuned to achieve small steady-state tracking error. Step inputs were evaluated at each joint to obtain dynamic response characteristics

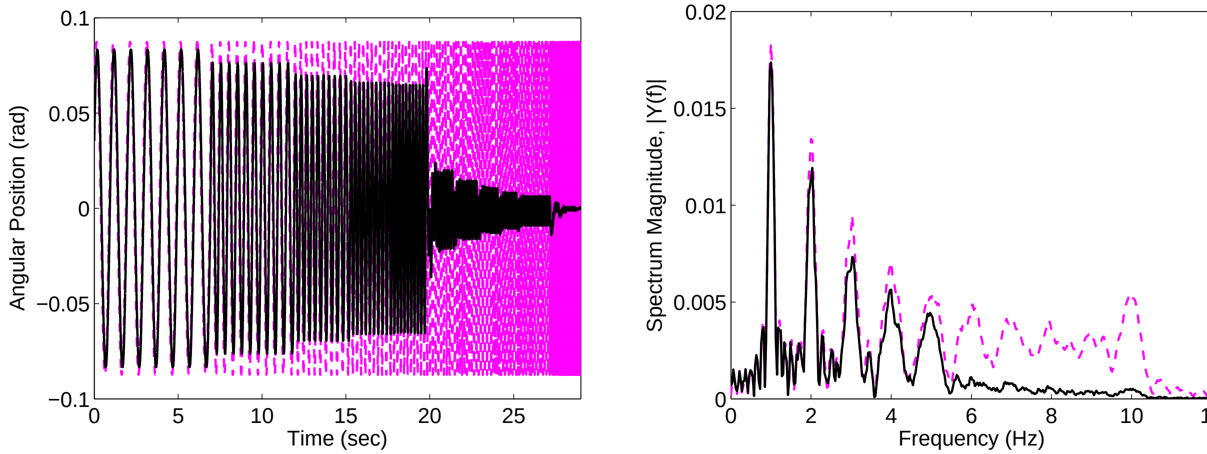

Figure 3.18. Left: Commanded versus measured angular position of a sinusoidal frequency sweep for the ankle joint. The pink dashed line is the desired command and the black solid line is the joint actuation response output. Right: Frequency spectrum analysis between the commanded signal and the measured signal for the ankle joint.

to evaluate the performance of the system. A position step input of 10 degrees (0.1745 radians) was commanded separately for both knee and ankle (see left column of Fig. 3.17). Response characteristics were computed and presented in Table 3.2. The ankle step response has better performance with faster response and settling time than the knee. Note the knee's actuation system receives a larger inertia to overcome with the opposing moment due to the mass of the leg during free swing. Thus, the knee has a slower response time compared to the ankle, where the settling time could not be computed based on its undershoot response. Control gains were selected for stable responses. Gains were increased to improve the control response of the knee, but under disturbances it proved to be unstable so gains were returned to lower values.

A step duty cycle was commanded to both joints individually to evaluate transient responses during small time durations (see right column of Fig. 3.17). The desired position commands applied in order were [0, 0.01745, 0, -0.01745, 0, 0.08727, 0.1745, 0.2618, -0.08727, -0.1745, -0.2618, -0.1745, -0.08727, 0, 0.08727, 0] radians at various time intervals over time length of 30 seconds. Again the ankle actuator was able to meet the desired commanded

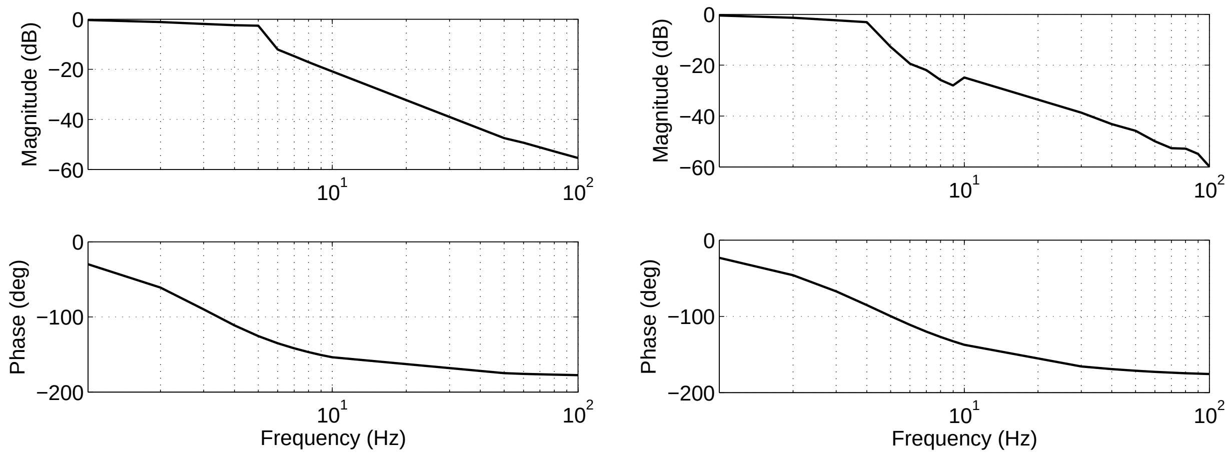

Figure 3.19. Empirical results of closed-loop frequency response of UTD Leg 1 ankle (left) and knee (right).

position, while the knee had steady-state error due to its undershoot behavior response. However, experimentation with the leg attached to amputees, an aided torque will be applied to the knee joint due to the moment created from the thigh motion during swing period. These results are preliminary benchtop testing. Future work may entail performing system identification techniques to accurately determine the open loop bandwidth of each actuator. Its important to note it may potentially be a destructive test, particularly for the knee, if a full open loop frequency response test is to be performed.

To characterize the closed loop system, a frequency response test was performed at each joint. For example, the test consisted of commanding a position sine sweep at different frequency values and measuring the response from the ankle (Fig. 3.18). The frequency sweep was performed at increments of 1 Hz from 1 to 10 Hz and then afterwards increments of 10 Hz up to frequency of 100 Hz. Using a joint PD controller to track a position sine sweep, benchtop experiments determined that the closed-loop position bandwidth (defined by -3 dB magnitude crossover frequency) exceeds 3.5 Hz at each joint (Fig. 3.19). This performance is sufficient for tracking human joint trajectories during walking (frequencies up to 2 Hz) [58, 116].

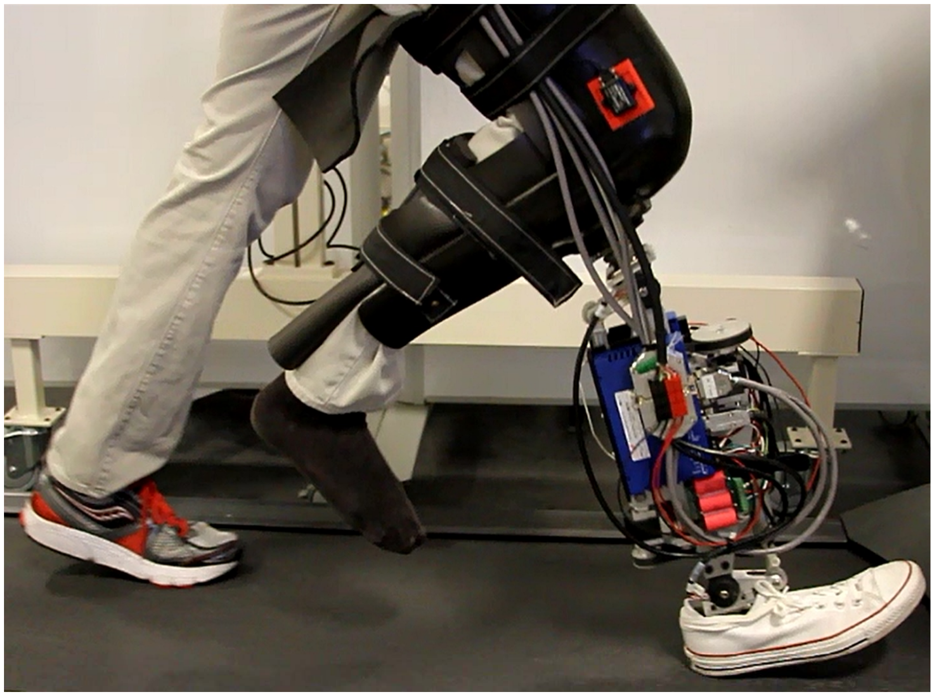

Figure 3.20. Photo of able-bodied human subject walking on the powered prosthesis through a leg-bypass adapter during treadmill experiment. The IMU can be seen attached to a red mount on the bypass adapter.

3.4.2 Preliminary Able-Bodied Subject Experiments with Fixed Virtual Constraints[5]

Experimental Setup and Protocol

Benchtop experiments were first performed to tune the two control parameters $(K_{\mathrm{p}i}, K_{\mathrm{d}i})$ per joint (Eq. 3.10) in order to determine starting parameters for walking experiments. The parameters were tuned with the prosthesis attached to the bench while an able-bodied subject walked on a treadmill at their comfortable walking speed (2.0 miles/hour (mph)) with the IMU sensor mounted fixed to their thigh along the sagittal plane to compute the phase variable. The leg was controlled by the virtual constraints as the subject walked

[5]© 2016 IEEE. Reprinted, with permission, from D. Quintero, D. J. Villarreal, and R. D. Gregg, Preliminary Experiments with a Unified Controller for a Powered Knee-Ankle Prosthetic Leg Across Walking Speeds, IEEE/RSJ International Conference on Intelligent Robots and Systems (IROS), 2016.

continuously. Control parameters were then tuned until tracking error was reduced while observing the prosthesis as it synchronized with the subject's leg during walking. After the initial control parameters were determined, the leg was mounted onto the bypass adapter for the able-bodied subject experiments.

The experimental protocol was reviewed and approved by the Institutional Review Board (IRB) at The University of Texas at Dallas. Experiments were conducted with an able-bodied subject wearing the powered prosthesis through a leg-bypass adapter while walking on a treadmill (Fig. 3.20). Prior to recording data, the subject was given time to acclimate to the prosthetic leg. During this time only one parameter was adjusted for the comfort of the human subject. Specifically, the knee joint's proportional gain $K_{\mathrm{p}k}$ was lowered for less forceful interaction with the subject. A smaller knee proportional gain was required during walking because of the thigh motion produced by the human, which created an aiding moment at the prosthetic knee joint. Note that the subject's comfortable walking speed during initial testing with the powered prosthesis was 1.5 mph.

The experiment with variable walking speeds began with the subject at rest on a treadmill. Walking was initiated by setting the treadmill speed to 1.0 mph. The treadmill speed was increased by increments of 0.5 mph after about 15 seconds of comfortable, steady walking at each speed. The highest walking speed reached was 3.0 mph. After walking at the fastest speed, the subject lowered speed to 2.0 mph and then 1.0 mph before settling back to rest. The same controller was used for all walking speeds.

A gait speed classifier is also implemented to automatically update the joint kinematics of the virtual constraints as walking speed changes for joint specific kinematics. These results demonstrate that the unified control approach can perform multiple activities for multiple users without re-tuning control parameters, which could drastically reduce the configuration time of powered knee-ankle prostheses compared to state-of-art methods [109]. Beyond speed classifiers, there are many classification techniques that can be implemented for this virtual constraint control framework for task-specific control [83, 48, 111, 119].

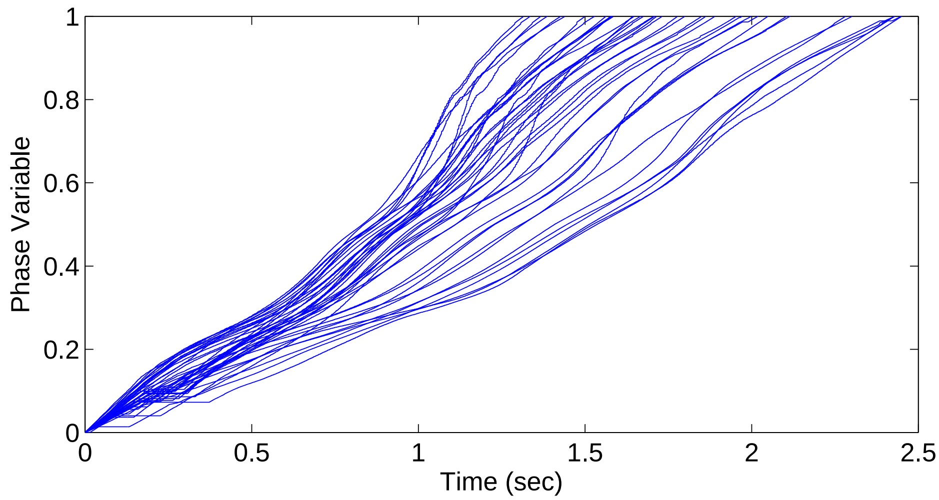

Figure 3.21. The normalized phase variable over raw time per stride for 40 continuous strides at various walking speeds (1 to 3 mph). The phase variable is monotonic and approximately linear for all strides, where the slope of the trajectory depends on the walking speed. Flat regions can be observed between 0 and 0.4 sec in a few trajectories, which are the result of a zero-order hold to enforce monotonicity during non-steady walking motions (i.e., the first few steps after starting from rest).

Experimental Results

A supplemental video of the experiment is available for download in [86]. The video demonstrates the subject's control over the prosthetic joints through their thigh motion. Fig. 3.21 shows the phase variable (computed from the phase plane in Fig. 3.13) over time for 40 continuous strides between 1.0 to 3.0 mph. The trajectories with shallower slopes over a longer time period correspond to slower walking, whereas the steeper slopes over a shorter time period correspond to faster walking. The slope of the phase variable trajectory influenced the speed of the commanded joint trajectory through Eq. 3.9, by which the prosthetic leg adapted its kinematics to the user's walking speed. The mean and standard deviation of the phase variable are shown over normalized time in Fig. 3.22. Overall, the phase variable exhibited a consistent, linear trajectory, which enabled consistent, smooth behavior for the prosthetic leg. The small variability about the mean can be attributed to transient changes in speed between treadmill settings and normal variability between the durations of stance

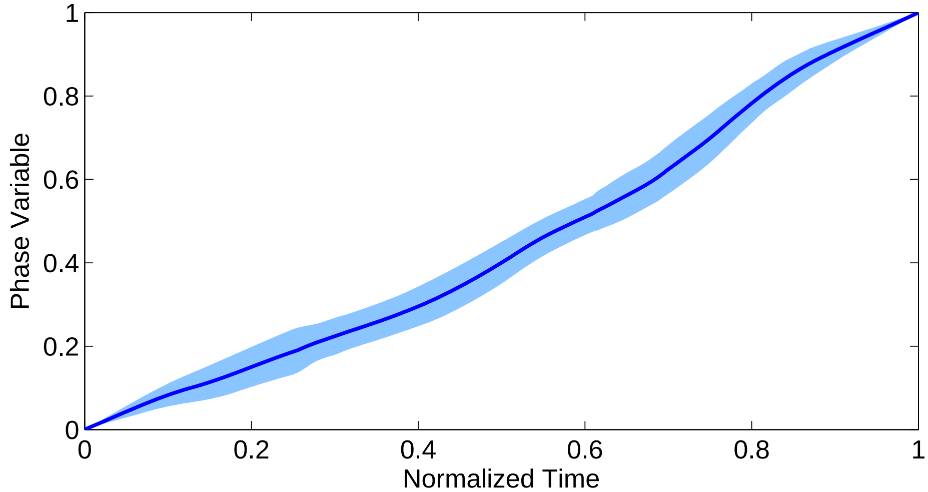

Figure 3.22. The normalized phase variable over normalized time per stride at various walking speeds (1 to 3 mph). The average trajectory (blue solid line) and ±1 standard deviation (shaded region) are computed across 40 continuous strides. The phase variable is strictly monotonic and approximately linear across the gait cycle.

vs. swing. For example, gait cycles with a longer stance period and shorter swing period would account for shallower slopes between 0 and 0.6 normalized seconds in Fig. 3.22.

For the experiments, the DFT virtual constraints in Fig. 3.23 were designed from able-bodied human data for normal walking speed [116]. Fig. 3.24 displays the mean and standard deviation of the commanded and measured joint angles over the phase variable. The commanded signals exhibit negligible variance, which was expected from the definition of virtual constraints as functions of the phase variable (the x-axis of Fig. 3.24). The larger variations of the measured joint angles demonstrate the flexibility afforded by the controller as external forces change with speed. Some phase delay can be observed in tracking the commanded signal, which the control gains were tailored for the comfort of the subject and produced more tracking error. Efforts at shifting the phase variable to compensate for this phase delay did not prove beneficial in these experiments. For a different perspective, the joint kinematics are shown over normalized time in Fig. 3.25. The variations in the commanded signals are associated with variations of the measured phase variable within gait cycles (Fig. 3.22).

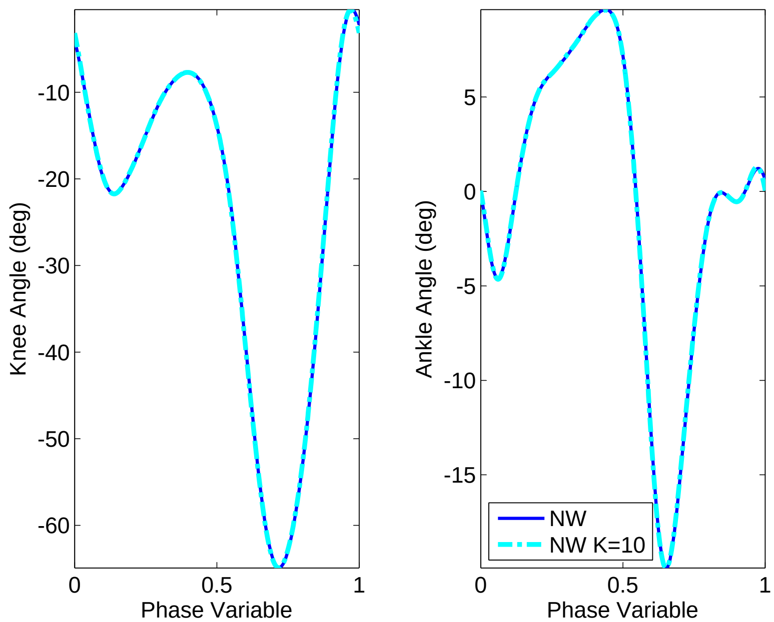

Figure 3.23. The desired joint trajectory and the virtual constraint by DFT with $K = 10$ (see Eq.2.6) for the knee (left) and ankle (right) with normal walking (NW) speed for an entire gait cycle. The reference data from [116] is indicated with solid lines and the virtual constraint is indicated with broken lines. Note, the knee angle is defined from the thigh to the shank and the ankle angle is defined from the shank to the foot (minus 90 deg). Both angles follow the right-hand rule.

The motor current commands sent to the motor drivers were measured across the various walking speeds (Fig. 3.26). These motor commands roughly correspond to output torque at the joints through a nonlinear mapping based on the dynamics and kinematics of the actuator transmission. The ankle demanded the highest torque during a noticeable powered push-off (phase variable between 0.5 to 0.6) at the end of stance. The knee required the most torque during late stance (knee flexion) and late swing (knee extension).

3.4.3 Gait Speed Classifier Experiments

To emulate joint speed specific kinematics, a gait speed classifier was implemented to demonstrate the user viability of automatically switching between different virtual constraints as walking conditions change. This brings the possibility of using our task-specific control ap-

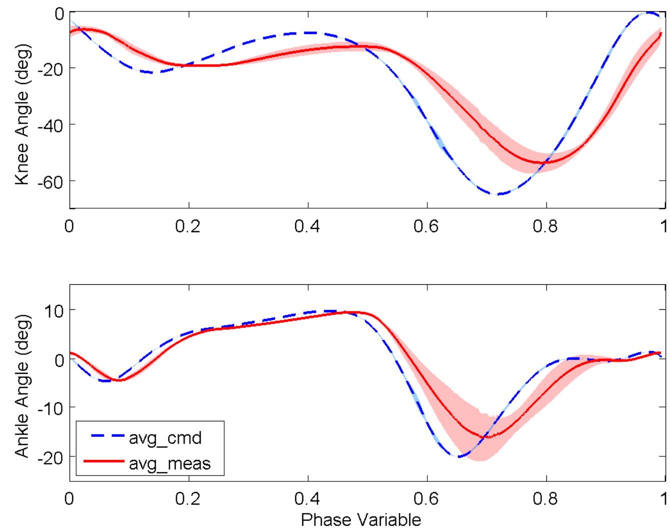

Figure 3.24. Joint kinematics of the prosthetic knee (top) and ankle (bottom) over the phase variable at various walking speeds (1.0 to 3.0 mph). The black dashed line is the average commanded angle for each joint. The red solid line is the average measured angle for each joint. The shaded regions represent ±1 standard deviation about the mean. The averages and standard deviations are taken over 40 continuous strides. The control system reasonably tracked the commanded angles from the virtual constraints, which were designed from healthy human data in Fig. 3.23.

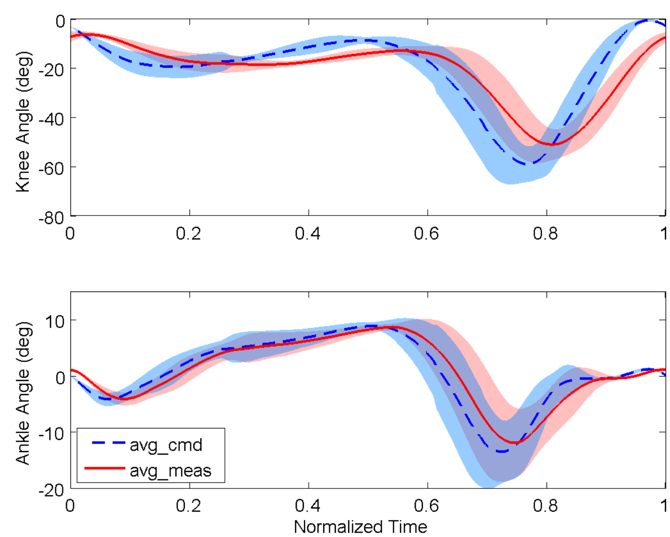

Figure 3.25. Joint kinematics of the prosthetic knee (top) and ankle (bottom) over normalized time at various walking speeds (1.0 to 3.0 mph). The black dashed line is the average commanded angle for each joint. The red solid line is the average measured angle for each joint. The shaded regions represent ±1 standard deviation about the mean. The averages and standard deviations are taken over 40 continuous strides.

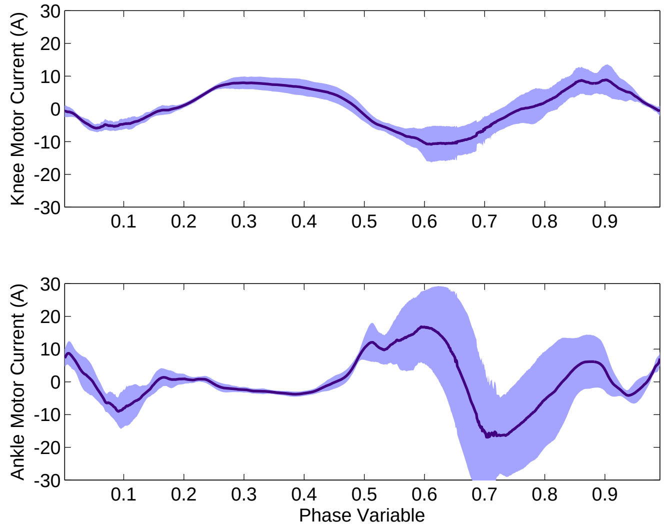

Figure 3.26. The commanded motor currents from the controller for the knee (top) and ankle (bottom) over the phase variable at various walking speeds (1.0 to 3.0 mph). The knee requires the most current during the swing period (phase variable between 0.6 to 1.0), and the ankle current peaks during late stance (phase variable between 0.5 to 0.6) as powered push-off injects energy to propel the prosthetic leg into swing motion. Note, push-off occurs around phase variable of 0.6.

proach in a higher-level task state machine. A finite state machine classified between slow (1.5 mph), normal (2.0 mph), and fast (2.5 mph) walking speeds based on the cadence of the subject. The cadence of each stride was calculated by taking the inverse of the amount of time between prosthesis heel strikes. The classifier selected the walking speed by comparing the most recent cadence measurement to non-overlapping intervals centered about the average pre-recorded cadence for each speed. Note, other gait speed classifier methods can also be implemented, such as the one described in Section 3.3.2.

An “autospeed” experiment was performed separately using the classifier on the prosthesis as the subject accelerated from slow to normal to fast walking in a continuous sequence (30 s for each condition). This experiment was performed by an able-bodied subject using a bypass adapter as shown in Fig. 3.20. The best results were obtained with additional damping (i.e., more compliance) in the knee controller. No other control parameters changed.

Fig. 3.27 shows the temporal trajectories of the phase variable for all consecutive strides, demonstrating appropriate changes in slope as walking speed changes. Moreover, the time duration of each stride is grouped around one of the three averages (i.e., slow, normal, and fast), which allowed the classifier to choose the correct virtual constraints for the walking speed. This is confirmed by Fig. 3.28, in which the joint trajectories of each stride are closely grouped around one of the three kinematic averages. These plots also demonstrate that the subject was able to seamlessly transition between speed conditions using the classifier.

3.4.4 Discussion

We developed a single, unified prosthesis controller that captures the entire gait cycle using a periodic virtual constraint driven by a human-inspired phase variable. The unified controller eliminates the need to divide the gait into different periods with independent controllers, reducing the control parameters to tune for each individual subject and walking speed. This could significantly reduce the clinical time and effort to configure a powered knee-ankle prosthesis for an individual subject. The controller was implemented in a powered prosthesis and tested with an able-bodied subject using a bypass adapter to evaluate walking at variable speeds.

The results from Section 3.4.2 used the same controller for all walking speeds, demonstrating adaptability as the human user initiated, accelerated, decelerated, and terminated walking with their thigh motion. Although the controller used fixed virtual constraints based on able-bodied joint kinematics for a specific walking speed, the human subject naturally forced desirable changes in the prosthetic knee and ankle kinematics as the walking speed changed (Fig. 3.24). This behavior approximates the slight variations observed in able-bodied joint kinematics across different walking speeds [116]. The combination of the flexible controller and the subject's intact hip joint enabled appropriate changes in step length as the walking speed changed to achieve a comfortable walking gait. Chapter 4 investigates using

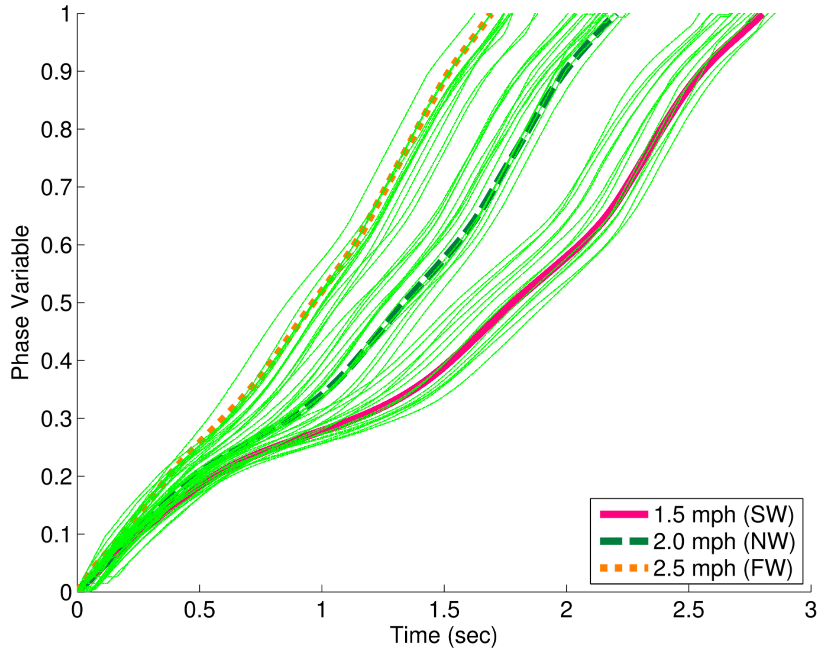

Figure 3.27. Prosthesis phase variable vs. time for a consecutive sequence of strides at slow (SW, 1.5 mph), normal (NW, 2.0 mph), and fast (FW, 2.5 mph) speeds with the autospeed classifier. The mean SW, NW, and FW phase trajectories (thick lines) are shown for reference.

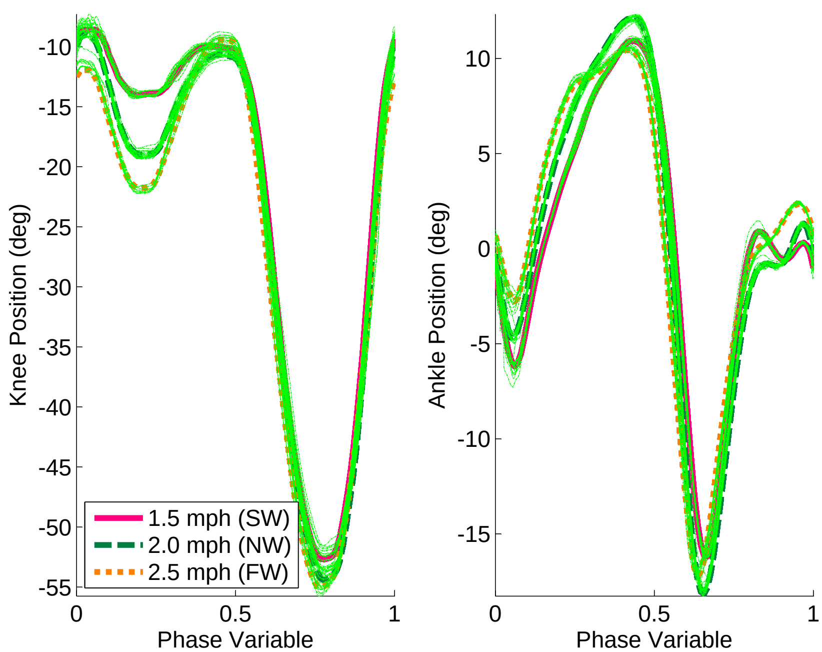

Figure 3.28. Prosthetic joint angles for a consecutive sequence of strides at slow (SW, 1.5 mph), normal (NW, 2.0 mph), and fast (FW, 2.5 mph) speeds with the autospeed classifier. The mean SW, NW, and FW joint trajectories (thick lines) are shown for reference.

task-specific joint commanded trajectories (as in [45]) that could be beneficial to produce the appropriate joint torque and power for effective walking at a particular speed.

The maximum speed achieved in these experiments is on par with the fastest walking speed currently reported in the literature [60] for a powered knee-ankle prosthesis, but our results were achieved with a single controller. This walking speed is substantially faster than typical finite state machine approaches for walking (e.g., [107]), but not as fast as the running-only controller in [99]. To our knowledge, no other controller has been reported for a knee-ankle prosthesis that can vary across such a wide range of walking speeds without adjusting any control parameters. Future efforts include additional control loops, such as closed-loop torque control, which can potentially provide better tracking that may enable faster walking. Preliminary experiments also suggest that comfortable walking can be achieved without retuning control parameters for different human subjects, which is part of the contribution work in Chapter 4.

We then demonstrated in Section 3.4.3 that a task-level finite state machine can pick the appropriate virtual constraints as conditions change, specifically walking speed. A gait speed classifier was implemented to automatically update the virtual constraints as walking speed changes. This was done to demonstrate the viability of using our task-specific control approach in a higher-level task state machine, for which many classification techniques exist [83, 48, 111, 119].

The proposed control approach can be applied equally well to other locomotion activities with well-characterized joint kinematics from able-bodied data, such as walking on slopes or stairs [116]. Furthermore, the clinical viability can be demonstrated by giving clinicians graphical interface to tune the joint trajectories in this control framework, as opposed to iteratively guessing several impedance parameters in a state machine to achieve the intended effect. This will be explored further in Chapter 5. Experiments involving transfemoral amputee subjects to further validate the performance of the powered prosthesis using the unified controller is given in Chapter 4.

CHAPTER 4

TRANSFEMORAL AMPUTEE SUBJECT EXPERIMENTS USING UNIFIED CONTROL ON A POWERED PROSTHESIS[1]

This chapter describes the experimental setup, protocol, and results with three amputee subjects walking at different speeds and inclines. The experimental protocol was approved by the Institutional Review Board (IRB) at The University of Texas at Dallas. Handrails and/or a safety harness were provided to prevent falls, though no adverse events occurred. The hardware knee-ankle robotic leg used during experiments is described in Sections 3.1 and 3.2.

The periodic virtual constraints were parameterized against the thigh phase angle in order to continuously define the desired joint kinematics across strides. In particular, virtual constraints defined with the Discrete Fourier Transform (DFT) encapsulate the property of periodicity [85], which respects the repetitive nature of the gait cycle. The conceptual design of DFT virtual constraints was studied in simulations of an amputee biped model in Chapter 2, demonstrating that the continuous-phase controller can produce stable walking for various walking speeds. Preliminary experiments with this control method were conducted with an able-bodied subject wearing a powered knee-ankle prosthesis through a leg bypass adapter in Section 3.4.2. This chapter expands that work with amputee subject users and investigates the phase-based controller for not just various speeds, but for various slopes of ascent and descent as well.

4.1 Initial Setup and Tuning

The control parameters used in the amputee experiments were determined through benchtop and able-bodied testing. First, the top of the prosthetic knee joint was mounted to a rigid bench. The control parameters in Section 3.3.3 were tuned while the joints tracked walking trajectories based on prerecorded phase variable measurements. After finding a set of control parameters that reasonably enforced the virtual constraints, the prosthesis was mounted onto a leg-bypass adapter that allows an able-bodied subject to walk on the prosthesis. The IMU was mounted above the prosthetic knee joint and aligned in the sagittal plane.

An able-bodied human subject walked on the powered prosthesis as in [86]. After recording several strides of IMU data, a Principal Component Analysis (PCA) was done to compute a transformation matrix that further decouples the Euler angles of the frontal and sagittal planes [52]. Control parameters were then retuned as the able-bodied subject walked on a level treadmill at their comfortable speed. The knee joint parameters were reduced to account for the aiding hip moment and to produce less forceful interaction with the user, resulting in slightly more knee angle tracking error. The ankle torque control parameters (Eq. 3.12) were increased to provide more push-off torque against the weight of the subject. The friction compensator parameters from Eq. 3.11 remained the same.

Table 4.1. Characteristics of Transfemoral Amputee Subjects

Subject	Gender	Height (m)	Weight (kg)	Age (yrs)	Post-Amputation Time (yrs)	Amputated Side
TF01	Male	1.702	87.1	34	18	Left
TF02	Male	1.69	65.8	29	20	Right
TF03	Male	1.78	70.6	37	7	Left

Table 4.2. Ranges of Activities Performed by Transfemoral Amputee Subjects

Subject	Min Speed (mph)	Max Speed (mph)	Min Slope (deg)	Max Slope (deg)
TF01	1.5	2	-2.5	7.5
TF02	1.5	2.7	-2.5	9
TF03	1.5	2.7	-2.5	7.5

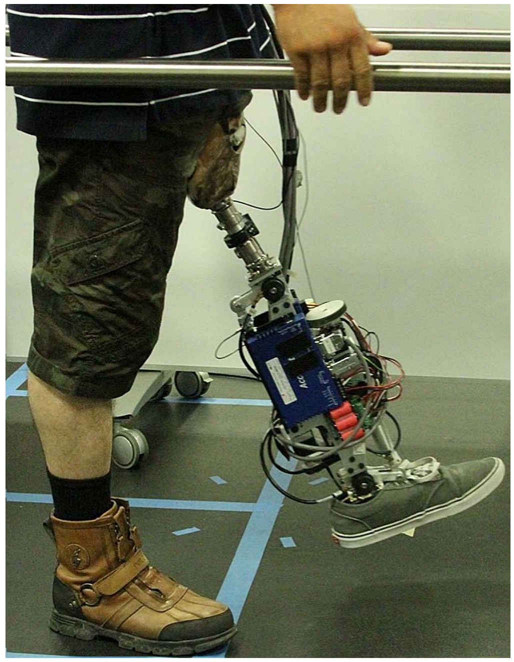

Figure 4.1. Photo of transfemoral amputee subject wearing the powered knee-ankle prosthesis. The IMU sensor is mounted on the pylon between the residual limb socket and the prosthetic knee joint (in the sagittal plane).

4.1.1 Experimental Setup and Protocol

Experiments were conducted with three transfemoral amputee subjects (TF01–03) as reported in Table 4.1. Each subject met the inclusion criteria, e.g., weight less than 113 kg, 18 to 70 years in age, and no neuromuscular disorder or secondary health problems that would prohibit their ability to participate in the study activities. All subjects had zero to minimal experience using a powered prosthesis.

A certified prosthetist attached the powered prosthesis to each subject's current, well-fitting custom socket (Fig. 4.1) and aligned the prosthesis appropriately. The subjects became acclimated to the powered prosthesis by walking overground along handrails for about 20 minutes. The transformation matrix for decoupling the IMU Euler angles was also computed during this period. Once acclimated, the subject participated in treadmill experiments with different speeds and inclines. The same control gains were used across all trials.

The subject first walked on a level treadmill at different speeds with virtual constraints corresponding to slow, normal, or fast kinematics (Section 2.2). Walking speeds are reported in the units of the treadmill, miles per hour (mph). Initially, the subject walked as the treadmill speed incrementally increased to 2.0 mph (0.89 meters/sec) to verify that this was a comfortable, normal walking speed. Then, the slow and fast speeds were defined at 1.5 mph (0.67 meters/sec) and 2.5 mph (1.12 meters/sec), respectively. Individual slow, normal, and fast speed trials were performed at the subject's discretion with the corresponding kinematics for a minimum of 30 seconds to capture a consecutive sequence of steady-state strides. The subject was also given the option to walk at a very fast speed of 2.7 mph (1.21 meters/sec) with the fast kinematics. Trials were then performed at these speeds using fixed normal-speed kinematics to examine the adaptability provided by the phase variable alone.

Next, the subject walked at the normal speed on different treadmill inclines using the corresponding virtual constraints (Section 2.2). The subject started on a slope of -2.5 deg (the minimum slope of the treadmill). Then the slope was incremented by $+2.5$ deg until reaching the user's maximum comfortable slope or $+9.0$ deg (the maximum slope of the treadmill). Walking data was recorded at each slope condition for at least 15 seconds. The subjects also walked successfully on variable inclines using fixed joint kinematics, but those results are withheld for this experimental study.

4.2 Amputee Experimental Results

The range of speeds and slopes achieved by each subject is given in Table 4.2. A supplemental video of all subjects walking across these conditions is available for download in [87]. We first highlight results at the normal walking speed on level ground and then present differences over speeds and inclines.

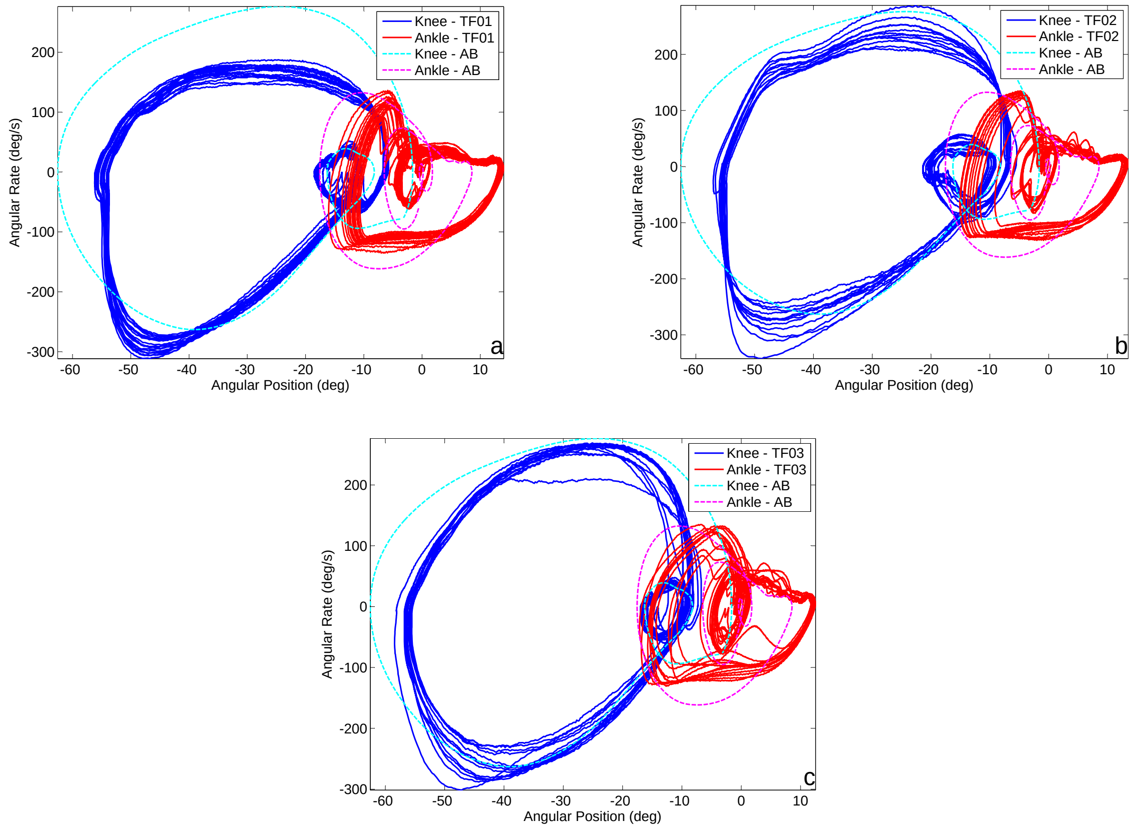

Figure 4.2. Phase portrait of the prosthetic leg (measured joint angular positions versus velocities) over 20 consecutive strides of steady-state, level-ground walking at the comfortable speed (about 2.0 mph) for amputee subjects TF01 (a), TF02 (b), and TF03 (c), compared with averaged able-bodied data (AB) [116]. Note that the prosthetic joints follow similar orbits to the able-bodied data.

4.2.1 Normal Level-Ground Walking

Fig. 4.2 shows the phase portraits of prosthetic joint angles versus velocities for all three amputee subjects walking on level ground at 2.0 mph with the normal-speed virtual constraints. Each subject was able to walk comfortably with the prosthesis and achieve a normative periodic orbit over consecutive strides. The phase portrait of subject TF01 exhibits the least variance due to more consistent hip motion. However, slower hip motion during swing resulted in slower prosthetic knee extension for this subject.

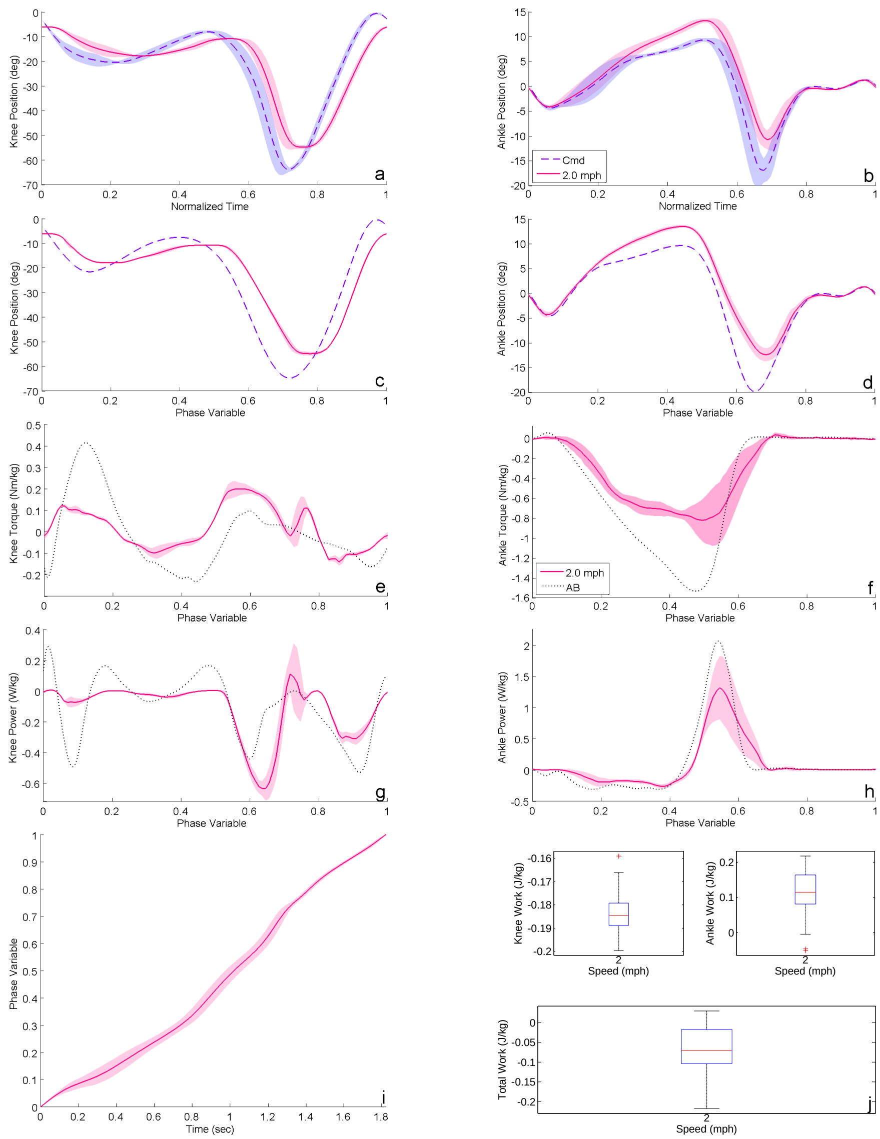

Figure 4.3. Powered prosthesis joint kinematics/kinetics for TF01 level-ground walking at 2.0 mph, averaged over 20 consecutive strides with ±1 standard deviation shown by shaded regions. The commanded (Cmd) and measured (2.0 mph) joint angles are shown over normalized time (a–b) and over the phase variable (c–d). The estimated joint torques (e–f) and powers (g–h) are normalized by subject mass and compared with averaged able-bodied data (AB) over the phase variable [116]. The knee torque is estimated with the measured motor current and the knee actuator model, and the ankle torque is estimated with the measured linear force and ankle kinematic model (Fig. 3.11). The phase variable over time (i) is strictly monotonic and nearly linear, where the most variance occurs during early and mid stance. Box plots of mechanical work per stride (j) show the median (red line), 25th percentile (bottom of box), 75th percentile (top of box), distribution bounds (black whiskers), and outliers (red plus markers). Ankle work is positive, knee work is negative, and total work is near zero as expected from able-bodied walking [116].

Fig. 4.3 displays the prosthesis kinematics and kinetics for TF01 averaged over 20 consecutive strides. The phase variable exhibits a nearly linear, monotonically increasing trajectory over time (Fig. 4.3i). The small variability about the mean can be attributed to normal within-stride variability between stance and swing, e.g., the phase variable exhibits a shallower slope during a longer stance period and a steeper slope during a shorter swing period. This behavior synchronized torque and power delivery with critical phases of the gait cycle (Fig. 4.3e–h) and resulted in consistent, smooth joint motion (Fig. 4.3a–d).

The commanded versus measured joint angles are shown over normalized time in Fig. 4.3a–b and over the phase variable in Fig. 4.3c–d. Because virtual constraints define the desired joint angles as functions of the phase variable, the commanded position only exhibits variance over normalized time. This temporal variability is associated with temporal variability in the phase variable based on the user's progression within the gait cycle (Fig. 4.3i), which resulted in slower or faster progression through the desired prosthetic trajectories. The measured joint kinematics exhibit small variance over both time and phase variable, demonstrating consistency over multiple consecutive strides. Some phase delay can be observed between the measured and commanded signals, which can be attributed to the reflected inertia of the actuators and the lower control gains employed for user comfort.

Fig. 4.3e–h display the joint torques and powers over the phase variable, which more accurately captures the within-stride progression of the user [113]. The knee torque and power was smaller than normal during stance ($s_h \in [0, 0.6]$) because of the non-backdrivable actuator design, which can support the weight of the amputee without much input from the motor. During swing period ($s_h \in (0.6, 1.0]$), the knee joint provides appropriate torque and power to help flex and then extend the knee. The ankle torque and power follow the curved shape of able-bodied data, particularly giving push-off torque and power during late stance. The measured values are lower than able-bodied averages due to the small control gains.

Fig. 4.3j provides box plots of the normalized mechanical work (J/kg) per stride for each joint (i.e., the time-integral of normalized joint power (W/kg) per stride). The ankle did positive work over the stride, behaving as an energy generator and giving the positive power needed for push-off [35]. The knee joint did negative work due to the negative power required for normative swing biomechanics [14]. The total work done by the prosthesis was close to zero, demonstrating a normative energy balance between the two joints [116].

4.2.2 Variable Speeds

Fig. 4.4 shows the averaged results for TF02 walking at different speeds with *matched* kinematics. The slope of the temporal phase variable trajectory increased with walking speed (Fig. 4.4g) due to the faster motion of the user's hip. This resulted in faster progression through the prosthesis joint patterns to match the shorter stride period. The prosthesis provided appropriate kinematics by enforcing the different virtual constraints for slow, normal, and fast walking (Fig. 4.4a–b), where the joint range of motion increased for the faster kinematics. The subject also performed a very fast trial (2.7 mph) using the fast kinematics, and some dynamic adaptation can be seen compared to the fast trial (2.5 mph). For example, the prosthesis exhibited greater ankle dorsiflexion during early stance ($s_h \sim 0.2$) in the very fast trial.

Torque and power delivery (Fig. 4.4c–f) during stance increased at faster speeds as observed in able-bodied data [116]. This resulted in more (positive) ankle work and total work at faster speeds (Fig. 4.4h), thus providing more assistance to the user. The subject spent more time in stance (i.e., a later stance-to-swing transition) while walking at the slow speed, resulting in some differences from the faster speeds. For example, the slow speed exhibited a longer period of ankle push-off torque and power (with less magnitude). At the slow speed, the knee had a large peak of negative power during swing flexion ($s_h \sim 0.65$), possibly to slow the knee while the user's hip rapidly accelerated to complete the shorter swing period.

Subject TF02 was able to walk at the same range of speeds using *fixed normal-speed* kinematics (Fig. 4.5) due to the temporal adaptation provided by the phase variable. In particular, the phase variable exhibited speed-appropriate slopes over time (Fig. 4.5g), which

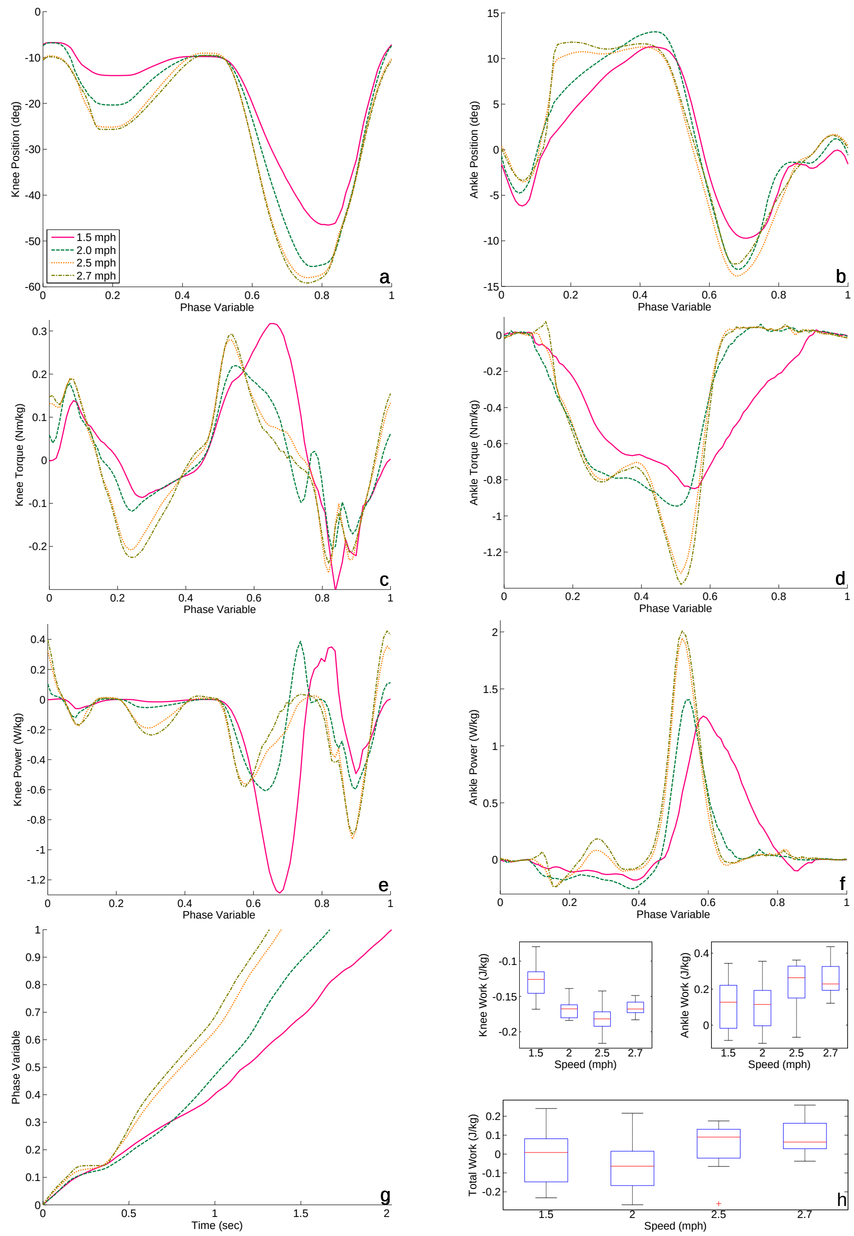

Figure 4.4. Powered prosthesis joint kinematics/kinetics for TF02 level-ground walking at multiple speeds with slow, normal, and fast kinematics, averaged over 15-20 consecutive strides. The measured joint angles over phase (a–b) demonstrate that faster speeds produce a larger range of motion. The estimated joint torques (c–d) and powers (e–f) are normalized by subject mass and plotted over phase, demonstrating more torque and power at faster speeds. The phase variable over time (g) is monotonic with a steeper slope (i.e., shorter time duration) for faster speeds. Box plots of mechanical work per stride (h) show the median (red line), 25th percentile (bottom of box), 75th percentile (top of box), distribution bounds (black whiskers), and outliers (red plus markers) for each speed condition. Ankle work and total work increase with walking speed as expected [116].

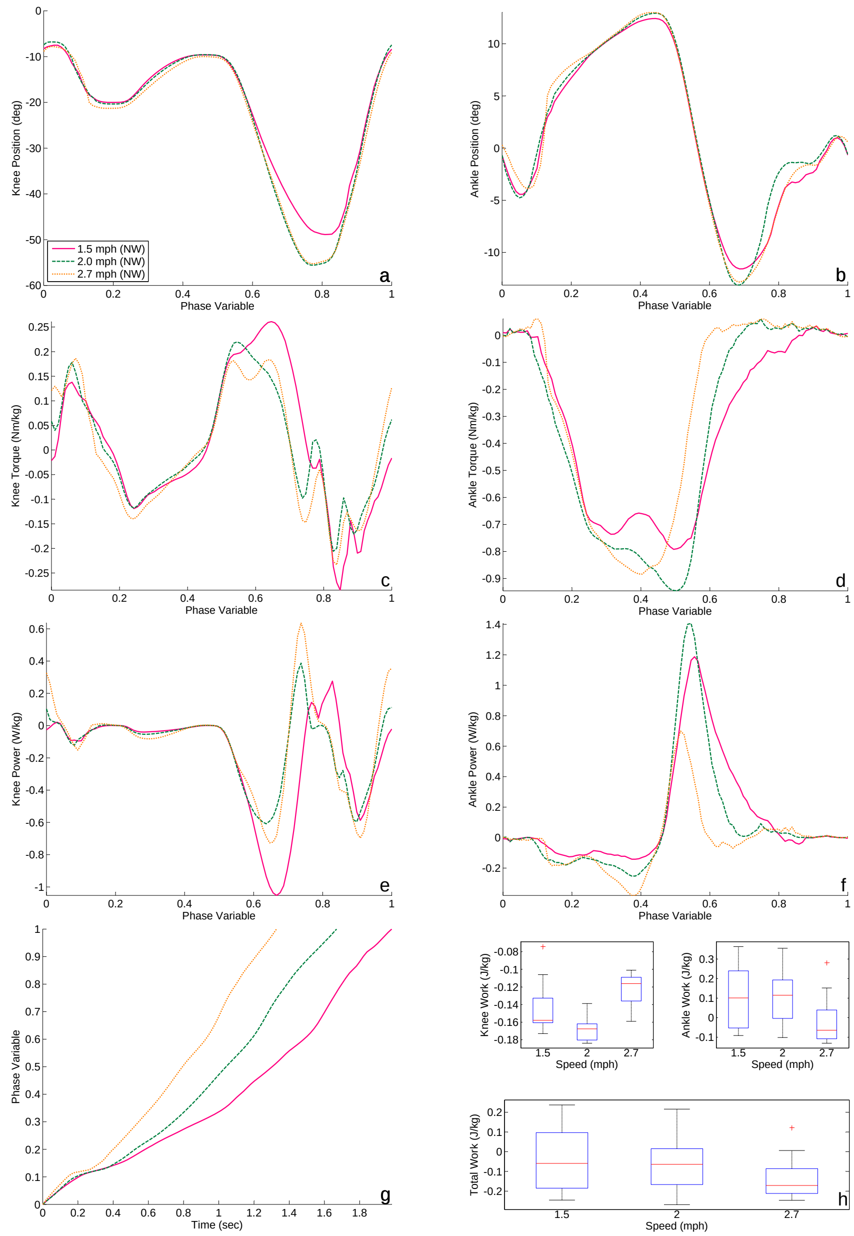

Figure 4.5. Powered prosthesis joint kinematics/kinetics for TF02 level-ground walking at multiple speeds with fixed normal-speed kinematics, averaged over 15-20 consecutive strides. The measured joint angles (a–b), normalized joint torques (c–d), and normalized joint powers (e–f) are more appropriate for slow and normal speeds than the fastest speed. The phase variable over time (g) adapts appropriately with all speeds, having a steeper slope (i.e., shorter time duration) for faster speeds. Box plots of mechanical work per stride (h) show the median (red line), 25th percentile (bottom of box), 75th percentile (top of box), distribution bounds (black whiskers), and outliers (red plus markers) for each speed condition. Ankle work and total work are appropriate for slow and normal walking but insufficient for the fastest speed [116].

appropriately slowed or accelerated the prosthetic leg's progression through its fixed joint trajectories. The different load conditions for slow and fast walking resulted in some dynamic adaptation in the prosthetic joint kinematics, especially at the slow speed (Fig. 4.5a–b). However, the fixed kinematics did not allow the joint kinetics (Fig. 4.5c–f) to adjust appropriately to changing speed. In particular, the ankle did not increase its torque and power output with walking speed as in the matched kinematics experiments (Fig. 4.4c–f). This resulted in a relatively flat trend in ankle work and total leg work as speed increased (Fig. 4.5h). These experiments demonstrate that fixed virtual constraints can provide adequate function at different walking speeds, but speed-matched virtual constraints promote more natural gait biomechanics, especially energetics.

4.2.3 Variable Inclines

Fig. 4.6 shows the averaged results for the different inclines (-2.5 deg to +9.0 deg) performed by TF02. Because the treadmill speed was consistent (2.0 mph) across inclines, the temporal phase variable trajectory remained consistent (Fig. 4.6g). The prosthesis provided appropriate kinematics by enforcing the different virtual constraints for each incline condition (Fig. 4.6a–b), where the knee joint (Fig. 4.6a) has more flexion from heel strike ($s_h \sim 0$) to heel rise ($s_h \sim 0.45$) at steeper inclines. The ankle joint (Fig. 4.6b) exhibited more dorsiflexion during stance to align the foot with the ground slope. Because of the consistent walking speed, swing knee flexion remained consistent across inclines as expected [20, 67].

Prosthetic joint kinetics at small ground slopes ($\pm$2.5 deg) are similar to level ground (Fig. 4.6c–f). Torque and power delivery during stance increased for inclines greater than +5.0 deg, providing a greater vertical force to the subject's center of mass. Ankle work tended to increase with ground slope (Fig. 4.6h), but the trend is not as obvious as the variable speed case (Fig. 4.4h). The total work done by the prosthesis was negative for positive slopes, possibly because the actuators were optimized for level-ground walking or

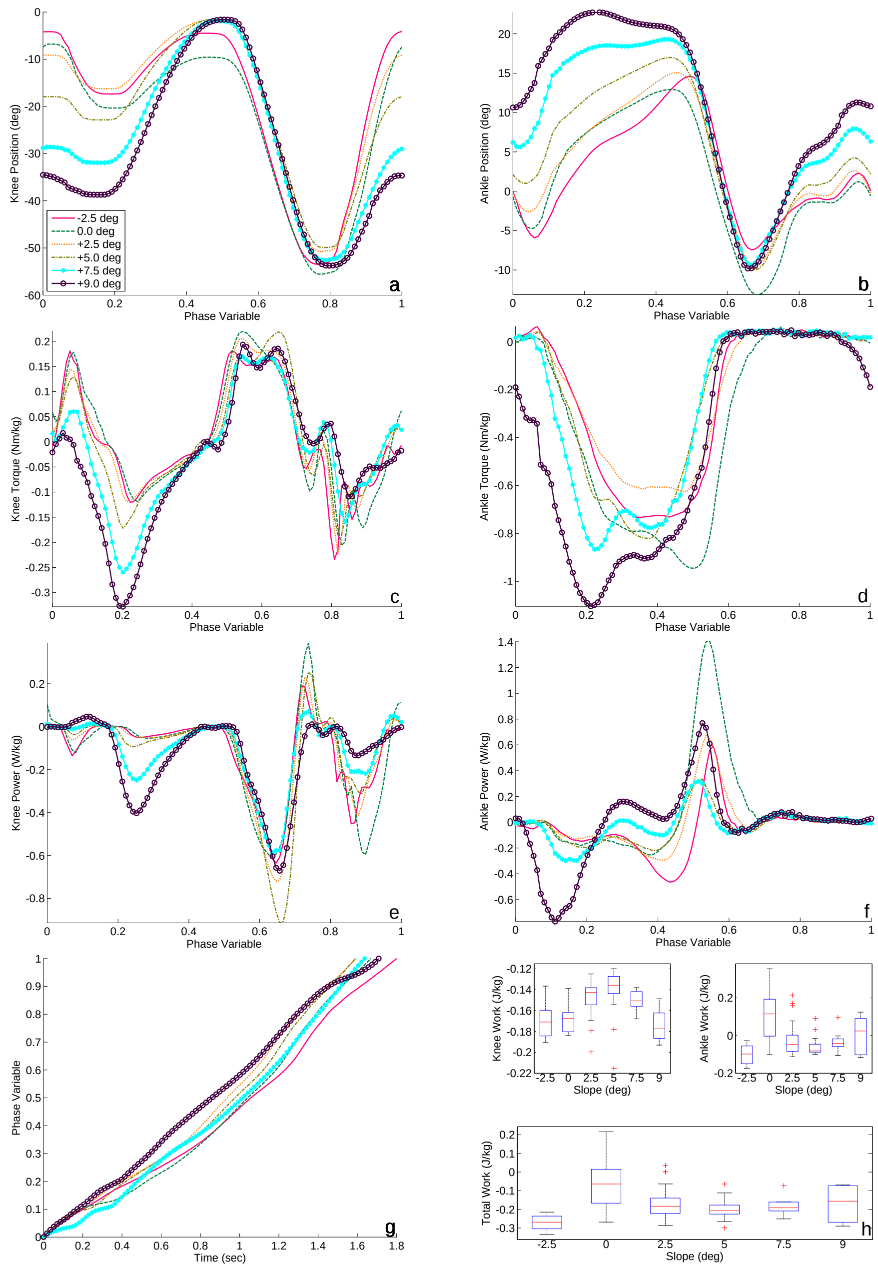

Figure 4.6. Powered prosthesis joint kinematics/kinetics for TF02 walking on multiple ground slopes at 2.0 mph with slope-specific kinematics, averaged over 10-20 consecutive strides. The measured joint angles over phase (a–b) exhibit more stance ankle dorsiflexion and stance knee flexion/extension for steeper inclines. The estimated joint torques (c–d) and powers (e–f) are normalized by subject mass and plotted over phase. The phase variable over time (g) has a consistent, linear trajectory across ground slopes (i.e., similar time durations). Box plots of mechanical work per stride (h) show the median (red line), 25th percentile (bottom of box), 75th percentile (top of box), distribution bounds (black whiskers), and outliers (red plus markers) for each slope condition.

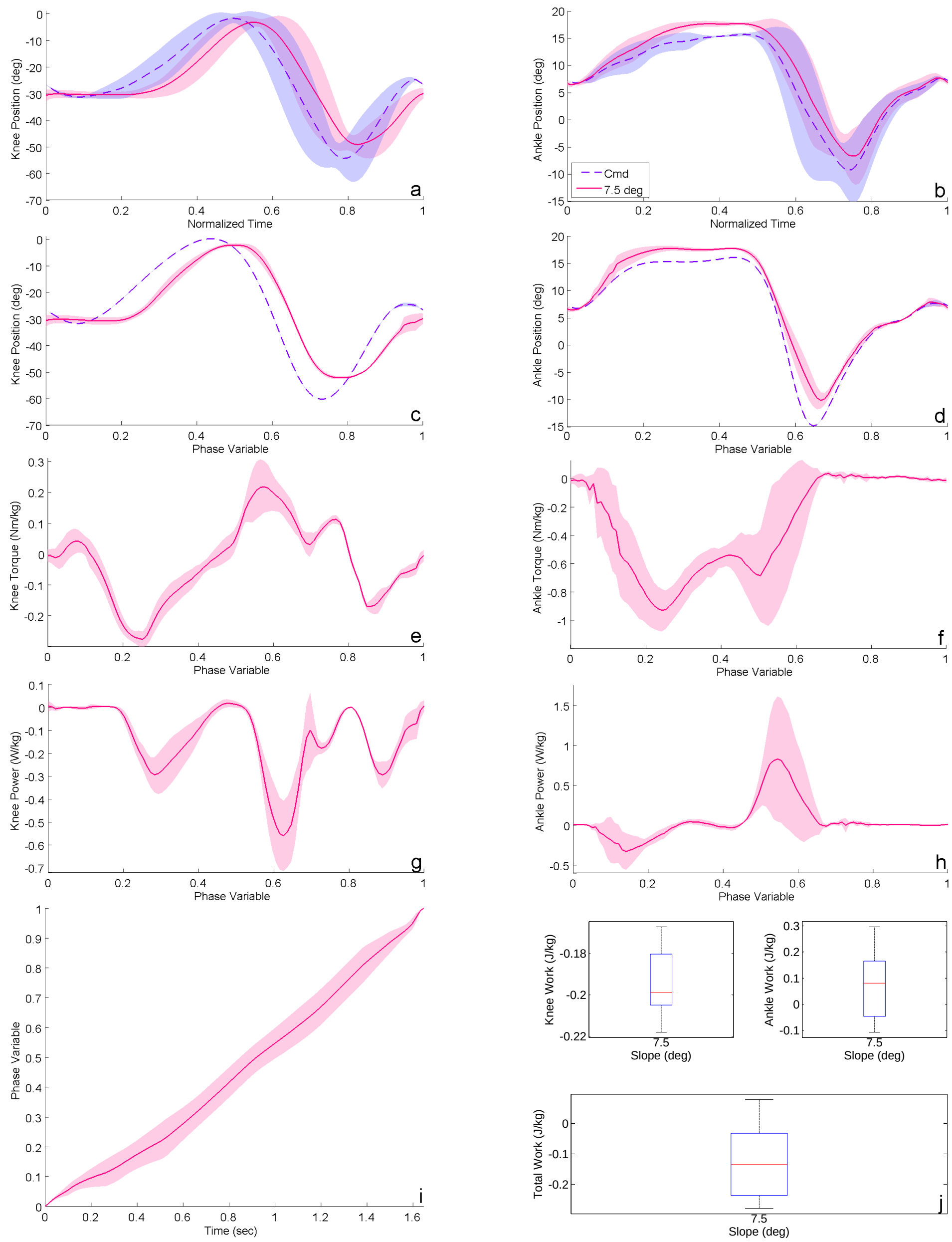

Figure 4.7. Powered prosthesis joint kinematics/kinetics for TF03 walking on 7.5 deg incline at 2.0 mph, averaged over 9 consecutive strides with ±1 standard deviation shown by shaded regions. The commanded (Cmd) and measured (7.5 deg) joint angles are shown over normalized time (a–b) and over the phase variable (c–d). The commanded signals have some variance at the end of the stride due to the use of a rate limiter as a safety feature. The estimated joint torques (e–f) and powers (g–h) are normalized by subject mass and shown over the phase variable. The phase variable over time (i) is strictly monotonic and nearly linear. Box plots of mechanical work per stride (j) show the median (red line), 25th percentile (bottom of box), 75th percentile (top of box), distribution bounds (black whiskers), and outliers (red plus markers).

because the kinematic data [20] encoded into the incline virtual constraints did not provide adequate power delivery (see Section 4.3.2).

For a closer look at another representative subject, Fig. 4.7 displays the mean and variance of prosthesis kinematics and kinetics for TF03 on a 7.5 deg incline. The averaged results largely match the 7.5 deg case of subject TF02 (Fig. 4.6), except the ankle provided more positive work for TF03 (Fig. 4.7j). The ankle push-off torque and power in Fig. 4.7 have similar amplitudes to the level-ground case of TF01 in Fig. 4.3. The inclined results in Fig. 4.7 exhibit slightly more variance than the level-ground case, possibly because inclined walking is a more intense activity.

4.3 Discussion

The goal of this work was to unify the gait cycle in prosthetic leg control using a continuous sense of phase. We showed that periodic virtual constraints can be defined for any speed/slope condition using the same phase variable, which enabled multiple amputee subjects to walk in those conditions using the same fixed control gains. The phase variable accommodated different walking speeds with fixed virtual constraints, but utilizing speed-specific virtual constraints improved leg energetics. These results motivate future implementation of continuous-phase controllers within task-level finite state machines, leveraging the rich literature on speed/slope detection [94, 84] and activity mode/intent recognition [83, 48, 111, 119].

4.3.1 Advantages of the Control Method

The primary clinical benefit of the continuous-phase control approach is a significant reduction in the dimension of the parameter space, which greatly reduces the configuration time for each amputee user. Current approaches that use different controllers for distinct phases of gait [109, 104, 106, 58, 6, 18, 108, 105, 59] have dozens of control gains and switching rules that require hours of tuning for each user [100]. The continuous control approach eliminates all switching conditions between gait phases and uses fixed PD gains, making it less sensitive to the ambulation mode and user than existing approaches. The phase variable provides the temporal synchronization needed to walk at variable speeds even with fixed virtual constraints, but speed-matched joint kinematics provide more appropriate adjustments in prosthetic leg work. It appears that normative able-bodied joint trajectories are an adequate starting point for different amputee subjects, though better user-specific performance could possibly be achieved with minimal tuning of the reference trajectories. The four PD gains could also be quickly modified by a clinician (see Chapter 5) or an automatic tuning method such as [47, 2, 56, 124, 57]. Hence, the continuous-phase control approach brings powered prosthetic legs closer to plug-and-play functionality across amputee patients.

These experiments also demonstrate that the human-inspired phase variable (the thigh phase angle) effectively synchronizes the powered prosthesis with the user's gait across speeds and inclines. Because hip motion reflects the natural variability between strides (e.g., some faster than others), prosthetic joint patterns appropriately accelerated or decelerated to match and complete each stride in sync with the user (Fig. 4.3). The phase variable also maintained the correct timing of critical events such as ankle push-off and swing knee flexion as conditions varied (Figs. 4.4 and 4.6), which is difficult to achieve with finite state machines. The periodic, unified virtual constraints produced very smooth, continuous joint motion within and across strides, which is also difficult to achieve when switching between finite states. One exception in the literature [60] has demonstrated similar ankle work and smoothness over variable speeds using a finite state machine based on quasi-stiffness during stance and minimum-jerk trajectories during swing.

Several qualitative observations were made during the experiments. The amputee subjects mentioned the prosthetic leg's synchronization with their intended motion. One subject mentioned relief of back pain while using the powered prosthesis compared to their passive take-home prosthesis, despite the fact that the powered leg was heavier. This feeling of relief was likely a consequence of the energy input from the powered joints, which minimized the need for hip compensations to initiate swing knee flexion and extension as required with a passive prosthetic leg [101, 96, 88]. The powered ankle push-off likely helped propel the leg into swing, so the user did not notice the extra weight of the leg while walking. The amputee subjects were given a post-experiment questionnaire to provide additional feedback, and they unanimously noted the benefits of the ankle push-off at terminal stance and the aiding knee moment during swing.

4.3.2 Limitations of the Study

The primary limitation of the presented control approach is the requirement of a well-defined thigh orbit (Fig. 3.13) to calculate the continuous phase variable (Eq. 3.7). This means that the control approach works best during rhythmic walking and not during start/stop transitions. A piecewise continuous version of this control approach was recently introduced in [114] to accommodate non-rhythmic, volitional motions such as starting, stopping, and walking backwards. The piecewise phase variable is determined directly from the thigh angle (without its integral or derivative), where a ground contact sensor determines whether the thigh angle is in the top or bottom half of its orbit. The piecewise controller can work in tandem with the continuous-phase controller to accommodate both non-rhythmic and rhythmic motions [114].

Hardware limitations were more prominent at the larger inclines and faster speeds because the actuators were optimized for the torque/speed requirements of level-ground walking. Because inclined walking demands large ankle torques, the ankle motor driver intermittently disabled itself (for milliseconds at a time) when exceeding its temperature safety threshold. This behavior caused larger variances in ankle torque/power than knee torque/power in Fig. 4.7. Because the large reflected inertia of the highly geared knee actuator was not compensated by closed-loop torque control, the knee joint was unable to swing freely. As a result, the knee joint had difficulty keeping up with the desired swing motion at the faster walking speeds, and the subject experienced stiffer interaction with the prosthesis. These limitations will be addressed in future designs with purely rotational actuators using high-torque pancake motors, low-ratio transmissions, and high amperage drivers as in [126]. Series elastic actuators [36, 93, 79] could also make the system more compliant and provide closed-loop torque control for enforcing the virtual constraints.

The experiments in Section 4.2 demonstrate that leg performance also depends on the reference trajectories encoded into the virtual constraints. A different able-bodied dataset was used to define the level-ground, variable-speed walking trajectories [116] than the variable-incline, normal-speed walking trajectories [20], which might explain why the work done by the prosthesis was not as favorable over inclines (Fig. 4.6h) as it was over speeds (Fig. 4.4h). Ankle work and total work were substantially higher for the level-ground condition (using data from [116]) than the incline conditions (using data from [20]) in Fig. 4.6h, and it is unlikely that hardware limitations alone would be responsible for the drop in work observed at small slopes (± 2.5 deg) compared to level ground. A post-hoc analysis of the two datasets suggests that inclines affect the temporal offset between heel strike and the left-most point of the thigh orbit, which defines 0% gait for the phase variable (Fig. 3.13). Hence, the phase variable may need to be shifted relative to the incline in order to achieve optimal power delivery, which is left to future work.

Because activity recognition was outside the scope of this study, the virtual constraints were manually changed to match the speed/incline condition. The discrete set of virtual constraints that was validated in this study could be incorporated into a higher-level task state machine, for which many classification techniques exist [83, 48, 111, 119]. In particular, a gait speed classifier can be implemented based on the cadence of the prosthesis (see Section 3.4.3), and the ground slope can be estimated by a foot-mounted IMU when the foot is flat on the ground (e.g., [94]).

CHAPTER 5

DEVELOPMENT AND CASE STUDY OF A CLINICAL INTERFACE

This chapter presents a solution to the challenges clinicians (e.g. prosthetists) encounter when interfacing and configuring a powered prosthesis. Typically powered prostheses use an impedance-based control scheme that contains several independent controllers each corresponding to periods along the gait cycle. This control strategy has numerous control parameters and switching rules to be tuned per subject, which generally are tuned by researchers or technicians and not by a certified clinician. Furthermore, some of these control parameters are not clinically intuitive or have no translation from a biomechanical perspective for clinicians to interpret and prescribe adjustments to the prosthesis. For instance, the impedance stiffness and damping tunable control gains contain arbitrary values that can be difficult to understand the direct impact of improving the prosthesis performance. We propose a clinical control interface that is intuitive for clinicians to tune a powered knee-ankle prosthesis using a virtual constraint controller, while reducing clinical time. The user interface assists clinicians to tune the controller based on their clinical expertise with regards to adjusting desired joint kinematic trajectories for the virtual constraints. Experiments with an amputee subject were performed for level ground walking with a certified clinician. The clinician tuned the controller with minimal time and improved the amputee's gait (i.e., gait symmetry, step length, etc.) compared to a baseline controller. The clinical control interface provides a bridge between advanced powered prostheses and the clinical environment, which can aid in having powered prostheses more readily available for amputees in their daily life.

5.1 Overview of a Clinician Control Interface

This section describes the methods in developing a Clinician Control Interface (CCI) and how it translates to the control of the prosthesis. The desired joint kinematic trajectories were created using Catmull-Rom splines from human walking data with an optimization routine to maximize goodness of fit. The final clinician-designed joint kinematics are then transformed into virtual constraints by method of DFT from Section 2.2, which is the control strategy of the powered prosthesis. The phase-based controller presented in Section 3.3.4 was used to perform the clinical control tuning experiments for overground walking. The algorithms described in this section were integrated in a graphical user interface using Mathworks MATLAB GUIDE app development tool [66].

5.1.1 Manipulation of Desired Joint Kinematics

The method for direct curvature manipulation prior to the design of the virtual constraints by DFT was using Catmull-Rom splines. This method comes from a cardinal spline that interpolates between control points to create a set of piecewise polynomials with matching tangent slopes at each piecewise boundary [11]. For a set of N control points, we combine $(N-1)$ piecewise polynomials to create a C^1 continuous, interpolation curve containing all N control points. This gives no discontinuities in the tangent direction and magnitude. The control points are defined by a set of N hand-picked (x, y) coordinates

$$C_P = \begin{bmatrix} p_{1,\rho} \\ \vdots \\ p_{N,\rho} \end{bmatrix}, \tag{5.1}$$

where $C_P \in \mathbb{R}^{N\text{x}2}$ and the subscript ρ refers to either x or y coordinate. The x-coordinate indicates a position along the normalized gait cycle and y-coordinate refers to the joint angular position of either the knee or ankle.

For each piecewise polynomial, the Catmull-Rom spline requires a set of four control points from C_P as $[p_{k-1} p_k p_{k+1} p_{k+2}]^\top$, where $k = 1, \ldots, N-1$ and the subscript ρ is suppressed. The spline endpoints are repeated for cases where $k = 1$ ($p_0 := p_1$) and $k = N-1$

$(p_{N+1} := p_N)$, so the tangents for interval data set sharing endpoints are equal. The cardinal matrix M_k creates the basis polynomial functions with uniform parameter spacing gives

$$M_k = \begin{bmatrix} -\alpha & 2-\alpha & \alpha-2 & \alpha \\ 2\alpha & \alpha-3 & 3-2\alpha & -\alpha \\ -\alpha & 0 & \alpha & 0 \\ 0 & 1 & 0 & 0 \end{bmatrix} \begin{bmatrix} p_{k-1} \\ p_k \\ p_{k+1} \\ p_{k+2} \end{bmatrix}, \tag{5.2}$$

where $\alpha = (1-c)/2$ and c is the tension parameter on the interval [0,1] that controls the curve bend at the interpolated control points. The tension parameter c is set to zero for a uniform Catmull-Rom spline. Evaluating the k-th piecewise polynomial segment results in

$$P_k(t) = \begin{bmatrix} t^3 & t^2 & t & 1 \end{bmatrix} M_k \tag{5.3}$$

$$\frac{dP_k(t)}{dt} = \begin{bmatrix} 3t^2 & 2t & 1 & 0 \end{bmatrix} M_k, \tag{5.4}$$

where $t \in [0,1]$. We evaluate all piecewise sections for both x and y dimensions of $p_1, \ldots, p_N$, and obtain the analytical parametric derivative by computing

$$\frac{dP_{k,y}}{dP_{k,x}} = \frac{dP_{k,y}}{dt}\left(\frac{dP_{k,x}}{dt}\right)^{-1} \tag{5.5}$$

with the condition that $dP_{k,x}/dt > 0$.

Human gait is a periodic sequence. Thus, it is advantageous for the interpolating splines for the knee and ankle joint kinematics to be periodic with respect to a gait cycle, that is, to ensure matching curve behavior in the first and last piecewise polynomials $P_1(t)$ and $P_{N-1}(t)$, respectively. We enforce periodicity through removing the original endpoints and duplicating existing control points to match the y-coordinates of p_1 and p_N. As a result, p_1 and p_N have no effect on the final curve other than defining the final x-coordinate range.

First, to ensure the final periodic curve spans the original x-coordinate range, we calculate

$$x_{min} = p_{1,x}$$

$$x_{max} = p_{N,x}$$

$$\Delta x = x_{max} - x_{min},$$

and discard the original p_1 and p_N endpoints. Duplicating the remaining four endpoints (p_2, p_3, p_{N-2}, and p_{N-1}) transforms the control points matrix to

$$\hat{C_P} = [\hat{p}_{N-2}, \hat{p}_{N-1}, p_2, p_3, \ldots, p_{N-2}, p_{N-1}, \hat{p}_2, \hat{p}_3]^\top, \tag{5.6}$$

where $\hat{p}_k$ points are duplicates of the original p_k point. The points $\hat{p}_k$ are translated in the x-direction by Δx to lie outside the original x-coordinate range

$$\hat{p}_{N-2} = p_{N-2} + [-\Delta x \;\; y_0]$$

$$\hat{p}_{N-1} = p_{N-1} + [-\Delta x \;\; y_0]$$

$$\hat{p}_2 = p_2 + [\Delta x \;\; y_0]$$

$$\hat{p}_3 = p_3 + [\Delta x \;\; y_0],$$

where $y_0 = 0$ to leave the y-coordinate unmodified. The curve generated by $\hat{C_P}$ spans from $\hat{p}_{N-1,x}$ to $\hat{p}_{2,x}$, so we truncate the regions outside $x_{min} \leq P_{1,x}(t)$ and $P_{N-1,x}(t) \leq x_{max}$. The final curve represents one period of a periodic C^1 continuous trajectory with identical values and tangent slopes at both endpoints.

5.1.2 Initialization of Interface Joint Kinematics

During initial startup of CCI tool, an optimization routine is computed for fitting a cardinal spline to an existing human joint kinematic dataset in [116]. This optimizer computes the limited number of control point coordinates (x, y) to create the piecewise cardinal spline, while minimizing the curve fitting error from the dataset. The fitted spline curve is defined as the default (Baseline) knee and ankle joint kinematics that clinicians begin manipulating using the interface tool. Since the cardinal spline curve intersects all control points, our curve-fitting approach chooses N control points from the input dataset $D \in \mathbb{R}^{L\text{x}2}$ consisting of L data points. We maximize the spline curve's goodness of fit R^2 value against the original dataset using an iterative approach in Algorithm 2. Throughout the algorithm, R^2 and $\hat{R}^2$ are goodness of fit measures calculated from the cardinal spline curve defined by the output C_P and current evaluated $\hat{C_P}$, respectively, and p_j refers to the current control point being operated on.

The while loop in line 2 adds new control points from the dataset D until R^2 reaches a sufficiently high threshold, κ. Line 3 selects the point of largest y-coordinate error in the dataset with respect to the evaluated spline curve (eval(C_P)), and line 4 appends the chosen point to C_P. Next, the algorithm prunes non-essential control points (line 9) after verifying the maximum $\hat{R}^2$ value calculated in line 7 exceeds $\hat{\kappa}$. Finally, we move each control point (line 18) within its respective piecewise section to the optimal position to maximize R^2. The final control points matrix C_P defines the optimized fit for the input dataset D. After the optimization routine is completed, the clinician can begin manipulating the curve based on their prescribed joint kinematics for a particular subject. Once the clinician completes their tuned trajectories, the curve dataset from the piecewise spline is used to parameterize a single parameterized function using method of DFT (see Section 2.2) against an ideal monotonic phase variable for the virtual constraint design of prosthetic joint control.

5.1.3 Features for Virtual Constraint Manipulation

The CCI leverages the Catmull-Rom spline to modify joint angle trajectories by adjusting the location of control points through various methods that affects the prosthesis virtual constraint design. Fig. 5.1 displays the interface that was created using Mathworks MATLAB GUIDE as the interactive tool for app development [66].

There are quick tuning buttons that allow the clinician to simultaneously move four control points to adjust the amplitude and location of key transition regions along the gait

Algorithm 2 : Optimization Routine using goodness of fit R^2

Input: Dataset $D = \{D_i\} \in \mathbb{R}^{Lx2}, i = 1, \ldots, L$
Output: $C_P \subset D$

Initialize $C_P = [D_1, D_{\lfloor L/4 \rfloor}, D_{\lfloor L/2 \rfloor}, D_{\lceil 3L/4 \rceil}, D_L]^\top$;
while $R^2 < \kappa$ **do**
  $i = \underset{i \in \{1,\ldots,L\}}{\arg\max} \ (|\mathrm{eval}(C_P)_{i,y} - D_{i,y}|)$;
  $C_P = [p_1, \ldots, D_i, \ldots, p_N]^\top$;
end while
while length$(C_P) > 4$ **do**
  $j = \underset{j \in \{2,\ldots,N-1\}}{\arg\max} \ (\hat{R}^2 \mid \hat{C_P} = C_P - \{p_j\})$;
  if $\hat{R}^2 > \hat{\kappa}$ **then**
    $C_P = C_P - \{p_j\}$;
  else
    break;
  end if
end while
for $j = \{2, \ldots, N-1\}$ **do**
  $\xi = \{i \mid D_i = p_{j-1}\}$;
  $\nu = \{i \mid D_i = p_{j+1}\}$;
  $g = \underset{g \in \{\xi+1,\ldots,\nu-1\}}{\arg\max} \ (\hat{R}^2 \mid \hat{p}_j = D_g)$;
  $p_j = D_g$;
end for

cycle: ankle push-off during terminal stance (45%-60%), and knee flexion during swing (50%-65%). Left and right arrow buttons shift the curve along x-axis, and plus and minus buttons increase and decrease the angular amplitude along the y-axis (see Fig. 5.5).

Under the *View* menu bar is the option to show advanced features to add and delete control points to the curve. Manually adding and deleting control points gives users more control over the placement of the piecewise polynomials. While this gives users complete control, it will override results of the optimization scheme described in Algorithm 2. Inserting a new control point requires adding a new point p_j to the control points matrix

$$C_P = [p_1, \ldots, p_{j-1}, p_j, p_{j+1}, \ldots, p_N]^\top,$$

where $p_{j-1,x} < p_{j,x} < p_{j+1,x}$. Likewise, deleting a control point consists of removing the point p_j from the control points matrix

$$C_P = [p_1, \ldots, p_{j-1}, p_{j+1}, \ldots, p_N]^\top.$$

Clicking and dragging any control point displays the modified curve in real-time for visual inspection of the result. Having the capability to view the joint angular position and velocity plots, a novice user can gain insight into the full effect of the kinematic modifications. Moving a control point p_j to a new (x, y) location $\tilde{p}_j$ replaces the corresponding entry in the control points matrix

$$C_P = [p_1, \ldots, p_{j-1}, \tilde{p}_j, p_{j+1}, \ldots, p_N]^\top \tag{5.7}$$

with the constraint that x-coordinate monotonicity $p_{j-1,x} < \tilde{p}_{j,x} < p_{j+1,x}$ still holds. For finer adjustments, control point (x, y) coordinates $\tilde{p}_{j,x}$ and $\tilde{p}_{j,y}$ can be specified through a manual numeric entry window option as well.

A neighboring points feature intuitively converts mouse drag operations into smooth adjustments across multiple control points. The feature applies part of the user-specified change $(\tilde{p}_j - p_j)$ to the immediate surrounding control points p_{j-1} and p_{j+1} based on the relative spacing of $p_{j-2}, \ldots, p_{j+2}$, given by the translation scaling coefficients

$$\gamma_1 = \frac{\|p_{j-1} - p_j\|}{\|p_{j-1} - p_{j-2}\| + \|p_{j-1} - p_j\|}$$
$$\gamma_2 = \frac{\|p_{j+1} - p_j\|}{\|p_{j+1} - p_{j+2}\| + \|p_{j+1} - p_j\|},$$

which apply the $\tilde{p}_j$ translation vector to the modified neighbor points

$$\tilde{p}_{j-1} = p_{j-1} + \gamma_1(\tilde{p}_j - p_j)$$
$$\tilde{p}_{j+1} = p_{j+1} + \gamma_2(\tilde{p}_j - p_j).$$

Finally, the modified control points are applied to the control points matrix as in Eq. 5.7:

$$C_P = [p_1, \ldots, p_{j-2}, \tilde{p}_{j-1}, \tilde{p}_j, \tilde{p}_{j+1}, p_{j+2}, \ldots, p_N]^\top.$$

To further aid clinicians in using this interface, a feature displays gait period reference markers within commonly known periods of gait (e.g., Loading Response, Mid-stance, Pre-Swing, Mid-Swing, and Terminal Swing). When enabled, the interface displays both the gait period name and highlighted region associated with the gait period hovered by the mouse.

Additionally, the CCI has the ability to compare the current trajectory design to previous designs with a comparison toolbar, listing previous amputee subject trajectory design files. For instance, a clinician can review a subject's current design from a past clinical session to determine if additional kinematic changes are needed for the subject to improve their gait. Selecting a previous design file displays the position and velocity curves alongside the current design. This comparison feature can help clinicians track changes over time for individual subjects, a vital feature for clinical applications.

5.1.4 Safety Considerations

While allowing the clinician freedom to adjust any control point on the curve, the clinician interface enforces pre-defined safety constraints. When a safety constraint is flagged while adjusting the curve, the interface posts a warning message and highlights the offending curve section in red. This then limits the adjustments the user can perform when manipulating the curve. Such safety constraints include the following items:

- Range of motion limits for the joint angular positions between two extremes.
- Velocity maximum setpoint limits for the magnitude of the joint angular velocities obtained in Eq. 5.5.
- Enforce the x-axis monotonicity requirement for Eq. 5.5 to ensure the joint angular velocities never approach a singularity.

This allows the clinician to adjust the joint kinematics that are feasible for the prosthetic leg design to perform.

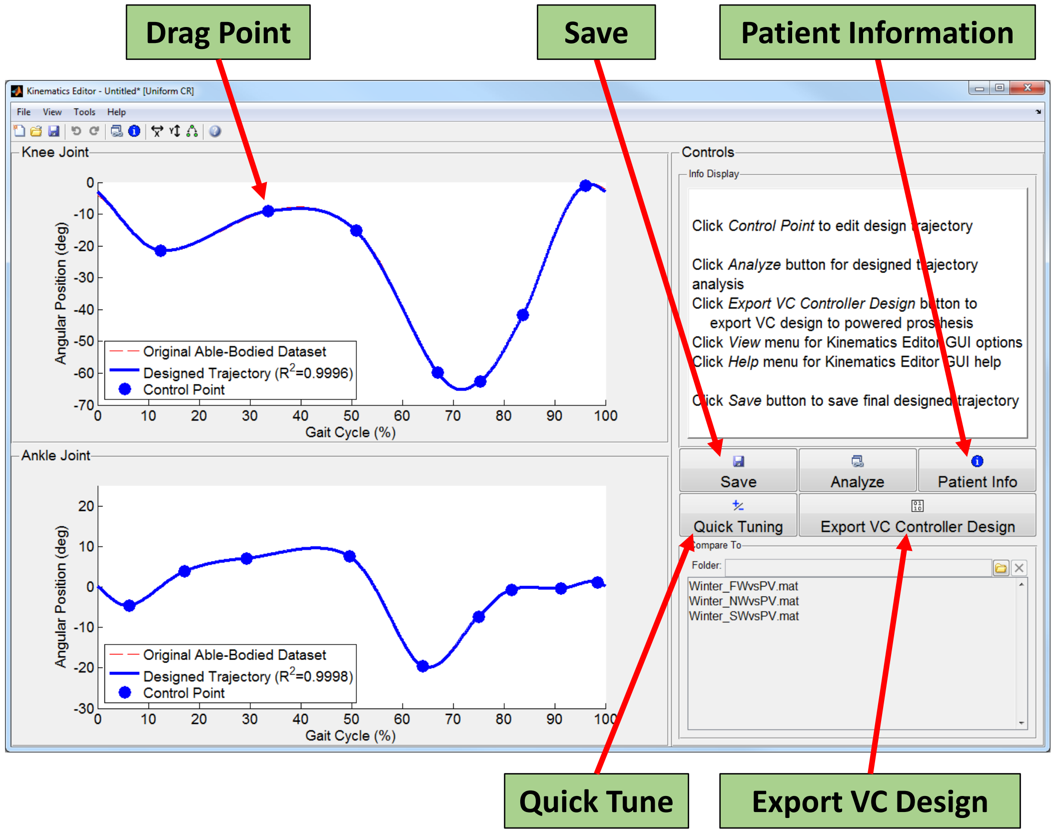

Figure 5.1. Clinician control interface with default knee (top) and ankle (bottom) angular position trajectories with respect to gait cycle, fitted to Catmull-Rom spline from Winter's dataset for normal walking [116]. Dragging the control points (blue dots) smoothly adjusts the joint trajectories. Commonly used features such as Save and Patient Information are easily accessible through large buttons.

5.2 Example of Clinical Tuning for a Powered Prosthesis

The main window of the CCI (Fig. 5.1) displays the knee and ankle angular position trajectories along the gait cycle with click-and-drag handles on the control points. Additionally, joint angular velocities with respect to gait cycle can also be shown using the Analyze button.

5.2.1 Initialization Setup

To begin the process of defining joint trajectories for a patient, the user must first open an existing patient file or create a new file. Creating a new file allows the user to enter

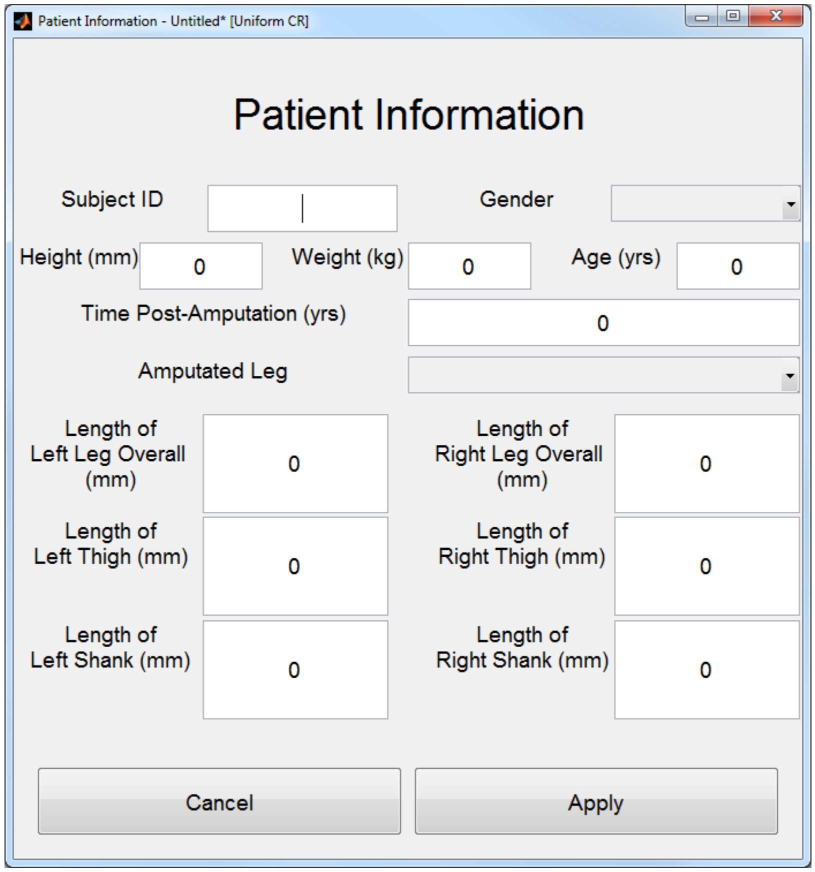

Figure 5.2. Patient information dialog displays the subject ID, gender, height, weight, age, time post-amputation, amputated leg, and leg measurements.

patient information such as subject ID, gender, age, and lower limb anatomical measurements (Fig. 5.2) for future retrieval. New files contain the Baseline joint kinematics for a given task as a starting point to tune the prosthesis for the patient. Opening an existing file displays the patient information and modified joint trajectories for that patient. All patient data is stored alongside the designed joint trajectories in a single MATLAB data file. Launching the help window (Fig. 5.3) guides the user step-by-step through common actions.

5.2.2 Joint Kinematic Adjustment

Fig. 5.4 outlines the kinematic adjustment procedure using the CCI. Once the patient file is initialized, the user begins interactively adjusting the kinematic trajectories by the methods

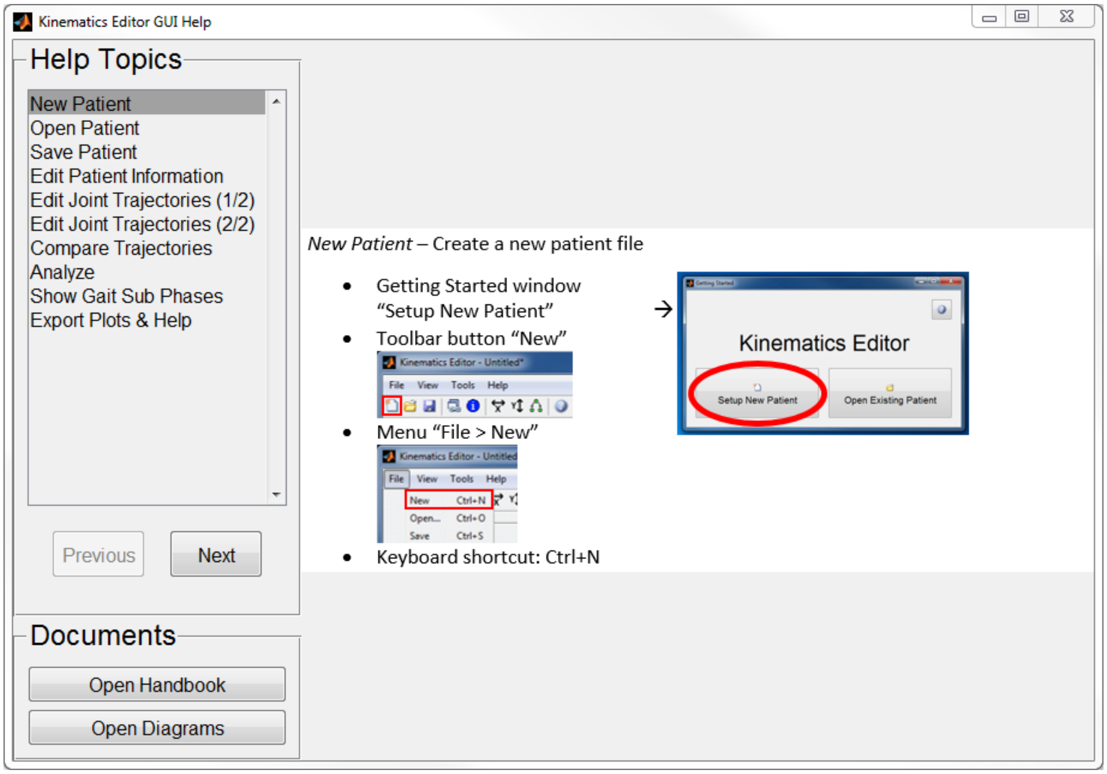

Figure 5.3. CCI Help window guides the user through common actions, such as editing trajectories and analyzing the kinematics.

in Section 5.1.3 to achieve the desired kinematics for the patient. When finished tuning, the user saves the modified trajectories and exports them to design trajectories using Eq. 2.6 over an ideal phase variable to implement virtual constraint control to the powered prosthesis. After observing the patient's gait with the new trajectories, the clinician may repeat the tuning process to further refine the performance of the prosthesis.

Case Example

Assume a patient's gait needed more push-off and to occur earlier in the gait cycle, then a clinician may press the ankle plus (+) and left (<) buttons in the quick tuning panel (Fig. 5.5). The resulting joint trajectories will have more push-off occurring earlier in the gait

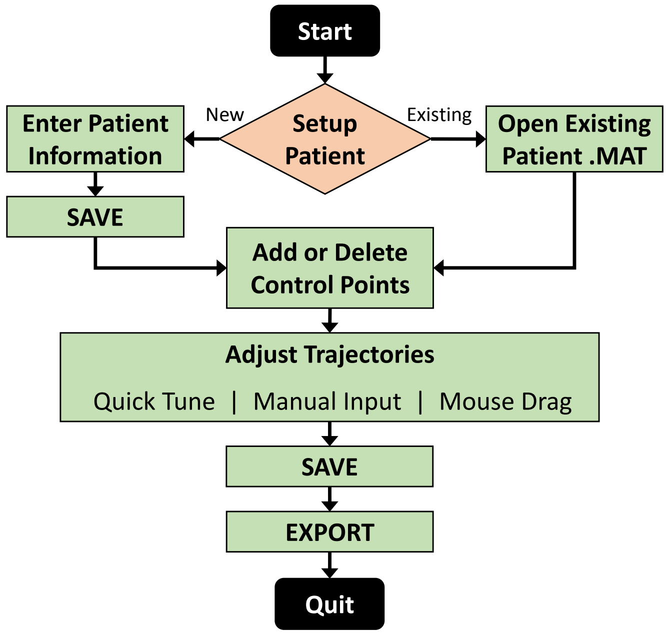

Figure 5.4. Flow diagram for the clinician graphical user interface. Setup begins with either opening an existing patient file or creating a new file with Patient Information. The user adds or deletes control points and adjusts the trajectories as desired. When finished tuning, the user saves the modified trajectories and exports the design for virtual constraint control to the powered prosthesis.

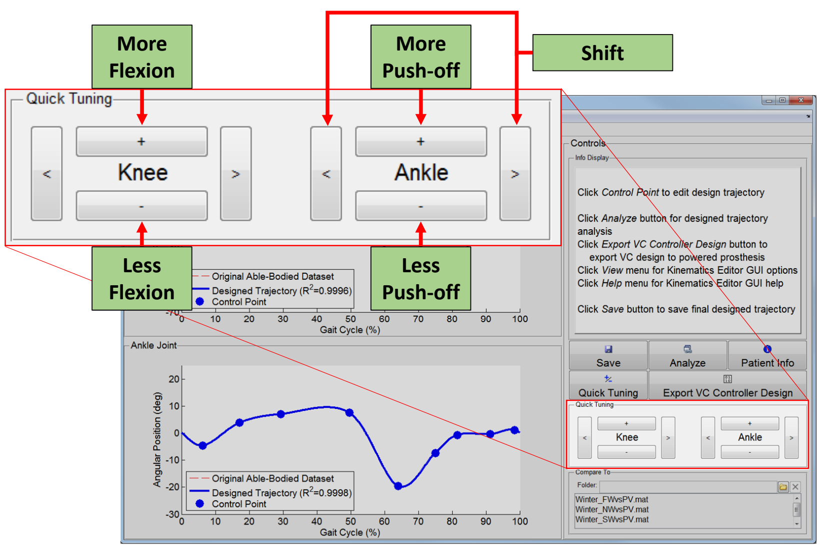

Figure 5.5. Quick tuning buttons allow for easily adjusting ankle push-off and knee flexion during swing. The plus (+) and minus (-) buttons increase and decrease the amplitude of the angular position, and the left (<) and right (>) buttons move the transition earlier and later in the gait cycle, both respectively.

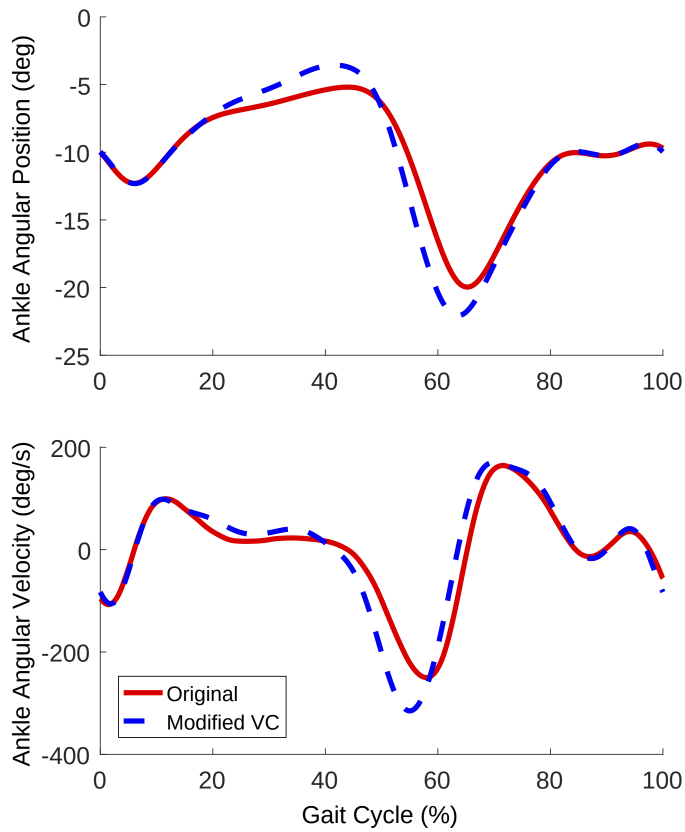

Figure 5.6. Case study of increasing ankle push-off and shifting earlier in the gait cycle. The modified ankle angular position (top blue dashed line) has more push-off range occurring earlier than the original trajectory (top red solid line). The modified ankle angular velocity (bottom blue dashed line) has a larger magnitude than the original angular velocity (bottom red solid line) as a result of the increased push-off amplitude.

cycle. Fig. 5.6 displays the ankle angular position and velocity before and after performing the quick tune.

All modifications to the joint trajectories are checked against safety constraints as defined in Section 5.1.4. If a user attempts to advance push-off earlier by dragging the control point too far to the left as shown in Fig. 5.7, then the CCI will highlight the offending section and alert the user that the modification exceeds the prosthesis safety limits for velocity. By automatically restricting all edits to the furthest extent allowed by the safety constraints, the CCI helps train users by demonstrating the range of allowed modifications in real-time.

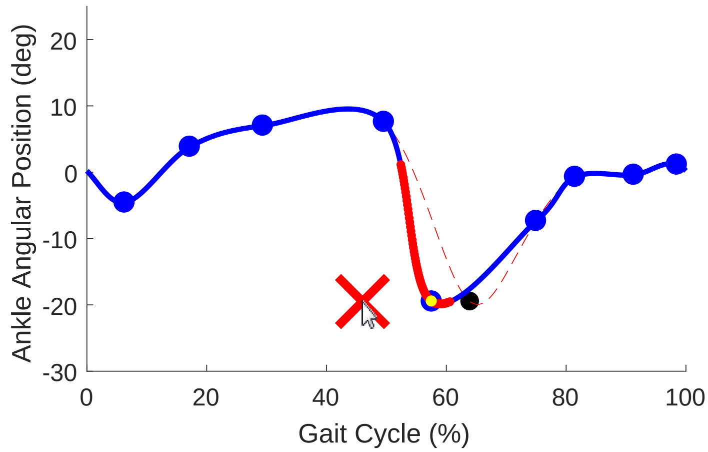

Figure 5.7. Sample user adjustment beyond safety limits. The user drags the cursor (pointer) to move the original control point (black circle) to a new location (red cross). Safety features restrict the modification to the furthest safe control point location (blue circle with yellow center).

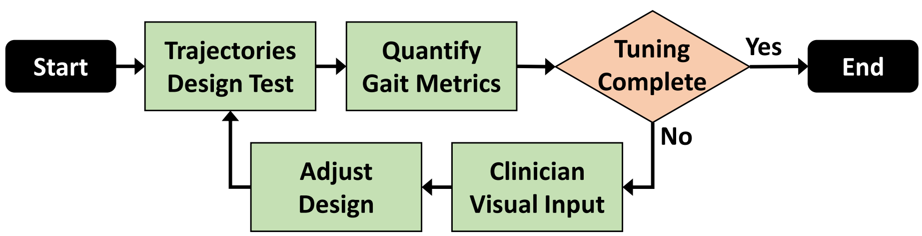

Figure 5.8. Block diagram of clinician input into the joint angle trajectories design process. Clinician visual feedback and other comparison metrics as described in Section 5.1.3 allow the tuning process to reach better performance for the patient.

5.2.3 Clinical Tuned Control Implementation

Once the joint trajectories are finalized, the user exports the curves to a virtual constraint representation as discussed in Section 2.2. The final virtual constraint coefficients are saved by pressing Export VC Design button (see Fig. 5.1), and then compiled to the real-time processor for testing and evaluation on the powered knee-ankle prosthesis. Fig. 5.8 shows the iterative process where clinicians may adjust the trajectories and repeat testing to meet the needs of the patient.

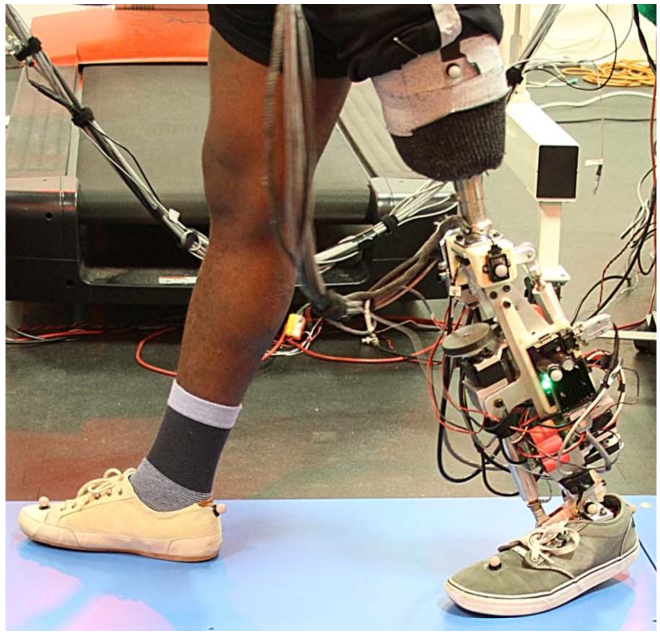

Figure 5.9. Photo of a transfemoral amputee subject wearing the powered knee-ankle prosthesis. Reflective markers placed on the amputee's lower limbs to collect kinematic data during walking trials from a motion capture system.

5.3 Clinical Tuning Experiment

The experiments replicated a clinical setting between a certified clinician and an above-knee amputee fitting a new prosthesis. The prosthesis controller scheme used for volitional overground walking is described in Section 3.3.4. The goal of the experiments were to have the clinician apply their professional expertise in tuning a powered knee-ankle prosthesis using the CCI tool to improve the amputee's gait. Results of the clinical tuning to adjust the prosthesis controller will show improvement in the amputee's gait from several gait outcome metrics.

5.3.1 Experimental Setup & Protocol

The experimental setup consisted of a 5.3 m long handrail walkway with a force plate located in the middle to collect ground reaction forces (GRF) at a sample rate of 500 Hz. A ten camera motion capture system (Vicon, Oxford, UK) utilizing Nexus Plug-in-Gait software was used to record kinematic parameters of the subject. Reflective markers were placed along key landmarks about the subject's lower limbs (see Fig. 5.9) to measure 3D spatial coordinates to create a 3D kinematic biped model. Anatomical measurements (e.g., leg length, hip width, etc.) were taken from the subject to aid in creating the 3D model. The subject was asked to bring or was provided comfortable clothes so that no markers would be occlude/obscure in being captured by the cameras.

The experimental protocol was approved by the Institutional Review Board at the University of Texas at Dallas. The transfemoral amputee subject had a height of 1.75 m, weight of 76.5 kg, post-amputation time of 11 yrs, and left side amputation. The subject and the clinician had no prior experience using a powered prosthesis. The clinician who participated in the experiment has been a practicing, licensed prosthetist for 14 years. To begin, the clinician attached and aligned the powered prosthesis to the subject's custom socket. The subject spent a period of time getting acclimated to the powered prosthesis by walking overground with handrails. The control strategy from Section 3.3.4 was incorporated using control law from Eq. 3.10 to enforce control at each of the joints. Only the forward walking control sequence was used as no backward walking was performed as part of this experiment (see Fig. 3.15). The control gains were tuned prior to this experiment with an able-bodied subject overground walking for normal walking speed. Note, for these experiments the load cells placed along the ball screw (see Section 3.2) for closed-loop torque control were not functional at both joints and too costly to replace. Thus, pure proportional and damping control terms were tuned (from Eq. 3.10 $\dot{y}_i$ was replaced with the measured angular velocity $\dot{q}_i$ for both knee and ankle).

The experiment entailed a subject performing forward walking handrail experiments using the powered prosthesis described in Section 3.1. A forward walking trial began at one end of the handrail walkway from rest to walking forward at the subject's comfortable walking speed until reaching the other end of the walkway to complete the trial. The subject began trials using a default (Baseline) controller with virtual constraint designed from normal walking joint kinematics in [116], while proceeding with the following steps.

Step 1) The subject walked the full length of the handrail for a forward walking trial twice while the clinician (e.g., prosthetist) observed the subject's gait to determine if adjustments to the prosthesis were required.

Step 2) If the clinician had recommendations to improve the gait of the subject, then the CCI was used to make the necessary adjustments (see Section 5.1.3).

Step 3) Once the clinician incorporated changes to the joint kinematic trajectory from the CCI tool for either knee or ankle, then those design trajectories were converted to virtual constraints using the method in Section 2.2.

Step 4) After the new clinician-designed virtual constraints were implemented and compiled in the prosthesis software, the subject repeated the forward walking while the clinician observed if the new prosthesis controller improved the subject's gait based on their clinical expertise.

The clinician was a novice user to the CCI and only given a brief introduction prior to its use. *Steps 1)* through *4)* were repeated until the clinician and the subject were in agreement that the clinician controller was stable and comfortable for the amputee to perform daily walking.

5.3.2 Experimental Results

The scope of this study was to emulate a clinical session with a certified clinician adjusting a prosthesis to a lower limb above-knee amputee. The clinician had the final decision when the prosthesis was tuned appropriately for the amputee. Thus, the number of trials was inherently limited for this particular experiment, consequently, statistical analysis is not impactful. The experimental results investigate gait outcome metrics, such as spatial-temporal parameters and gait symmetry. These calculations are evaluated for both the prosthesis and intact leg within each clinical trial while compared against the Baseline controller. The trials for each controller are concatenated to produce average and standard deviation of the results.

Clinician Virtual Constraint Design & Outcome

The clinician performed *Steps 1)* through *4)* from Section 5.3.1 with the amputee subject, creating two different clinician controllers. After observing the amputee walking with the Baseline controller, the clinician prescribed that the subject needed more ankle push-off. This involved using the CCI to increase ankle range of motion in the gait region of terminal stance to push-off. The clinician did not make adjustments to the knee. This first clinician controller design was labeled as Controller 1. The amputee repeated forward walking trials with Controller 1, while the clinician observed the amputee's gait. The clinician and amputee discussed together what functional changes needed to be achieved in improving the prosthesis performance outcome. The amputee provided feedback to the clinician after using Controller 1, that is, requesting additional tuning at the ankle for more push-off. Also, the clinician observed adjustment in gait phase was needed to improve timing when push-off occurred with regards to the amputee's hip motion from the phase variable.

A second clinician controller (Controller 2) was designed with more adjustment to ankle push-off and small change to knee swing. After the subject repeated forward walking trials with this new controller, the clinician from a visual inspection and the subject both agreed that the second controller was tuned appropriately. Fig. 5.10 displays the Baseline joint kinematics compared to the two clinician controllers from using the CCI tool to create the final virtual constraint designs to the prosthesis.

Fig. 5.11 presents the powered prosthesis results of the amputee using the Baseline controller and the final preferred design amputee controller in Controller 2. Observing Fig. 5.10, it can be seen that the adjustment in more ankle push-off for Controller 2 was realized in the ankle angular position (see Fig. 5.11). This impacted Controller 2 knee angular measurements by producing a smaller magnitude during swing due to a large increase in ankle push-off that assisted in an earlier pre-swing compared to Baseline. Furthermore, this also affected the thigh motion of the amputee during walking with increased thigh angle magnitude when using Controller 2. Fig. 5.12 shows the piecewise phase variable measurement derived from Section 3.3.4 over the consecutive strides achieved on the handrail walkway. The following sections will overview the experimental results from a gait analysis point of view.

Spatial-Temporal Parameters

Spatial-temporal parameters are gait analysis metrics to assess the performance of a human's locomotion [116, 77]. Spatial evaluates distance parameters (e.g., step length) and temporal takes into account time parameters (e.g., stance time). The clinician controllers brought convergence of these spatial-temporal parameters between the prosthesis and intact leg, such as step length, stance time, swing time, and stance percentage. These metrics show confidence of the subject with the prosthesis as well as improvements in gait symmetry. Table 5.1 displays the spatial-temporal parameter averages for each controller and their standard deviation in parentheses. Controller 1 showed a 4.0% increase difference between the prosthetic and intact leg in step length compared to the Baseline difference, while Controller 2 had a 75% decrease resulting in an average difference of 2.6 mm (compared to Baseline's 40 mm difference). Improvements in symmetry are very apparent; the difference in stance time, a good marker of uneven gait, decreased by 15% with the first controller and 44% with the second. Controller 1 showed a 30% decrease in swing time compared from the

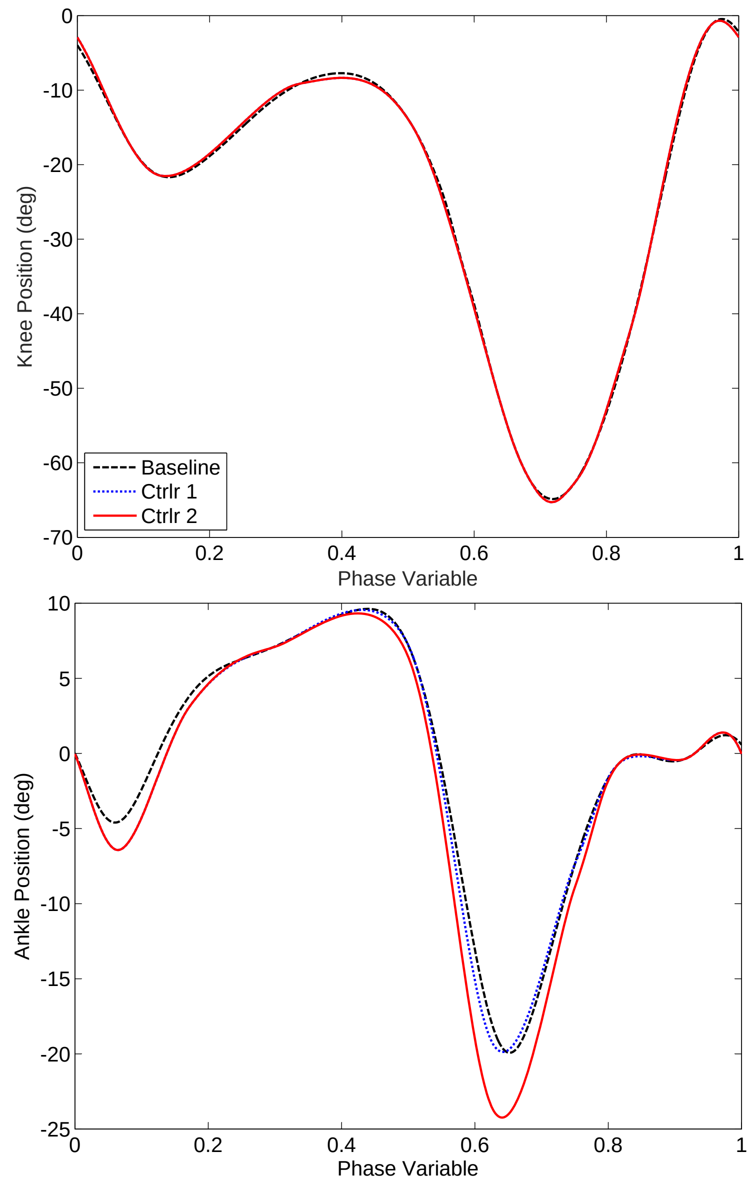

Figure 5.10. Clinician joint kinematic design for Controller 1 (Ctrlr 1) in blue dotted line and Controller 2 (Ctrlr 2) in red solid line versus the Baseline controller in black dashed line over phase variable. The knee (top) trajectories had very minor adjustment with the Baseline and Controller 1 remained the same (on top of each other), and Controller 2 was slightly shifted in phase to the left for earlier swing. The ankle (bottom) trajectories each had some variance from Baseline controller with increase in ankle push-off between $s_h = 0.5$ to 0.78, where Controller 2 had the largest push-off difference and earlier start of push-off occurring at $s_h = 0.42$. Both controllers have an increase in plantarflexion to have the foot give higher loading response ($s_h = 0.075$) after heel strike ($s_h = 0.0$). All these trajectories were exported from the CCI tool into the prosthesis virtual constraint controller for experimentation.

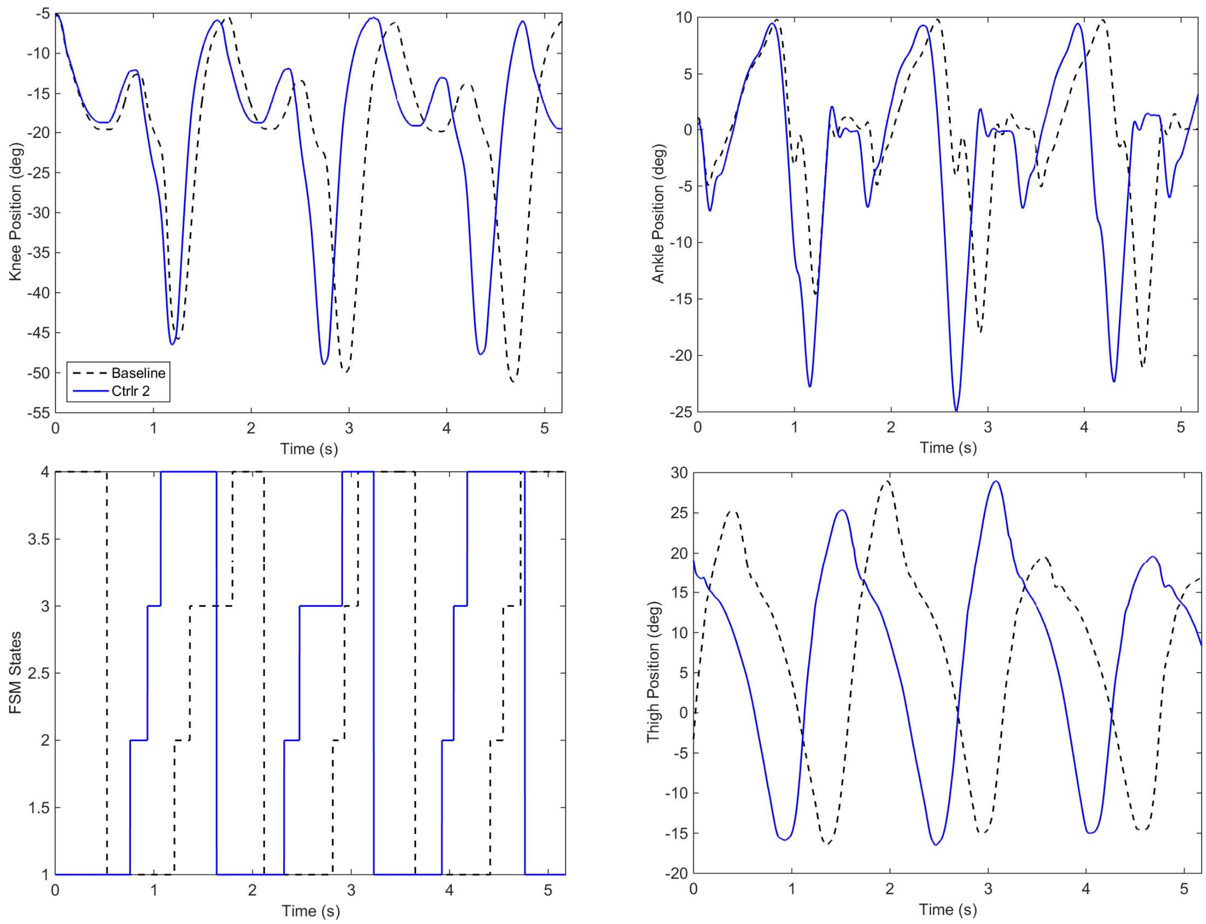

Figure 5.11. Powered prosthesis measured signals over consecutive strides for a forward walking trial when the amputee is using the Baseline controller in black dashed line and the clinician Controller 2 (Ctrlr 2) in blue solid line. Baseline and Controller 2 were separate test trials, so the results are compared by having their time sequence aligned with respect to their first phase variable measurement (see Fig. 5.12). The knee angular position (top left) for both controllers have similar responses with the exception of a phase shift, likely from the increase ankle push-off (top right) for Controller 2. FSM states (bottom left) shows that each state was achieved in sequence with some states occurring in longer duration. Thigh position (bottom right) gives larger magnitude when ankle push-off is increased using Controller 2 (t = 2.25 to 3.1 s).

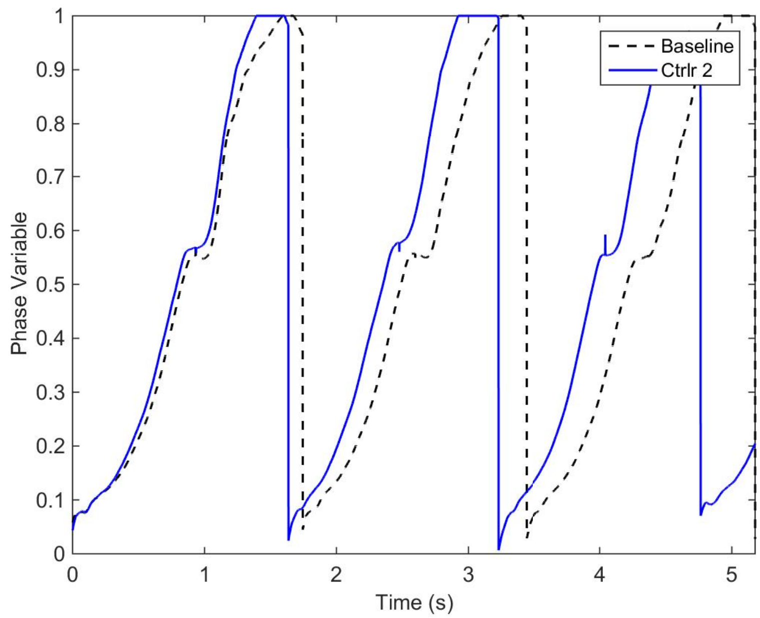

Figure 5.12. The phase variable measurement over time shows Controller 2 (Ctrlr 2) compared to Baseline occurring faster with respect to time as the amputee is getting aided assistance from increase in ankle push-off along gait.

Baseline and Controller 2 presented a 58% decrease. The change in stance and swing time have repercussions in stance percentage, the percent of the gait cycle that the ipsilateral foot is on the ground during the gait cycle, causing the percentages to gradually converge closer to the accepted textbook value of 60% for normal walking [9].

Table 5.1. Spatial-Temporal Parameter Results

	Stance Time [s]		Swing Time [s]		Step Length [m]		Stance Percentage [%]	
	P	I	P	I	P	I	P	I
Baseline	0.82 (0.08)	1.11 (0.06)	0.72 (0.01)	0.40 (0.00)	0.51 (0.01)	0.47 (0.01)	54.9 (1.7)	70.9 (1.6)
Controller 1	0.91 (0.12)	1.17 (0.11)	0.65 (0.06)	0.41 (0.02)	0.48 (0.03)	0.45 (0.10)	58.2 (4.9)	73.7 (2.6)
Controller 2	0.88 (0.05)	1.07 (0.19)	0.65 (0.07)	0.47 (0.06)	0.54 (0.04)	0.54 (0.03)	57.6 (3.5)	69.2 (3.4)

Ground Reaction Forces

Table 5.2 shows the peak ground reaction forces (GRF) measured in terms of Body Weight (BW) units (force divided by subject's weight) by a force plate located in the middle of the

Table 5.2. Analysis of Ground Reaction Forces

	Peak GRF [BW]		Braking [BW]		Propulsive [BW]	
	P	I	P	I	P	I
Baseline	–	1.23	–	0.06	–	0.085
Controller 1	1.02	1.13	0.064	–	–	–
Controller 2	1.08	1.21	0.067	0.073	0.057	0.098

walkway. It was imperative that the subject was not informed of the force plate location, so to not alter their gait when performing walking trials. Thus, any table cell with '–' indicates an incomplete or bridged step over the force plate and the reading was invalid for that test. Table 5.2 gives a lower peak GRF for the Baseline compared to Controller 1. Both the intact and prosthetic sides with this controller were close to reported values for transfemoral amputees (1.02 BW prosthetic, 1.13 BW intact) [97], while Controller 2 showed higher peak values (1.08 BW prosthetic, 1.21 BW intact). These results are single step outcomes and more trial passes would of reduced the number of invalid force plate readings to give clinical significance in the results. Fig. 5.13 shows GRF for both the prosthesis and intact leg when using Controller 2.

To continue, Table 5.2 showed Controller 2 having comparable braking and propulsive forces, an indicator of gait with no acceleration, on the prosthetic leg [128]. Along the axis of motion, braking pushes forward as the foot stops and propulsion pushes backward 'propelling' itself into the swing period [78]. Similarities are seen between Baseline and the clinical controller trials showing no significant difference between the trials for braking and propulsive forces. Furthermore, Controller 2 produced higher forces on the intact leg: 0.01 BW higher for braking and 0.025 BW higher for propulsive forces, which is consistent with expected trends [97].

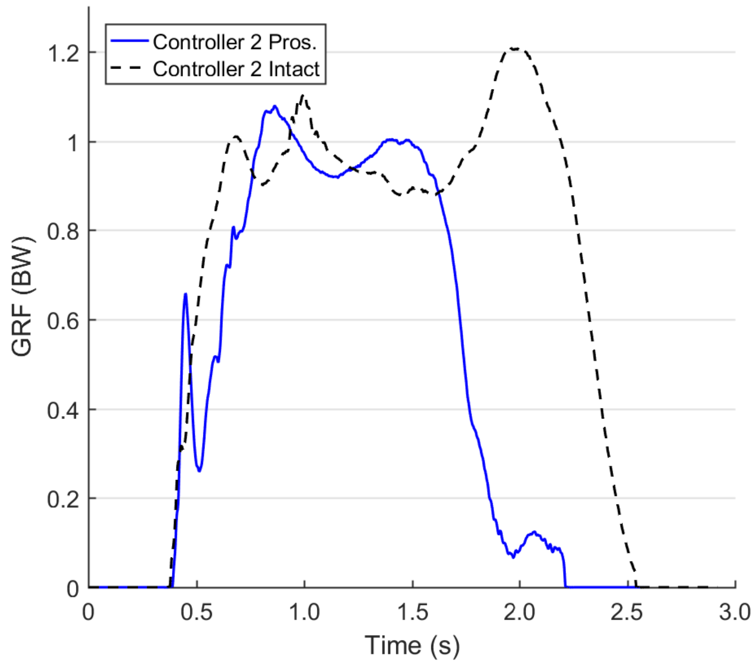

Figure 5.13. This figure shows vertical normalized GRF for Controller 2 with respect to units of Body Weight (BW). The blue solid line refers to the prosthetic side (Controller 2 Pros.) and in black dashed line is the intact side (Controller 2 Intact). The initial sharp peak on the prosthetic side is due to impact force before loading and the relative peak on the intact side at $t = 1.0$ s corresponds with the subject's vault. The difference in duration is a good representation of the difference in stance time between the prosthetic and intact limbs.

Gait Pathology Results

Powered knee-ankle prostheses mitigate compensatory mechanisms by actively providing energy during toe-off and lifting the toe during swing period. This increases clearance of the affected limb; associated values are reported in Table 5.3. Vaulting, excessive plantarflexion during stance, is often seen in combination with other compensatory gait methods such as increased range of motion of the hip and pelvis frontal plane for aid in toe clearance of the prosthesis. It is most commonly quantified by measuring peak ankle plantarflexion power during single support [17] and can be seen in Fig. 5.13, but the data did not have consistent force data so that metric cannot be used. This work presents an alternate approach to kinematic quantification. This approach measures peak plantarflexion by tracking the foot

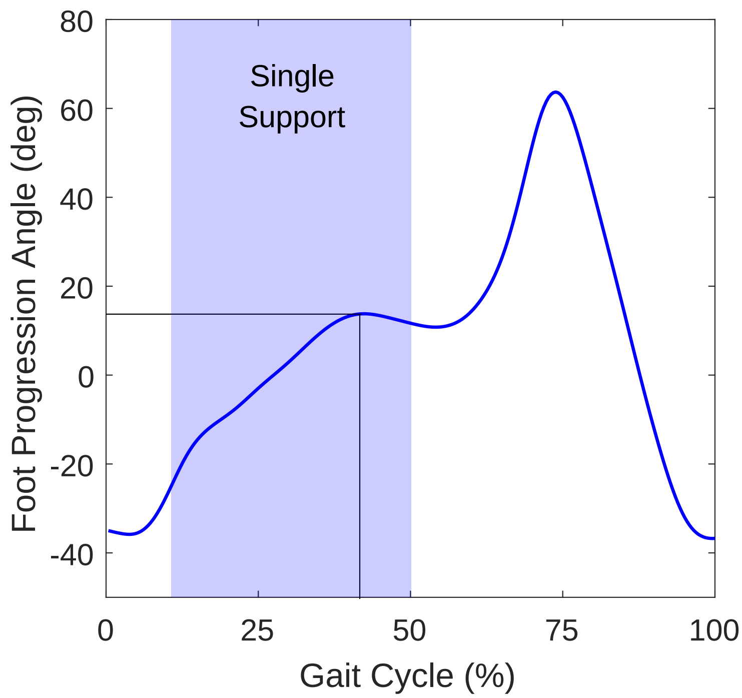

Figure 5.14. Intact leg foot progression angle in the sagittal plane over a gait cycle that identifies the peak angle of plantarflexion (thin black lines) in the single support period (shaded region) using the powered leg to illustrate the method of vaulting quantification. The subject is trying to create as much space as possible for toe clearance during contralateral swing period.

progress angle in the sagittal plane during single support at the point of minimum angular velocity. This can be identified in Fig. 5.14 for the magnitude and location of peak joint power. The clinical tuning showed an overall decrease in vaulting compensation. Table 5.3 shows Controller 1 produced a 6% decrease in this compensation compared to the Baseline controller, while Controller 2 showed a 3% decrease. Both clinician tuned controllers were able to reduce vaulting amount due to more assistance from the powered prosthesis with increase ankle push-off.

Frontal plane range of motion measures pelvic obliquity and hip abduction, which are good metrics for quantifying hip-hiking and circumduction. These are additional strategies to increase toe clearance for a passive leg or lifting the weight of a powered leg [3]. Table 5.3 gives quantified gait pathology metrics for range of motion (ROM) of the hip and pelvic in frontal plane as well as the vaulting amount the subject has taken along the sagittal plane. The non-parenthesis numbers are the average values and the parenthesis numbers are their standard deviation. In Table 5.3, the first controller shows an average decrease in hip motion on both intact and prosthetic sides, while a slight decrease in range for pelvic obliquity on the prosthetic side. The second controller also showed a decrease in hip abduction on the prosthetic side, but increases in pelvic range of motion on both sides. The decreased vaulting along the sagittal plane is accounted for in the second controller by an increased range of motion on the frontal plane.

Table 5.3. Quantifying Gait Pathology

	Hip ROM [deg]		Pelvic ROM [deg]		Vaulting [deg]
	P	I	P	I	I
Baseline	7.09 (0.32)	10.61 (0.74)	7.68 (1.07)	3.35 (0.80)	14.50 (1.57)
Controller 1	5.44 (1.33)	9.06 (1.15)	6.58 (1.25)	3.77 (0.36)	13.61 (2.28)
Controller 2	6.35 (1.24)	12.27 (1.77)	8.14 (2.48)	5.18 (1.26)	14.03 (1.50)

Gait symmetry ratio (SR) is a powerful measurement for identifying gait asymmetry in relation to spatial-temporal parameters. A perfectly symmetrical gait will have a value of unity. A metric with a ratio greater than one favors the prosthetic side and these can be judged by the magnitude of deviation from perfect symmetry

$$SR = \frac{\Upsilon_{Prosthetic}}{\Upsilon_{Intact}},$$

where Υ refers to the spatial-temporal parameter [95]. As shown in Table 5.4, computing SR from step length shows a positive trend from the Baseline of 0.93, to the successive first and second controllers, 0.94 and 1.02, respectively. Stance and swing time also show the progression towards a more symmetrical gait with Baseline controller SR stance time at 1.33, and then Controllers 1 and 2 at 1.28 and 1.23, respectively. The trend towards symmetry continues with swing time: the Baseline and Controller 1 were similar at SR of

0.65 and 0.64, respectively, while Controller 2 greatly improved symmetry with value of 0.73 for a 11.6% improvement.

Another important outcome measure for overall gait pathology is Gait Deviation Index (GDI). GDI is a multivariate metric of gait pathology taken for each side of the subject that accounts for measurements of leg, hip, and pelvic movement [98]. A GDI ≥ 100 reveals an absence of gait abnormality, and every 10 points below a 100 corresponds to a standard deviation away from ideal gait. Measurements of both the prosthesis and intact legs from Vicon, where GDI was computed for each controller concatenating all the strides. All the prosthetic controllers had no significant change, since there were no drastic changes in the joint kinematics between controllers from the clinician adjustments. The intact side had small differences in GDI averages ranging from 76.8 to 80.5. The standard deviation is the highest in the Baseline Controller at 2.98 and reduces as the clinical controllers were used with the lowest value at 1.32 from Controller 2. This conveys that the intact side gait pathology was performing more consistently using Controller 2 compared to the other controllers with smaller variance.

Table 5.4. Overall Gait Performance Evaluation

	GDI		Symmetry Ratios		
	P	I	Step Length [m]	Stance Time [s]	Swing Time [s]
Baseline	75.2 (1.49)	80.5 (2.98)	0.93 (0.01)	1.33 (0.08)	0.65 (0.05)
Controller 1	75.0 (1.53)	76.8 (2.78)	0.94 (0.11)	1.28 (0.06)	0.64 (0.05)
Controller 2	75.2 (1.75)	78.6 (1.32)	1.02 (0.05)	1.23 (0.04)	0.74 (0.09)

5.4 Discussion

5.4.1 Convergence of Spatial-Temporal parameters increases gait fluidity

The clinician controllers had various kinematic strengths that increased the subject's comfort and the fluidity of gait. On the whole, it is easy to see that the strides became smoother because the spatial-temporal parameters converge with each successive, clinician-tuned controller. However, the standard deviation is relatively high because each controller was tested with only two passes across the walkway. The decreasing difference between both sides indicates that the gait is more symmetrical, the subject has more control of walking [76] and the loading of each limb have more even–minimizing pain and joint degeneration [71]. These improvements were achieved by changing the instance and magnitude of push-off to restore healthy locomotor function and energetics during human walking when using a powered prosthesis [110, 121].

5.4.2 Clinical tuning influences limb loading

The vertical GRF seen in the Baseline trial shows a higher loading of the body weight on the intact leg, a common occurrence in unilateral transfemoral amputees [97]. The decrease in intact leg forces between the Baseline and two clinician controllers is a good assessment; Controller 1 gave much improvement in peak GRF on the intact side, but additional trials would be needed to prove significance. On the prosthetic side, the Controller 1 shows acceptable loading, while the Controller 2 skews slightly higher than normal [70]. This is in good agreement with the loading on the intact leg for the second controller. The braking and propulsive forces are predominantly used to determine whether forward momentum is lost during stance period. We are looking for symmetry between braking and propulsive forces to indicate that the gait is smooth for the subject, as that conserves energy. Amputees typically present a smaller propulsive force than the braking force on the prosthetic side and higher on the intact side to compensate. The GRF and force data from this subject follows this trend well within normal ranges [54, 26].

5.4.3 Compensation moves from the ankle to the hip

Upon switching from the subject's take-home passive leg to our powered prosthesis, the subject began to use the active push-off and was able to create the space and propulsion needed without the same degree of vaulting compensation. Due to the unfamiliarity with a powered prosthesis and the brevity of the trial, the subject was letting this propulsion push his pelvis as evidenced by the increased ranges of motion in the frontal plane on the prosthetic side [3]. In comparison, a passive leg with a solid, stiff ankle and a passive knee requires more compensatory action because the foot cannot dorsiflex to allow the passive knee to swing unimpeded; an active push-off from a powered leg should create the energy needed to propel the step instead of using the height of the vault to swing the knee and clear the toe [49]. Though, this may only happen after being acclimated to the leg over a longer period of time than this study allowed. This is evidenced in Fig. 5.13–the final local maximum on the clinical prosthetic side is caused by the push-off not being fully utilized. With further acclimation, the subject might learn to lean into this push-off and decrease compensation.

The increase in pelvic obliquity on the intact side is caused, in most part, by having to leverage a heavier leg as well as the disruptive kinematics of vaulting on the pelvic floor. Increased hip abduction is caused by the weight differential between the subject's take-home leg and our powered leg, the subject seems to be hefting it off the ground and jerking hip with the core instead of fully utilizing the powered push-off due to his unfamiliarity with powered joints in general. We hypothesize that with a longer term study with multiple clinical sessions, these compensations would decrease in the frontal plane as the subject began to walk in a more energy efficient manner. Furthermore, hardware concerns have been identified for this prosthesis in [87], where the actuator torque budget reached near maximum so variance in the amount of ankle and knee torque was limited. Thus, a more significant effect with adjustment to ankle push-off by the clinician controller would be more apparent with a high-torque/low-speed actuator system. Another powered prosthesis design is currently in the works to specifically address this issue [19].

5.4.4 Metrics for overall gait pathology

Though, there are several metrics for determining symmetry, the SR was used for its ease of understanding and its good representation of the data [95]. Each of the spatial-temporal parameters showed movement towards more symmetrical gait as the clinician progressed with adjusting the prosthesis controller. The stance and swing times have the appropriate trends with the stance time favoring the prosthetic leg and swing time favoring the intact leg, but both temporal measures move towards a more symmetric gait from Baseline to Controller 2. These trends can be well explained by two factors. First, the clinical environment and frequent tuning led the subject to spend more time on the prosthetic leg in stance time to fully explore push-off, which amputees lack from their conventional passive leg. Second, the small changes in actuation during the gait cycle, as per swing time, the weight of the leg and the effort exerted to increase clearance are significant factors in shortening the swing time. The convergence of both of these metrics towards a SR of unity is indicative of the clinical tuning to help offset the weight of the leg and ease the compensatory methods as typically required with an amputee's conventional leg.

GDI is particularly important because it takes into account many lower limb joint variables. It is understandable that the values on the prosthetic side are lower than those of the intact leg, but the lower values for the intact leg can be explained by compensatory methods. Vaulting and hip-hiking are unnatural gait pathologies that cause significant deviations and are factors that are included in the overall measure of gait symmetry and fluidity. Finally, more acclimation time beyond one clinical session would be necessary to determine the true significance of powered prostheses on long-term gait pathology [25].

CHAPTER 6

CONCLUSION

This dissertation takes a different approach in terms of controls for powered prostheses from current control schemes using multiple impedance-based controllers to a single, unified controller using method of virtual constraints. The idea of virtual constraints has a significant influence in the field of biped robot controls. Virtual constraints are a phase-based control strategy that have desired joint trajectories parameterized over an unactuated degree of freedom known as a mechanical phase variable. This allows synchronization of kinematic constraints for a multi-joint system, such as a powered knee-ankle prosthesis, driven by a phase variable. The method of virtual constraints for a powered prosthesis was implemented by Discrete Fourier Transformation, which is a polynomial function against a monotonic phase variable over the entire gait cycle. The phase variable is computed from residual thigh motion, giving the amputee control over the timing of the prosthetic joint patterns. This reduced the number of controllers and control parameters to become a "plug-and-play" approach for a powered prosthesis that minimized clinical tuning time and allows this technology to be more readily available in a clinical setting for amputees.

Chapter 2: The current state of control methodology for lower limb powered prostheses is to have multiple switching controllers implemented over discrete periods between the stance and swing period. To go beyond the current status quo, a novel unified controller over the entire gait cycle was developed using virtual constraints encoded by method of Discrete Fourier Transformation parameterized by a phase variable. This phase-based prosthesis controller was validated in simulation for an above-knee amputee biped walker, where various walking speed controllers were accomplished with the biped reaching stable gaits. The simulation results verified the control strategy to eventually be implemented on a powered knee-ankle prosthetic leg.

Chapter 3: To implement novel control strategies on an actual control system, a robotic leg test bed was designed and built. The robotic leg is a two degree of freedom system containing linear actuators with translating rotation at the knee and ankle joints that includes the range of motion required to meet desired human walking. Both joint actuators had specified torque requirements similar to torques an able-bodied human produces for normal walking. The robotic leg was designed to be weight conscious and compact, and it can be worn by able-bodied subjects using a bypass adapter or above-knee amputees with a prosthetic socket. Multiple sensors were integrated onto the robotic leg as feedback signals to the control algorithms. A real-time control architecture and data acquisition using dSPACE was developed for both the unified and piecewise phase-based controllers to handle rhythmic and non-rhythmic motion, respectively. Preliminary experiments of leg benchtop testing and able-bodied experiments were performed in evaluating the control performance prior to achieving experiments with lower limb amputee subjects.

Chapter 4: The overarching goal of this dissertation was to validate the novel control strategy with amputee subjects. Three transfemoral amputee subjects were part of a large experimental study to perform various walking speeds (1.5 to 2.7 miles/hr) and different slopes (-2.5 to +9.0 deg). The virtual constraints were systematically designed for task-specific kinematics and no control gains were required to be tuned between subjects, which reduced configuration time during experiments. A number of kinematic and kinetic results were captured from the amputee subjects using the powered prosthesis that were comparable to normative data for these various ambulation modes.

Chapter 5: Demonstrating clinical feasibility is an ongoing problem with the advancement of control strategies for powered prosthesis. The presented "plug-and-play" control approach with minimal tuning parameters can potentially minimize time for amputees to be fitted and begin walking with a powered prosthesis. Experiments were conducted between a certified prosthetist and a transfemoral amputee, where the prosthetist tuned the prosthesis controller with a clinical interface that adjusts the virtual constraint designs to aid in improving the amputee's gait. Our control scheme explored the capability prosthetists have in meeting their requirements to fitting a powered prosthesis with minimal effort, while allowing immediate adjustments with the leg for any one amputee subject. Many gait outcome metrics were evaluated showing the amputee's gait was improving by way of intervention from the prosthetist adjusting the controller.

To conclude, this dissertation work has encapsulated many concepts and disciplines. Control theory was investigated for a unified phase-based controller using the theoretical derivation of virtual constraints for amputee locomotion. An amputee biped simulator was used to verify the control strategy, and stability analysis was presented prior to real-world application. Mechanical design and manufacturing was involved in developing the actuation system and structure of the powered knee-ankle prosthesis test bed for control development. Electrical and software engineering were applied in the electronic build-up of the robotic leg with motor and sensor integration as well as the controls algorithm software implementation for real-time control. The field of biomechanics and clinical research was adapted with human subject experiments to validate the control strategy. This dissertation has also laid the groundwork for other controls research, such as auto-tuning of control parameters [57] and high-level task-specific control for different ambulation modes [20]. Future work is also needed to make the unified control approach amenable to both rhythmic and non-rhythmic locomotion, which will mitigate the need for two different controllers to achieve both locomotion types. The need to include the clinician's expertise to adjusting prosthetic controllers is important and the research topic can only grow from here. Future work for the CCI would be to incorporate gait pathology feedback information as output results. Potential information to provide could be gait symmetry ratio, GDI, step width, etc. This can aid the prosthetist to make more informative decisions to adjust the prosthetic controller during the clinical session.

APPENDIX A

UTD LEG 1 DESIGN BUILD OF MATERIAL

Table A.1 shows the UTD Leg Build of Material used to manufacture the powered device. Here it provides description of the COTS and the custom machined parts for the powered leg. Key items are listed such as part name, material, quantity, and weight of the components.

Table A.1. UTD Leg 1 Bill of Materials

ITEM NO.	PART NAME	DESCRIPTION	PART NUMBER	VENDOR	MATERIAL	Weight	QTY.	Total Weight
1	SIde Plate UTD	Side Plate	N/A	UTD Machine Shop	6061 Alloy	0.52	2	1.04
2	Joint Base, Ankle UTD	Encoder Joint Base to Side Plates	N/A	UTD Machine Shop	6061 Alloy	0.07	1	0.07
3	Joint Base, Knee UTD	Encoder Joint Base to Side Plates	N/A	UTD Machine Shop	6061 Alloy	0.07	1	0.07
4	Joint, Ankle UTD	Joint Lever Arm	N/A	UTD Machine Shop	7075-O (SS)	0.24	1	0.24
5	Joint, Knee UTD	Joint Lever Arm	N/A	UTD Machine Shop	7075-O (SS)	0.29	1	0.29
6	Joint Base, Ankle UTD	Bearing Joint Base to Side Plates	N/A	UTD Machine Shop	6061-T6 (SS)	0.07	1	0.07
7	Joint Base, Knee UTD	Bearing Joint Base to Side Plates	N/A	UTD Machine Shop	6061 Alloy	0.07	1	0.07
8	Bearing Support Shoulder Bolt UTD	Supports Bearings	N/A	UTD Machine Shop	6061 Alloy	0.02	4	0.08
9	Cross Brace UTD	Supports side plates	N/A	UTD Machine Shop	7075-T6, Plate (SS)	0.03	1	0.03
10	Encoder Mount UTD	Encoder Mount	N/A	UTD Machine Shop	7050-T73510	0	2	0
11	Motor Rail UTD	Holds Motors	N/A	UTD Machine Shop	6061-T6 (SS)	0.05	2	0.1
12	Motor Plate w Rails UTD	Connects Motor to Rail	N/A	UTD Machine Shop	7075-T6, Plate (SS)	0.02	2	0.04
13	Rod End Bearing UTD	Bearing holder for end of ball screw rod	N/A	UTD Machine Shop	6061-T6 (SS)	0.04	2	0.08
14	Sleeve, Knee Ballscrew UTD	Ballscrew Sleeve over rod	N/A	UTD Machine Shop	6061-O (SS)	0.15	1	0.15
15	Sleeve, Ankle Ballscrew UTD	Ballscrew Sleeve over rod	N/A	UTD Machine Shop	6061-O (SS)	0.15	1	0.15
16	Cross Brace and Hard stop UTD	Knee Cross Brace and Hard stop	N/A	UTD Machine Shop	7050-T73510	0.09	1	0.09
17	Hard Stop addition	Additional height to knee hard stop	N/A	UTD Machine Shop	7075-T6, Plate (SS)	0.01	1	0.01
18	Hard Stop rubber	Rubber stop for Knee hard stop	N/A	UTD Machine Shop	Rubber	0	1	0
19	Bearing, Ball Screw Nook compact universal	Ball Screw Journal Bearing	EZBK10-SLB	Nook	Plain Carbon Steel	1.2	2	2.4
20	Ballnut Nook MBN12x2R-3VW	Ballnut	MBN 12x2R-3VW	Nook	Plain Carbon Steel	0.15	2	0.3
21	Ball Screw, Ankle Nook	Ball Screw	PMBS12x2R-3VW/0/T10/00/6K/184/0/S	Nook	Plain Carbon Steel	0.25	1	0.25
22	Ball Screw, Knee Nook	Ball Screw	PMBS12x2R-3VW/0/T10/00/6K/200/0/S	Nook	Plain Carbon Steel	0.25	1	0.25
23	FUTEK Load Cell	Futek Load Cell	LCM200	FUTEK	Plain Carbon Steel	0.06	2	0.12
24	Encoder, Joint US Digital EC35-4000-4-375-H-D-DM-B	EC35 Optical Commutation Kit Encoder	EC35-4000-4-375-H-D-DM-B	US Digital	Plastic	0.02	2	0.04
25	Motor Maxon EC-4pole_30-305013	Maxon EC-4pole 30 30 mm, brushless, 200 Watt	305013	Maxon	Plain Carbon Steel	0.66	2	1.32

Table A.1. Continued UTD Leg 1 Bill of Materials

ITEM NO.	PART NAME	DESCRIPTION	PART NUMBER	VENDOR	MATERIAL	Weight	QTY.	Total Weight
26	Encoder, Motor Maxon ENC16	Maxon Motor Encoder	461214	Maxon	Steel	0.03	2	0.06
27	Motor Controller Copley Controls ADP-090-36	DIGITAL SERVO DRIVE for BRUSHLESS/BRUSH MOTORS	ADP-090-36	Copley Controls	Steel	0.94	2	1.88
28	Bearing, Flanged MCM 4262T170	Type 440C Stainless Steel Flanged	4262T170	McMaster	Stainless Steel (ferritic)	0.01	12	0.12
29	Bushing, 0.25id 0.25lg MCM 91786A200	Bushing 0.25id, 0.25lg	91786A200	McMaster	6061 Alloy	0	4	0
30	lo_rider_v2	Lo Rider Prosthetic Foot	1E57	Octobock	Hexcel AS4C Carbon Fiber	0.77	1	0.77
31	gates_3mr-17s-09	Sprocket, Ankle Driver. 17 Teeth, 9mm belt size	3MR-17S-09	Gates	6061 Alloy	0.02	1	0.02
32	gates_3mr-68s-09	Ankle Sprocket, Driven. 68 Teeth, 9mm belt size	3MR-68S-09	Gates	6061 Alloy	0.27	1	0.27
33	gates_3mr-32s-09	Knee Sprocket, Driven. 32 Teeth, 9mm belt size	3MR-32S-09	Gates	6061 Alloy	0.06	1	0.06
34	gates_3mr-16s-09	Knee Sprocket, Driver. 16 teeth, 9mm belt size	3MR-16S-09	Gates	6061 Alloy	0.02	1	0.02
35	Powergrip GT3 Belts	Timing Belt	165-3MGT-09	Gates	Rubber	0.01	2	0.02
36	Pyramid Adapter FSR rubber	Rubber spacer for FSR device (HARD 70A)	1310N13	McMaster	Rubber	0.02	1	0.02
37	Female Pyramid Adapter	4-hole Pyramid Adapter (standard)	CPR18	Bulldog	Stainless Steel (ferritic)	0.03	1	0.03
38	Male Pyramid Adapter	4-hole Pyramid Adapter (standard)	P2-NH	Bulldog	Stainless Steel (ferritic)	0.03	1	0.03
39	Pyramid Adapter Plate	Pyramid Adapter Plate without center hole (not standard)	N/A	UTD Machine Shop	Stainless Steel (ferritic)	0.05	1	0.05
40	Bumper, Standard MCM 93115K872	Load-Rated Bumper with Threaded Stud	93115k872	McMaster	Rubber	0	3	0
41	Locknut, 0.25x20	Pyramid Adapter Screw Nuts	95615A120	McMaster	Zinc Plated Steel	0.018	8	0.144
42	Shoulder Bolt, 0.25od x 0.5 threadlock MCM 93996A847	Thread-Locking Tight-Tolerance Shoulder Screw	93996A847	McMaster	Plain Carbon Steel	0.014	2	0.028
43	Shoulder Screw, 0.25od x 0.3125 thread loc MCM 93996A838	Thread-Locking Tight-Tolerance Shoulder Screw	93996A838	McMaster	Plain Carbon Steel	0.011	4	0.044
44	Screw, 0.25x0.75L MCM 92220A185	Low-Profile Alloy Steel Socket Head Cap Screw	92220A185	McMaster	Plain Carbon Steel	0.01	5	0.05
45	Sholder Screw, 0.25id 1L MCM 93996A856	Thread-Locking Tight-Tolerance Shoulder Screw	93996A856	McMaster	Plain Carbon Steel	0.021	2	0.042
46	Spacer, 0.25id 0.375od 0.5l MCM 6389K113	Rubber Spacer	6389K113	McMaster	Rubber	0	2	0
47	Bolt, M3X12, Low Profile, MCM 90666A106	Bolt, M3X12, Low Profile, MCM 90666A106	90666A106	McMaster	Plain Carbon Steel	0	8	0
48	Screw, M5x40, LoProfile MCM 93070A133	Low-Profile Alloy Steel Socket Head Cap Screw	93070A133	McMaster	Plain Carbon Steel	0.015	8	0.12
49	Screw, 0.25x20 0.5L MCM 92220A183	Low-Profile Alloy Steel Socket Head Cap Screw	92220A183	McMaster	Plain Carbon Steel	0.01	14	0.14
50	Screw, M3x8L MCM 91290A113	Screw, M3x8L	91290A113	McMaster	Material ¡not specified¿	0	16	0
51	Spacer, 0.10id 0.25od 0.10l	Spacer behind electronics board, 0.1id, 0.25od	6389K113	McMaster	6061 Alloy	0	6	0

APPENDIX B

UTD LEG 1 KINEMATIC ANALYSIS

Fig. B.1 is a schematic of a planar view for UTD Leg 1. Below is derivation to determine the kinematic motion of each joint's lever arm. Constants were measured from the Leg CAD model as shown in Fig. 3.1. This can assist in estimating the torque at each joint produced by the motion of the linear ball screw.

General Variables

L_i = ball screw column length

Θ_i = measured joint angle (Right Hand Rule)

θ_i = inside lever arm angle

α_i = angle between lever arm and force line of action from ball screw

Ankle Constants

$\beta_1 = 16.62°$

$\beta_2 = 18.96°$

$l_1 = 0.200914$ m

$l_2 = 0.060452$ m

Knee Constants

$\beta = -15.33°$

$l_1 = 0.22733$ m

$l_2 = 0.05969$ m

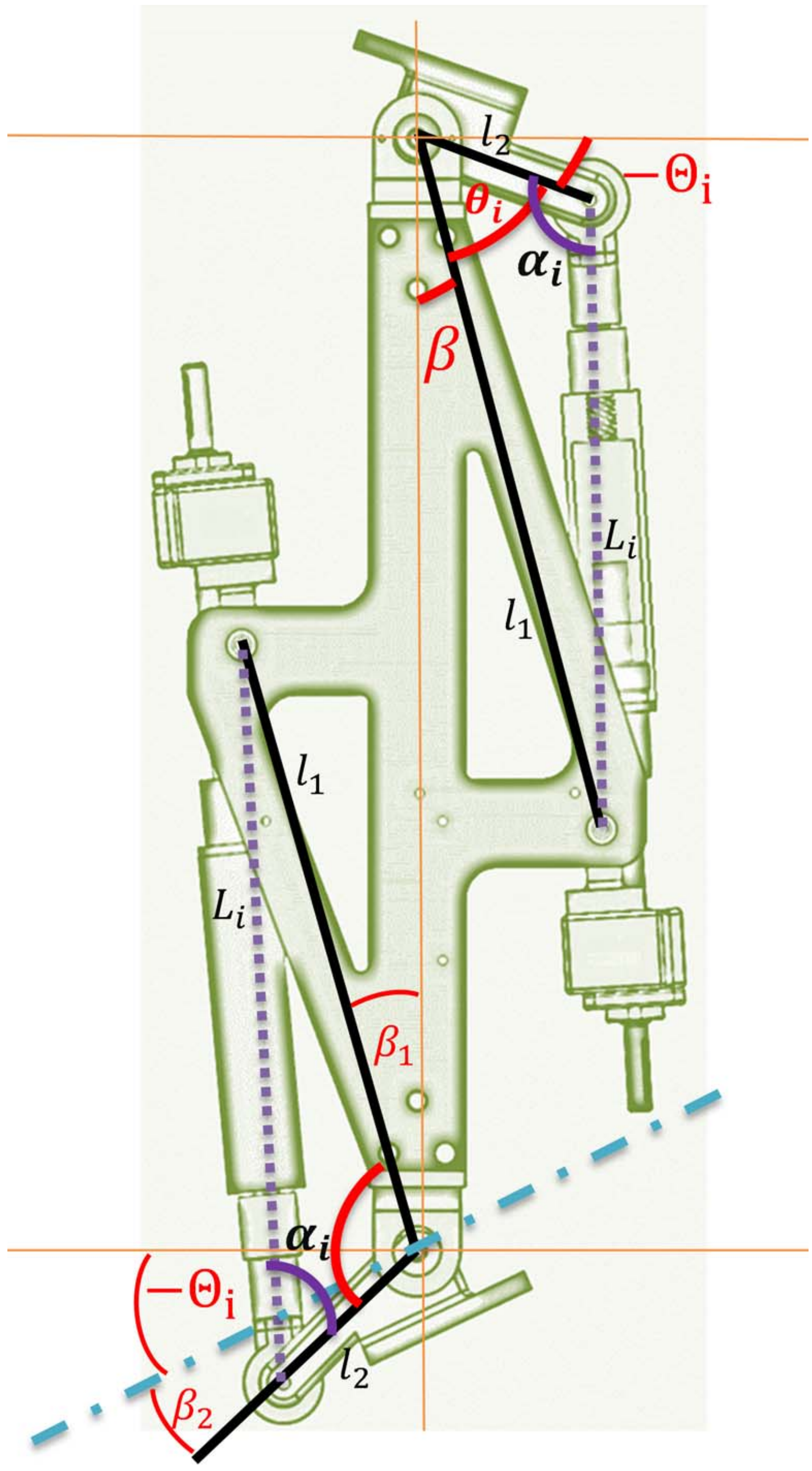

Figure B.1. UTD Leg 1 schematic for declaring mechanism parameters of angles and lengths to derive kinematic equations.

Estimating Joint Torque Derivation

The angle for the ball screw line of action α_i does not have an external sensor to measure. Note, the subscript i depends on the joint where a is for ankle and k is for knee. Applying Law of Cosines for the triangle $l_1 l_2 L_i$ and rearranging terms for obtaining the lever arm angle line of action α_i to give the following form:

$$\begin{aligned} l_1^2 &= L_i^2 + l_2^2 - 2l_2 L_i \cos(\alpha_i) \\ \alpha_i &= \arccos \frac{l_1^2 - L_i^2 - l_2^2}{-2l_2 L_i}. \end{aligned} \tag{B.1}$$

Now substitute L_i^2 from Eq. B.1 to give

$$\alpha_i = \arccos \frac{-2l_2^2 + 2l_1 l_2 \cos\theta_i}{-2l_2\sqrt{l_1^2 + l_2^2 - 2l_1 l_2 \cos\theta_i}}. \tag{B.2}$$

The estimated torque at the joint is

$$T_i = F_L l_2 \sin\alpha_i, \tag{B.3}$$

where F_L is the linear force along the ball screw measured from a uniaxial load cell as described in 3.2.

Ankle Joint Kinematic Derivation

The ankle joint angle can be estimated by the motor input measurement. Comparing angles about the ankle joint

$$\theta_i + \beta_1 = \frac{\pi}{2} - \Theta_i + \beta_2. \tag{B.4}$$

Combining Eqns. B.4 and B.2 to solve for Θ_a gives an estimated function of the ankle joint angle

$$\Theta_a = -\arccos \frac{-L_a^2 + l_1^2 + l_2^2}{2l_1 l_2} + \frac{\pi}{2} + \beta_2 - \beta_1. \tag{B.5}$$

An external sensor is not available for measuring the linear displacement of the ball screw. However, the linear displacement is a direct result of the motor's rotary motion connected to the timing belt. The following are mechanical transmission constants for the ball screw and timing belts.

$P_h = 2$ mm/rev, ball screw lead

$L_{oa} = 0.21209$ m, length of L_a when ankle joint angle is at $0°$

$L_{ok} = 0.21920$ m, length of L_k when knee joint angle is at $0°$

$n_a = 4,$ timing belt sprocket ratio for the ankle

$n_k = 2,$ timing belt sprocket ratio for the knee

The ball screw displacement ΔL is derived from the motor rotary θ_{mi} input to ball screw linear conversion is

$$\Delta L = \theta_{mi} \frac{P_h}{n_i} \tag{B.6}$$
$$\Delta L = L_i - L_{oi},$$

where θ_{mi} is the motor angles per i joint. Solving for L from Eq. B.6 gives a function with variable of motor angle for the travel length of the ball screw as given

$$L_i = \frac{P_h \theta_{mi}}{2\pi n_i} + L_o. \tag{B.7}$$

Substitute Eq. B.7 to B.5 to give a closed form solution of motor angle input to the joint angle output from the actuator system

$$\Theta_a = -\arccos \frac{-(\frac{P_h \theta_{ma}}{2\pi n_a} + L_o)^2 + l_1^2 + l_2^2}{2 l_1 l_2} + \frac{\pi}{2} + \beta_2 - \beta_1. \tag{B.8}$$

Knee Joint Kinematic Derivation

Similar to the ankle, compare angles about the knee joint gives

$$\theta_i + \Theta_i + \beta = -\frac{\pi}{2}. \tag{B.9}$$

Applying to the Law of Cosines to input variable θ_i to give an estimate of the knee joint angle

$$\Theta_k = -\arccos \frac{-L_k^2 + l_1^2 + l_2^2}{2l_1 l_2} - \frac{\pi}{2} - \beta. \tag{B.10}$$

A closed form solution for the knee joint angle can be given by substituting Eq. B.7 to give

$$\Theta_k = -\arccos \frac{-(\frac{P_h \theta_{mk}}{2\pi n_k} + L_o)^2 + l_1^2 + l_2^2}{2l_1 l_2} - \frac{\pi}{2} - \beta. \tag{B.11}$$

APPENDIX C

UTD LEG 1 MATLAB/SIMULINK CONTROL SYSTEM

The following are key subsystem blocks for the UTD Leg 1 control software using MATLAB/Simulink compiled to dSPACE for rapid control development. If shown either the knee or ankle model subsystem, then it is similar to the other respective joint.

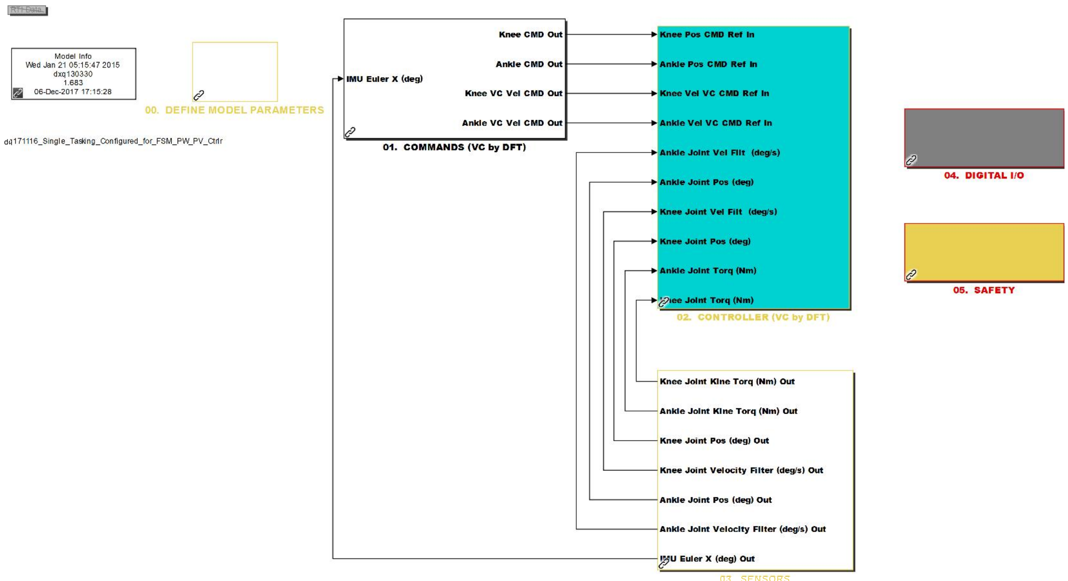

Figure C.1. UTD Leg 1 Control System: Model Main

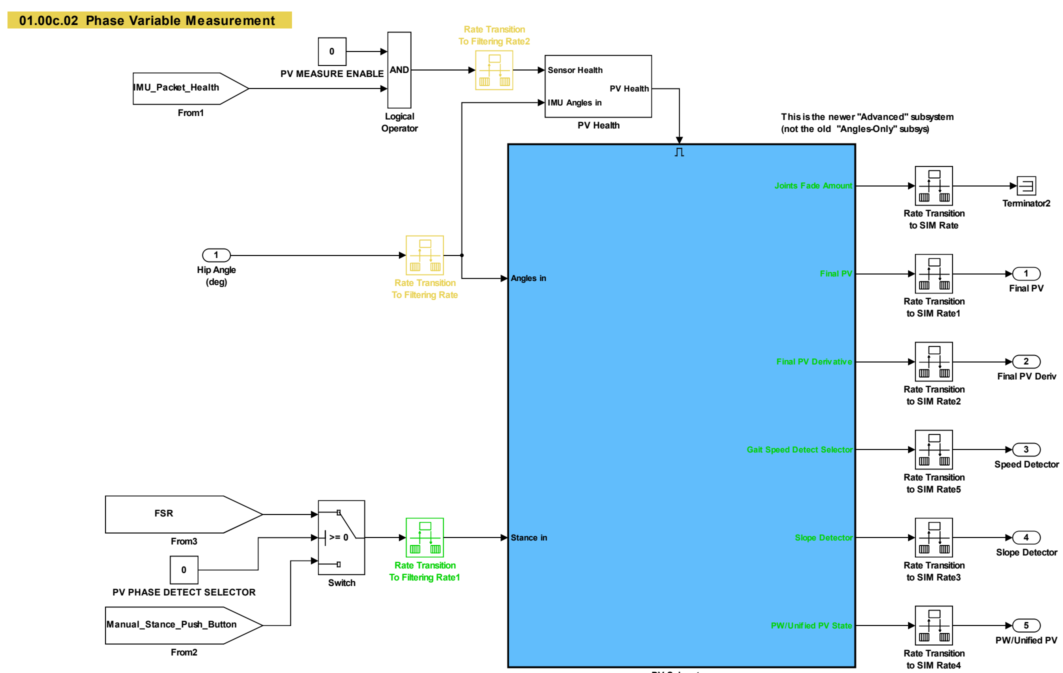

Figure C.2. UTD Leg 1 Control System: Phase Variable Main

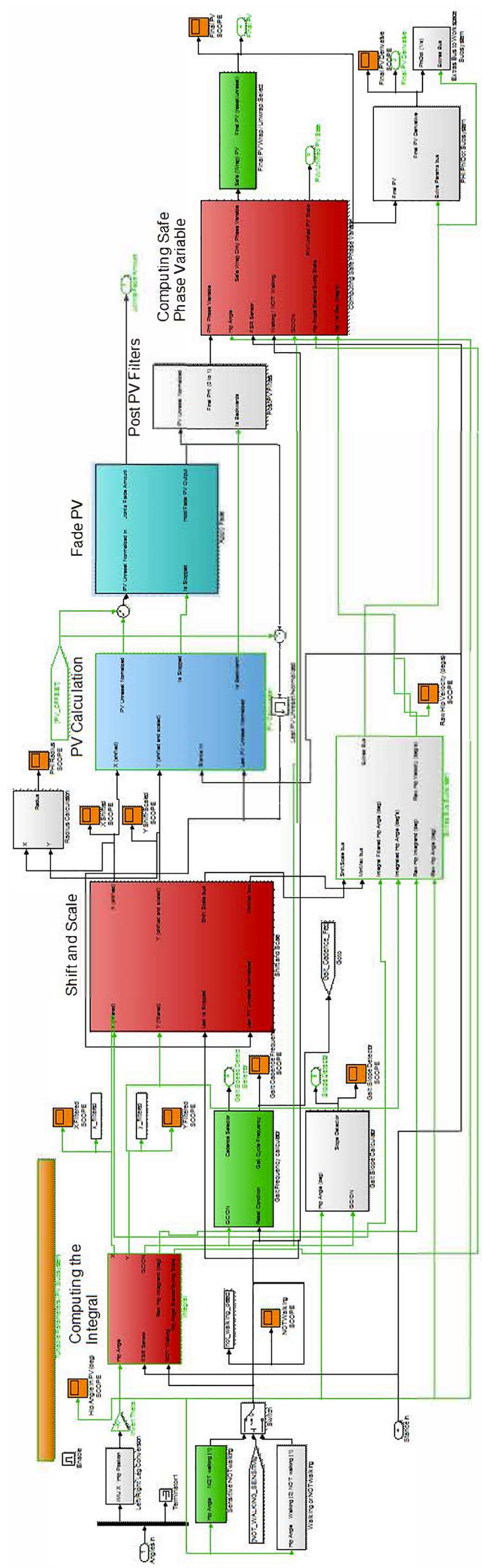

Figure C.3. UTD Leg 1 Control System: Phase Variable Subsystems

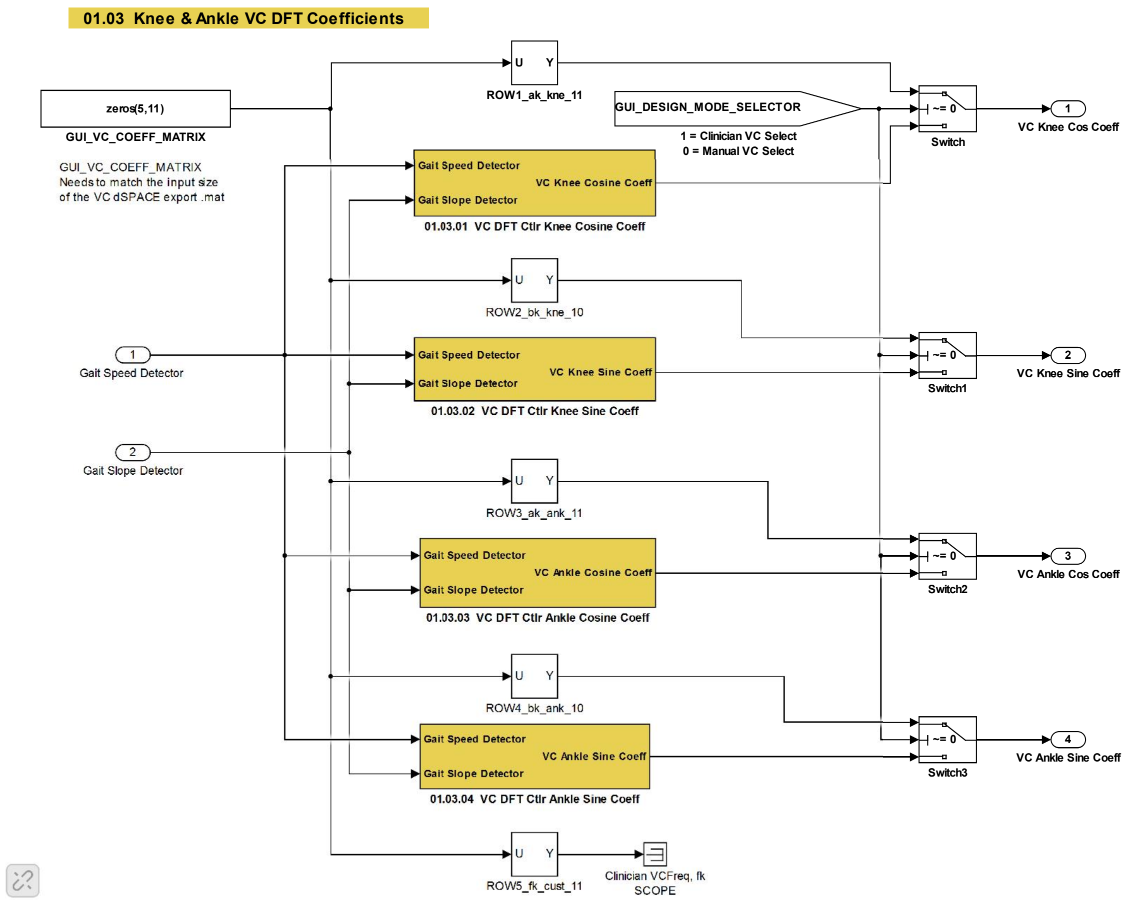

Figure C.4. UTD Leg 1 Control System: Virtual Constraint DFT Coefficients

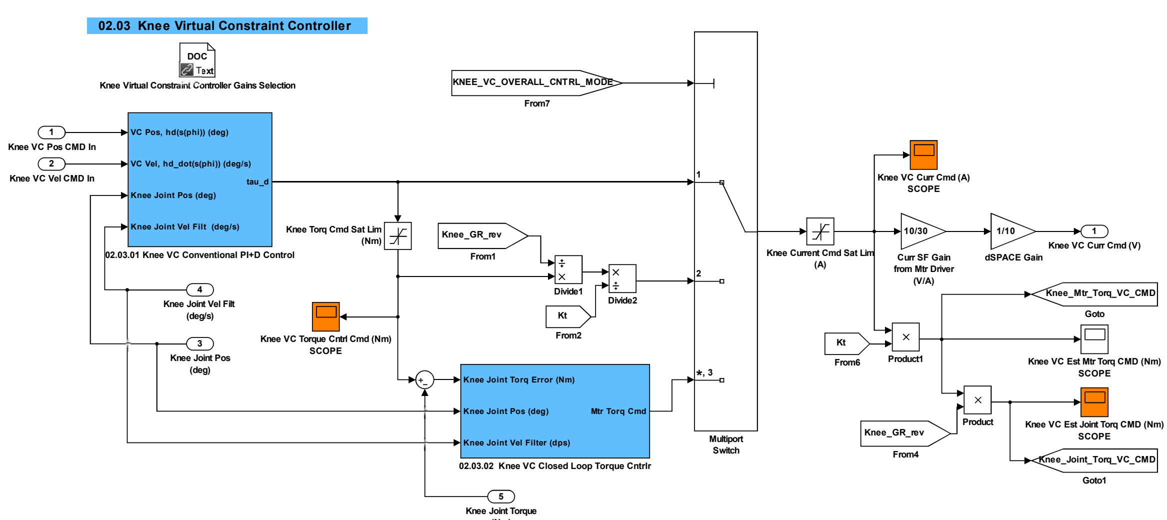

Figure C.5. UTD Leg 1 Control System: Virtual Constraint Outer and Inner Control Loops

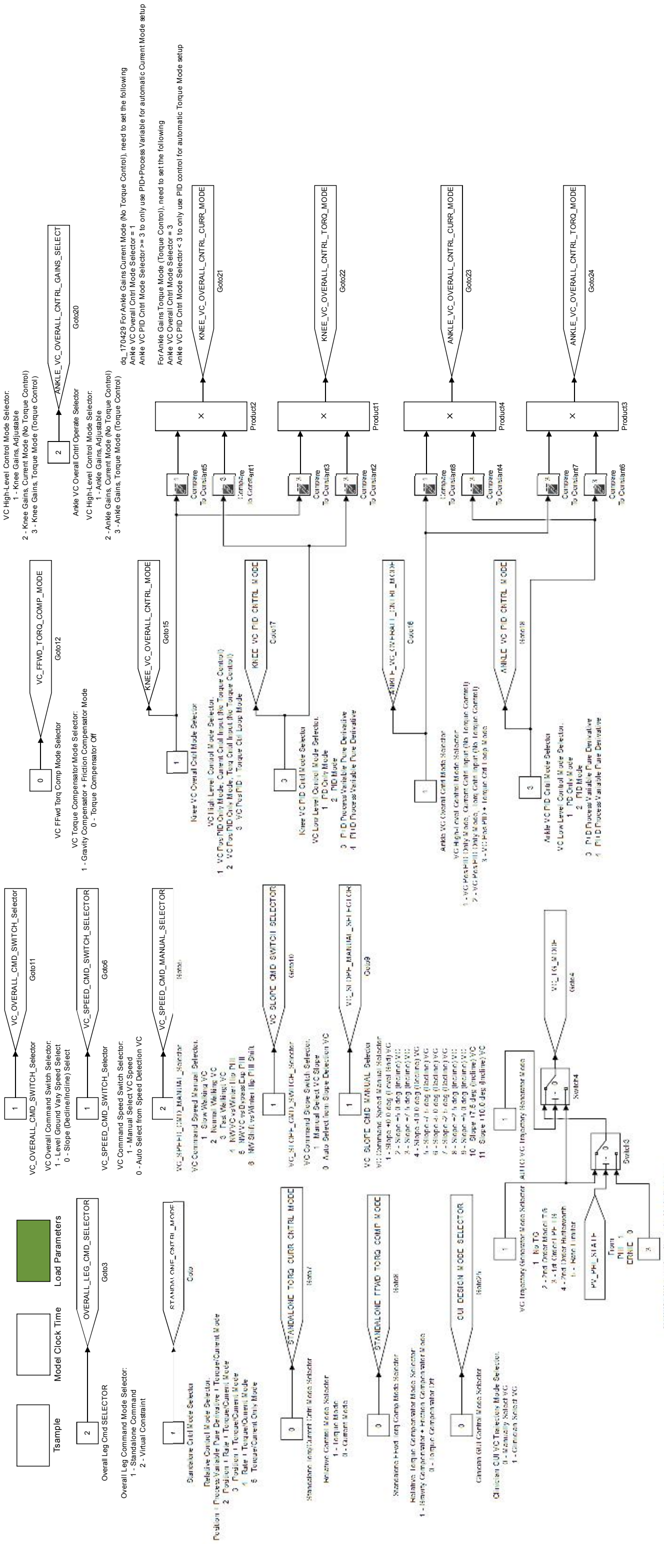

Figure C.6. UTD Leg 1 Control System: User Interface Control Options

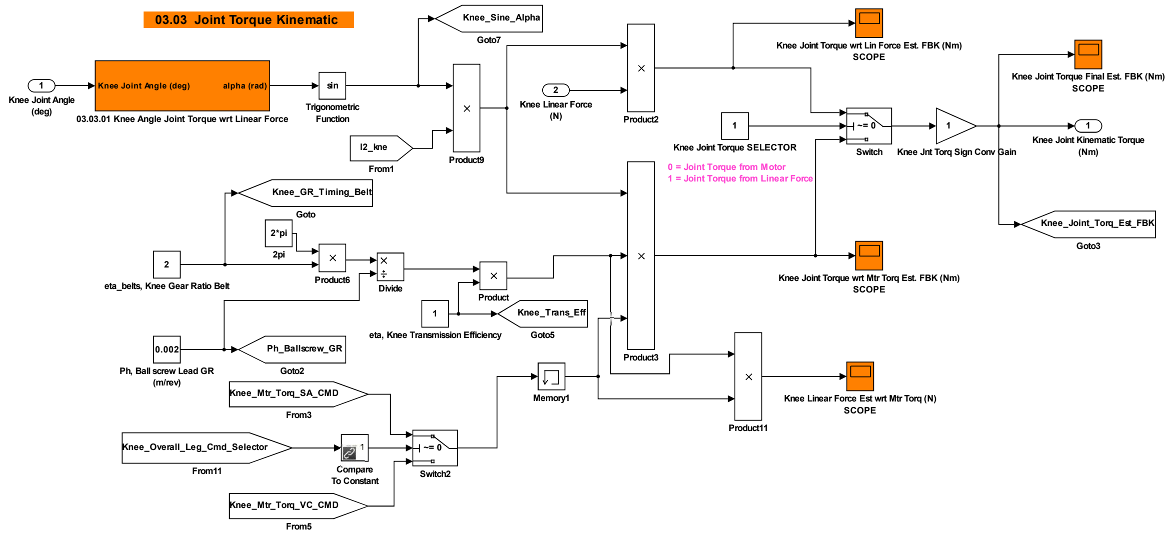

Figure C.7. UTD Leg 1 Control System: Joint Torque Estimation Main

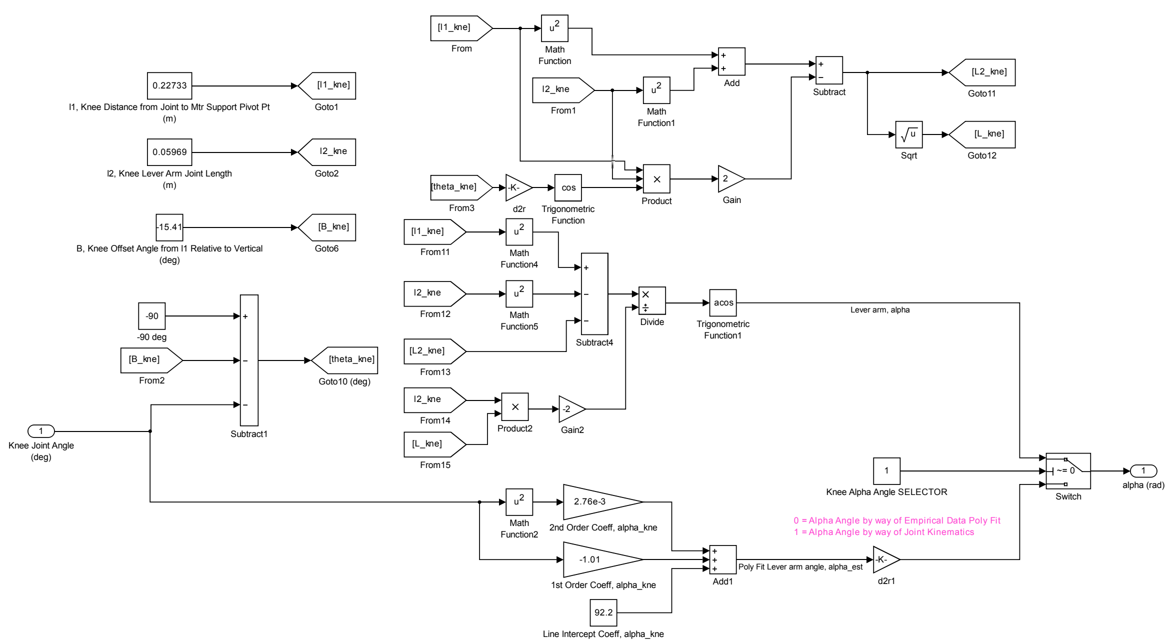

Figure C.8. UTD Leg 1 Control System: Joint Torque Lever Arm Angle Estimate

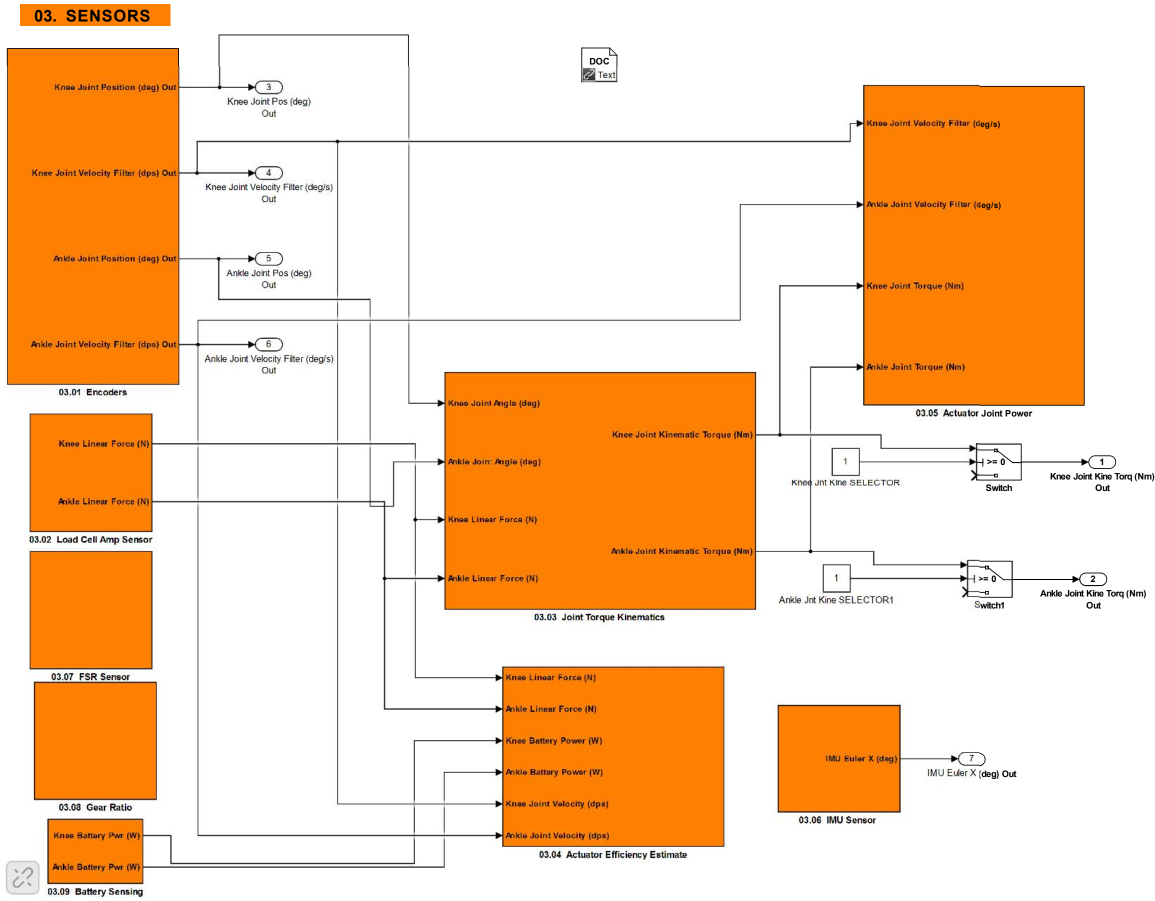

Figure C.9. UTD Leg 1 Control System: Sensors Main

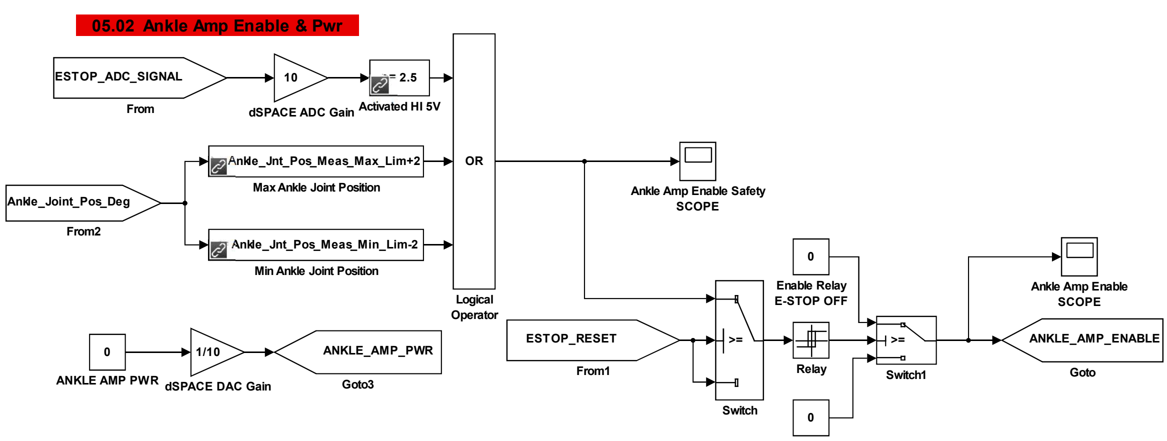

Figure C.10. UTD Leg 1 Control System: Power Safety

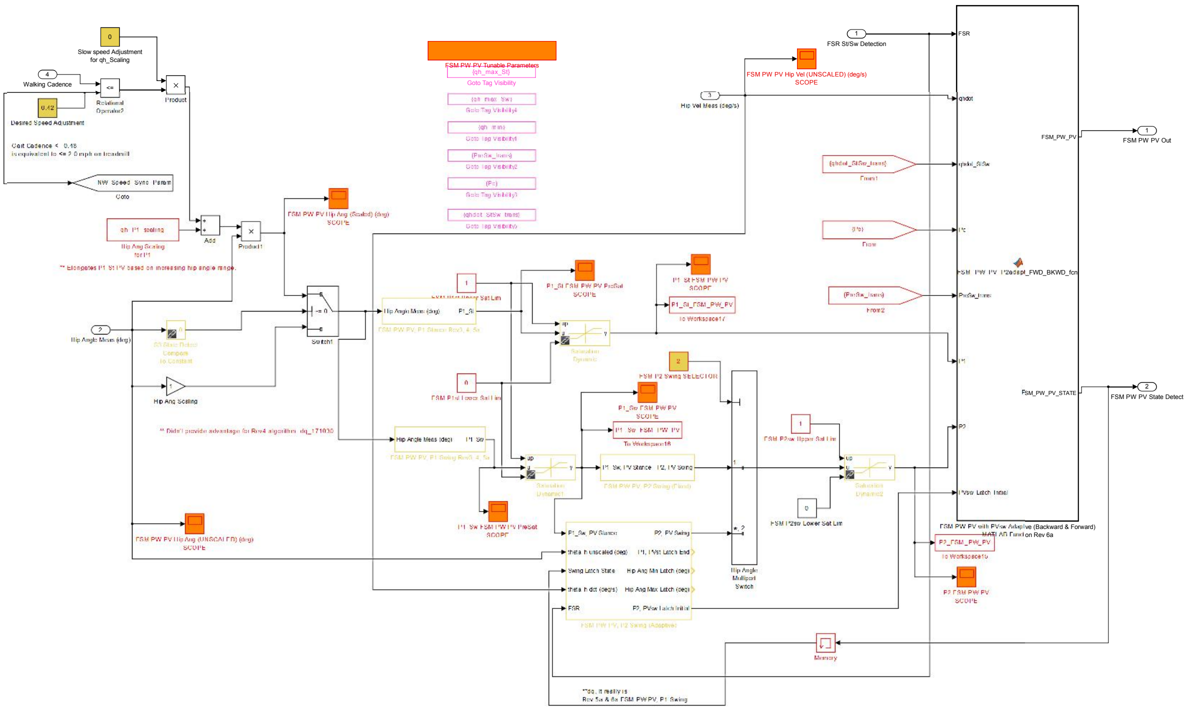

Figure C.11. UTD Leg 1 Control System: Piecewise Phase Variable Finite State Machine

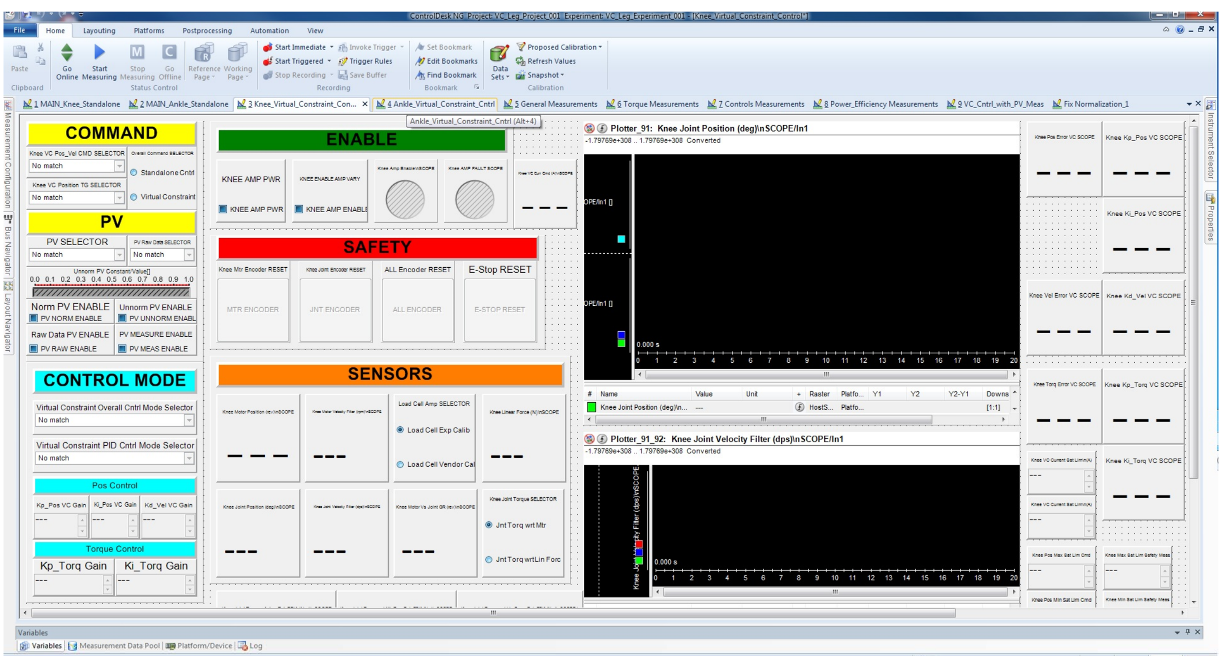

Figure C.12. UTD Leg 1 Control System: dSPACE Control Interface

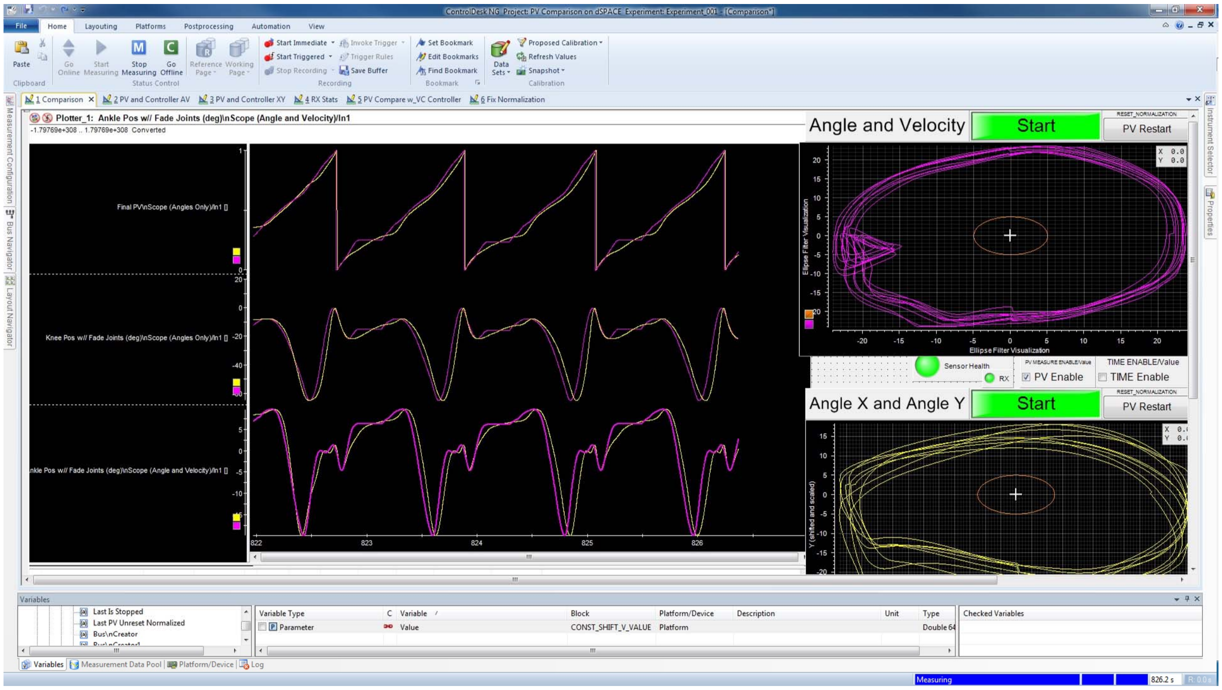

Figure C.13. UTD Leg 1 Control System: dSPACE Measurement Interface

REFERENCES

[1] 1stdibs (2018). Civil War wooden prosthetic leg. https://www.1stdibs.com/furniture/more-furniture-collectibles/collectibles-curiosities/scientific-instruments/pre-civil-war-wood-iron-leather-zinc-prosthetic-leg/id-f_480762/, Accessed: 1 April 2018.

[2] Aghasadeghi, N., H. Zhao, L. Hargrove, A. Ames, E. Perreault, and T. Bretl (2013). Learning impedance controller parameters for lower-limb prostheses. In *IEEE International Conference on Intelligent Robots and Systems*, pp. 4268–4274. IEEE.

[3] Armannsdottir, A., R. Tranberg, G. Halldorsdottir, and K. Briem (2017). Frontal plane pelvis and hip kinematics of transfemoral amputee gait. effect of a prosthetic foot with active ankle dorsiflexion and individualized training–a case study. *Disability and Rehabilitation: Assistive Technology*, 1–6.

[4] Armstrong-Hélouvry, B., P. Dupont, and C. C. De Wit (1994). A survey of models, analysis tools and compensation methods for the control of machines with friction. *Automatica 30*(7), 1083–1138.

[5] ASME.org (2018). The Civil War and the Birth of the U.S Prosthetics Industry. https://www.asme.org/engineering-topics/articles/bioengineering/the-civil-war-and-birth-of-us-prosthetics-industry, Accessed: 1 April 2018.

[6] Au, S. K. and H. Herr (2008). Powered ankle-foot prosthesis. *IEEE Robot. Automat. Mag. 15*(3), 52–59.

[7] Bakker, K., W. H. van Houtum, and P. C. Riley (2005). 2005: The international diabetes federation focuses on the diabetic foot. *Current diabetes reports 5*(6), 436–440.

[8] Bellman, R. D., M. A. Holgate, and T. G. Sugar (2008). Sparky 3: Design of an active robotic ankle prosthesis with two actuated degrees of freedom using regenerative kinetics. In *Proc. IEEE/RAS-EMBS Int. Conf. Biomed. Robot. Biomechatron.*,, pp. 511–516. IEEE.

[9] Burnfield, M. (2010). Gait analysis: normal and pathological function. *Journal of Sports Science and Medicine 9*(2), 353.

[10] Buss, B., A. Ramezani, K. Hamed, B. Griffin, K. Galloway, and J. Grizzle (2014). Preliminary walking experiments with underactuated 3d bipedal robot MARLO. *IEEE/RSJ Int. Conf. Intelli. Robots Sys.*, 2529–2536.

[11] Catmull, E. and R. Rom (1974). A class of local interpolating splines. In *Computer aided geometric design*, pp. 317–326. Elsevier.

[12] Chevallereau, C., G. Abba, Y. Aoustin, F. Plestan, E. Westervelt, C. C. de Wit, and J. Grizzle (2003). Rabbit: A testbed for advanced control theory. *IEEE Control Systems Magazine 23*(5), 57–79.

[13] Cutson, T. M. and D. R. Bongiorni (1996). Rehabilitation of the older lower limb amputee: A brief review. *J. Am. Geriatr. Soc. 44*(11), 1388–1393.

[14] DeVita, P., J. Helseth, and T. Hortobagyi (2007). Muscles do more positive than negative work in human locomotion. *J. Exp. Biol. 210*(19), 3361–3373.

[15] Diop, S., J. Grizzle, and F. Chaplais (2000). On numerical differentiation algorithms for nonlinear estimation. In *IEEE Conf. Decis. Contr.*, Volume 2, pp. 1133–1138. IEEE.

[16] Diop, S., J. Grizzle, P. Moraal, and A. Stefanopoulou (1994). Interpolation and numerical differentiation for observer design. In *Amer. Contr. Conf.*, Volume 2, pp. 1329–1329.

[17] Drevelle, X., C. Villa, X. Bonnet, I. Loiret, P. Fodé, and H. Pillet (2014). Vaulting quantification during level walking of transfemoral amputees. *Clinical Biomechanics 29*(6), 679–683.

[18] Eilenberg, M. F., H. Geyer, and H. Herr (2010). Control of a powered ankle–foot prosthesis based on a neuromuscular model. *IEEE Trans. Neural Sys. Rehab. Eng. 18*(2), 164–173.

[19] Elery, T., S. Rezazadeh, C. Nesler, J. Doan, H. Zhu, and R. Gregg (2018). Design and benchtop validation of a powered knee-ankle prosthesis with high-torque, low-impedance actuators. In *IEEE Int. Conf. Robot. Autom.* Accepted.

[20] Embry, K. R., D. J. Villarreal, and R. D. Gregg (2016). A unified parameterization of human gait across ambulation modes. In *IEEE Int. Conf. Eng. Med. Biol. Soc.*, pp. 2179–2183.

[21] Fletcher, D. D., K. L. Andrews, J. W. Hallett, M. A. Butters, C. M. Rowland, and S. J. Jacobsen (2002). Trends in rehabilitation after amputation for geriatric patients with vascular disease: implications for future health resource allocation. *Arch. Phys. Med. Rehab. 83*(10), 1389–1393.

[22] Freedom Innovation (2017). FS1000 Sierra Prosthetic Foot. `http://www.freedom-innovations.com/sierra/`, Accessed: 2 October 2017.

[23] Fu, A., C. Fu, K. Wang, D. Zhao, X. Chen, and K. Chen (2013). The key parameter selection in design of an active electrical transfemoral prosthesis. In *IEEE International Conference on Robotics and Biomimetics*, pp. 1716–1721. IEEE.

[24] Gailey, R. S., M. A. Wenger, M. Raya, N. Kirk, K. Erbs, P. Spyropoulos, and M. S. Nash (1994). Energy expenditure of trans-tibial amputees during ambulation at self-selected pace. *Prosth. Orth. Int. 18*(2), 84.

[25] Gaunaurd, I., S. E. Spaulding, D. Amtmann, R. Salem, R. Gailey, S. J. Morgan, and B. J. Hafner (2015). Use of and confidence in administering outcome measures among clinical prosthetists: Results from a national survey and mixed-methods training program. *Prosthetics and Orthotics International 39*(4), 314–321.

[26] Gauthier-Gagnon, C., D. Gravel, H. St-Amand, C. Murie, and M. Goyette (2000). Changes in ground reaction forces during prosthetic training of people with transfemoral amputations: A pilot study. *JPO: Journal of Prosthetics and Orthotics 12*(3), 72–77.

[27] Goldfarb, M., B. E. Lawson, and A. H. Shultz (2013). Realizing the promise of robotic leg prostheses. *Science translational medicine 5*(210), 210ps15–210ps15.

[28] Golub, G. H. and C. F. Van Loan (1996). Matrix computations. *Johns Hopkins Universtiy Press, 3rd edtion.*

[29] Goswami, A., B. Thuilot, and B. Espiau (1998). A study of the passive gait of a compass-like biped robot: Symmetry and chaos. *Int. J. Robot. Res. 17*(12), 1282–1301.

[30] Gregg, R. D., Y. Y. Dhaher, A. Degani, and K. M. Lynch (2012). On the mechanics of functional asymmetry in bipedal walking. *IEEE Trans. Biomed. Eng. 59*(5), 1310–1318.

[31] Gregg, R. D., T. Lenzi, N. P. Fey, L. J. Hargrove, and J. W. Sensinger (2013). Experimental effective shape control of a powered transfemoral prosthesis. In *IEEE Int. Conf. Rehab. Robot.*, Seattle, WA.

[32] Gregg, R. D., T. Lenzi, L. J. Hargrove, and J. W. Sensinger (2014). Virtual constraint control of a powered prosthetic leg: From simulation to experiments with transfemoral amputees. *IEEE Transactions on Robotics 30*(6), 1455–1471.

[33] Gregg, R. D., E. J. Rouse, L. J. Hargrove, and J. W. Sensinger (2014). Evidence for a time-invariant phase variable in human ankle control. *PLoS ONE 9*(2), e89163.

[34] Gregg, R. D. and J. W. Sensinger (2013). Biomimetic virtual constraint control of a transfemoral powered prosthetic leg. In *Amer. Contr. Conf.*, pp. 5702–5708.

[35] Grey, M. J., J. B. Nielsen, N. Mazzaro, and T. Sinkjær (2007). Positive force feedback in human walking. *The Journal of physiology 581*(1), 99–105.

[36] Grimmer, M., M. Eslamy, S. Gliech, and A. Seyfarth (2012). A comparison of parallel- and series elastic elements in an actuator for mimicking human ankle joint in walking and running. In *IEEE Int. Conf. Robotics & Automation*, pp. 2463–2470.

[37] Grizzle, J. W., G. Abba, and F. Plestan (2001). Asymptotically stable walking for biped robots: analysis via systems with impulse effects. *IEEE Trans. Automat. Contr. 46*(3), 513–513.

[38] Ha, K. H., H. A. Varol, and M. Goldfarb (2011). Volitional control of a prosthetic knee using surface electromyography. *IEEE Transactions on Biomedical Engineering 58*(1), 144–151.

[39] Hamed, K. and R. D. Gregg (2017). Decentralized feedback controllers for robust stabilization of periodic orbits of hybrid systems: Application to bipedal walking. *IEEE Trans. Control Syst. Tech. 25*(4), 1153–1167.

[40] Hamed, K. A., B. G. Buss, and J. W. Grizzle (2014). Continuous-time controllers for stabilizing periodic orbits of hybrid systems: Application to an underactuated 3D bipedal robot. In *IEEE Conf. Decis. Control*, pp. 1507–1513.

[41] Hanger (2017). Hanger clinic: Empowering human potential. `http://www.hangerclinic.com`, Accessed: 2 October 2017.

[42] Hansen, A. H., D. S. Childress, and E. H. Knox (2000). Prosthetic foot roll-over shapes with implications for alignment of trans-tibial prostheses. *Prosth. Orth. Int. 24*(3), 205–15.

[43] Hansen, A. H., D. S. Childress, and E. H. Knox (2004). Roll-over shapes of human locomotor systems: Effects of walking speed. *Clin. Biomech. 19*(4), 407–14.

[44] Hebenstreit, F., A. Leibold, S. Krinner, G. Welsch, M. Lochmann, and B. M. Eskofier (2015). Effect of walking speed on gait sub phase durations. *Hum. Movement Sci. 43*, 118–124.

[45] Holgate, M. A., T. G. Sugar, and A. Bohler (2009). A novel control algorithm for wearable robotics using phase plane invariants. In *IEEE Int. Conf. Robot. Automat.*, pp. 3845–3850.

[46] Hoover, C. D., G. D. Fulk, and K. B. Fite (2013). Stair ascent with a powered trans-femoral prosthesis under direct myoelectric control. *IEEE/ASME Transactions on Mechatronics 18*(3), 1191–1200.

[47] Huang, H., D. L. Crouch, M. Liu, G. S. Sawicki, and D. Wang (2016). A cyber expert system for auto-tuning powered prosthesis impedance control parameters. *Annals of Biomedical Engineering 44*(5), 1613–1624.

[48] Huang, H., T. A. Kuiken, and R. D. Lipschutz (2009). A strategy for identifying locomotion modes using surface electromyography. *IEEE Trans. Biomed. Eng. 56*(1), 65–73.

[49] Ingraham, K. A., N. P. Fey, A. M. Simon, and L. J. Hargrove (2016). Assessing the relative contributions of active ankle and knee assistance to the walking mechanics of transfemoral amputees using a powered prosthesis. *PloS one 11*(1), e0147661.

[50] Isidori, A. (1995). *Nonlinear Control Systems* (Third ed.). London, England: Springer.

[51] Jaritz, A. and M. W. Spong (1996). An experimental comparison of robust control algorithms on a direct drive manipulator. *IEEE Trans. Control Systems Technology 4*(6), 627–640.

[52] Jolliffe, I. (2002). *Principal Component Analysis*. Wiley Online Library.

[53] Kerestes, J., T. G. Sugar, and M. Holgate (2014). Adding and subtracting energy to body motion: Phase oscillator. In *ASME Int. Design Eng. Tech. Conf. & Comp. and Info. in Eng. Conf.*, pp. V05AT08A004.

[54] Koehler-McNicholas, S. R., R. D. Lipschutz, and S. A. Gard (2016). The biomechanical response of persons with transfemoral amputation to variations in prosthetic knee alignment during level walking. *Journal of rehabilitation research and development 53*(6), 1089.

[55] Kolathaya, S. and A. D. Ames (2012). Achieving bipedal locomotion on rough terrain through human-inspired control. In *Safety, Security, and Rescue Robotics (SSRR), 2012 IEEE International Symposium on*, pp. 1–6. IEEE.

[56] Koller, J. R., D. H. Gates, D. P. Ferris, and C. D. Remy (2016). Body-in-the-loop optimization of assistive robotic devices: A validation study. In *Robotics: Science and Systems Conference*.

[57] Kumar, S., A. Mohammadi, N. Gans, and R. Gregg (2017). Automatic tuning of virtual constraint-based control algorithms for powered knee-ankle prostheses. *IEEE Conf. Contr. Technol. Applicat.*, 812–818.

[58] Lawson, B. E., J. Mitchell, D. Truex, A. Shultz, E. Ledoux, and M. Goldfarb (2014). A robotic leg prosthesis: Design, control, and implementation. *IEEE Robot. Autom. Mag. 21*(4), 70–81.

[59] Lawson, B. E., H. Varol, A. Huff, E. Erdemir, and M. Goldfarb (2013). Control of stair ascent and descent with a powered transfemoral prosthesis. *IEEE Trans. Neural Sys. Rehab. Eng. 21*(3), 466–473.

[60] Lenzi, T., L. Hargrove, and J. Sensinger (2014). Speed-adaptation mechanism: Robotic prostheses can actively regulate joint torque. *IEEE Robot. Automat. Mag. 21*(4), 94–107.

[61] Martin, A. E. and R. D. Gregg (2015). Hybrid invariance and stability of a feedback linearizing controller for powered prostheses. In *Amer. Contr. Conf.*, Chicago, IL, pp. 4670–4676.

[62] Martin, A. E. and R. D. Gregg (2016). Incorporating human-like walking variability in an HZD-based bipedal model. *IEEE Trans. Robotics 32*(4), 943–948.

[63] Martin, A. E. and R. D. Gregg (2017). Stable, robust hybrid zero dynamics control of powered lower-limb prostheses. *IEEE Trans. Autom. Control 62*(8), 3930–3942.

[64] Martin, A. E., D. C. Post, and J. P. Schmiedeler (2014). Design and experimental implementation of a hybrid zero dynamics-based controller for planar bipeds with curved feet. *Int. J. Robot. Res. 33*(7), 988–1005.

[65] Martin, A. E. and J. P. Schmiedeler (2014). Predicting human walking gaits with a simple planar model. *J. Biomech. 47*(6), 1416–21.

[66] MATLAB (2013). *version 8.2.0.701 (R2013b).* Natick, Massachusetts: The MathWorks Inc.

[67] McIntosh, A. S., K. T. Beatty, L. N. Dwan, and D. R. Vickers (2006). Gait dynamics on an inclined walkway. *Journal of biomechanics 39*(13), 2491–2502.

[68] Miller, W. C., A. B. Deathe, M. Speechley, and J. Koval (2001). The influence of falling, fear of falling, and balance confidence on prosthetic mobility and social activity among individuals with a lower extremity amputation. *Arch. Phys. Med. Rehab. 82*(9), 1238–1244.

[69] Nguyen, Q. and K. Sreenath (2015). L1 adaptive control for bipedal robots with control lyapunov function based quadratic programs. In *Amer. Contr. Conf.*, pp. 862–867. IEEE.

[70] Nilsson, J. and A. Thorstensson (1989). Ground reaction forces at different speeds of human walking and running. *Acta Physiologica 136*(2), 217–227.

[71] Nolan, L., A. Wit, K. Dudziñski, A. Lees, M. Lake, and M. Wychowañski (2003). Adjustments in gait symmetry with walking speed in trans-femoral and trans-tibial amputees. *Gait & posture 17*(2), 142–151.

[72] Oppenheim, A. V. and R. W. Schafer (2013). *Discrete-Time Signal Processing* (3 ed.). New York City, NY: Pearson.

[73] Ottobock (2017). C-Leg above-knee prosthetic leg. `https://www.ottobockus.com/c-leg.html`, Accessed: 2 October 2017.

[74] Ottobock (2018). Mechanical above-knee prosthetic leg. `https://www.ottobockus.com/sports/solution-overview/waterproof-prosthetics/`, Accessed: 1 April 2018.

[75] Park, H.-W., A. Ramezani, and J. Grizzle (2013). A finite-state machine for accommodating unexpected large ground-height variations in bipedal robot walking. *IEEE Transactions on Robotics 29*(2), 331–345.

[76] Patterson, K. K., W. H. Gage, D. Brooks, S. E. Black, and W. E. McIlroy (2010). Evaluation of gait symmetry after stroke: a comparison of current methods and recommendations for standardization. *Gait & posture 31*(2), 241–246.

[77] Perry, J. and J. Burnfield (2010). *Gait Analysis: Normal and Pathological Function.* Thorofare, New Jersey: Slack-Incorporated.

[78] Peterson, C. L., S. A. Kautz, and R. R. Neptune (2011). Braking and propulsive impulses increase with speed during accelerated and decelerated walking. *Gait & posture 33*(4), 562–567.

[79] Pfeifer, S., A. Pagel, R. Riener, and H. Vallery (2015). Actuator with angle-dependent elasticity for biomimetic transfemoral prostheses. *IEEE/ASME Transactions on Mechatronics 20*(3), 1384–1394.

[80] Pieringer, D. S., M. Grimmer, M. F. Russold, and R. Riener (2017, July). Review of the actuators of active knee prostheses and their target design outputs for activities of daily living. In *IEEE Int. Conf. Rehab. Robot.*, pp. 1246–1253.

[81] Pillai, M. V., H. Kazerooni, and A. Hurwich (2011). Design of a semi-active knee-ankle prosthesis. In *Robotics and Automation (ICRA), 2011 IEEE International Conference on*, pp. 5293–5300. IEEE.

[82] Pratt, G. A., M. M. Williamson, P. Dillworth, J. Pratt, and A. Wright (1997). Stiffness isn't everything. In *Experimental Robotics IV*, pp. 253–262. Springer.

[83] Preece, S. J., J. Y. Goulermas, L. P. Kenney, D. Howard, K. Meijer, and R. Crompton (2009). Activity identification using body-mounted sensorsa review of classification techniques. *Physiological Measurement 30*(4), R1–R33.

[84] Quintero, D., D. J. Lambert, D. J. Villarreal, and R. D. Gregg (2017). Real-time continuous gait phase and speed estimation from a single sensor. *IEEE Conference on Control Technology and Applications*, 847–852.

[85] Quintero, D., A. E. Martin, and R. D. Gregg (2018). Towards unified control of a powered prosthetic leg: A simulation study. *IEEE Transactions on Control Systems Technology 26*(1), 305–312.

[86] Quintero, D., D. J. Villarreal, and R. D. Gregg (2016). Preliminary experiments with a unified controller for a powered knee-ankle prosthetic leg across walking speeds. In *IEEE Int. Conf. Intelli. Robots Sys.*, pp. 5427–5433.

[87] Quintero, D., D. J. Villarreal, D. J. Lambert, S. Kapp, and R. D. Gregg (2018). Continuous-phase control of a powered knee-ankle prosthesis: Amputee experiments across speeds and inclines. *IEEE Transactions on Robotics*. Accepted.

[88] Rabuffetti, M., M. Recalcati, and M. Ferrarin (2005). Trans-femoral amputee gait: Socket–pelvis constraints and compensation strategies. *Prosthet. Orthot. Int. 29*(2), 183–192.

[89] Ramezani, A., J. Hurst, K. Hamed, and J. Grizzle (2013). Performance analysis and feedback control of ATRIAS, a three-dimensional bipedal robot. *ASME J. Dyn. Sys. Meas. Control 136*(2), 021012.

[90] Renzi, R., N. Unwin, R. Jubelirer, and L. Haag (2006). An international comparison of lower extremity amputation rates. *Ann Vasc Surg 20*(3), 346–350.

[91] Research News @Vanderbilt, Michael Goldfarb's Center for Intelligent Mechatronics Laboratory (2013). Robotic advances promise artificial legs that emulate healthy limbs. `https://news.vanderbilt.edu/2013/11/07/robotic-legs-healthy-limbs/`, Accessed: 1 April 2018.

[92] Rossignol, S., R. Dubuc, and J.-P. Gossard (2006). Dynamic sensorimotor interactions in locomotion. *Physiological Reviews 86*(1), 89–154.

[93] Rouse, E. J., L. M. Mooney, and H. M. Herr (2014). Clutchable series-elastic actuator: Implications for prosthetic knee design. *The International Journal of Robotics Research 33*(13), 1611–1625.

[94] Sabatini, A. M., C. Martelloni, S. Scapellato, and F. Cavallo (2005). Assessment of walking features from foot inertial sensing. *IEEE Trans. Biomed. Eng. 52*(3), 486–494.

[95] Sadeghi, H., P. Allard, F. Prince, and H. Labelle (2000). Symmetry and limb dominance in able-bodied gait: a review. *Gait & posture 12*(1), 34–45.

[96] Sanderson, D. J. and P. E. Martin (1997). Lower extremity kinematic and kinetic adaptations in unilateral below-knee amputees during walking. *Gait & Posture 6*(2), 126–136.

[97] Schaarschmidt, M., S. W. Lipfert, C. Meier-Gratz, H.-C. Scholle, and A. Seyfarth (2012). Functional gait asymmetry of unilateral transfemoral amputees. *Human movement science 31*(4), 907–917.

[98] Schwartz, M. H. and A. Rozumalski (2008). The gait deviation index: a new comprehensive index of gait pathology. *Gait & posture 28*(3), 351–357.

[99] Shultz, A. H., B. E. Lawson, and M. Goldfarb (2015). Running with a powered knee and ankle prosthesis. *IEEE Trans. Neural Sys. Rehab. Eng. 23*(3), 403–412.

[100] Simon, A. M., K. A. Ingraham, N. P. Fey, S. B. Finucane, R. D. Lipschutz, A. J. Young, and L. J. Hargrove (2014). Configuring a powered knee and ankle prosthesis for transfemoral amputees within five specific ambulation modes. *PLoS ONE 9*(6), e99387.

[101] Smith, D., J. Michael, and J. Bowker (Eds.) (2004). *Atlas of Amputations and Limb Deficiencies: Surgical, Prosthetic, and Rehabilitation Principles.* Rosemont, IL: American Academy of Orthopaedic Surgeons.

[102] Sreenath, K., H.-W. Park, I. Poulakakis, and J. W. Grizzle (2011). A compliant hybrid zero dynamics controller for stable, efficient and fast bipedal walking on MABEL. *Int. J. Robot. Res. 30*(9), 1170–1193.

[103] Staros, A. (1957). The sach (solid-ankle cushion-heel) foot. *Ortho Pros Appl J*, 23–31.

[104] Sup, F., A. Bohara, and M. Goldfarb (2008). Design and control of a powered transfemoral prosthesis. *Int. J. Robot. Res. 27*(2), 263–273.

[105] Sup, F., H. A. Varol, and M. Goldfarb (2011). Upslope walking with a powered knee and ankle prosthesis: initial results with an amputee subject. *IEEE Trans. Neural Sys. Rehab. Eng. 19*(1), 71–78.

[106] Sup, F., H. A. Varol, J. Mitchell, T. J. Withrow, and M. Goldfarb (2009a). Preliminary evaluations of a self-contained anthropomorphic transfemoral prosthesis. *IEEE/ASME Transactions on Mechatronics 14*(6), 667–676.

[107] Sup, F., H. A. Varol, J. Mitchell, T. J. Withrow, and M. Goldfarb (2009b). Self-contained powered knee and ankle prosthesis: initial evaluation on a transfemoral amputee. In *IEEE Int. Conf. Rehab. Robot.*, pp. 638–644.

[108] Thatte, N. and H. Geyer (2016). Toward balance recovery with leg prostheses using neuromuscular model control. *IEEE Trans. Biomed. Eng. 63*(5), 904–913.

[109] Tucker, M. R., J. Olivier, A. Pagel, H. Bleuler, M. Bouri, O. Lambercy, J. del R Millán, R. Riener, H. Vallery, and R. Gassert (2015). Control strategies for active lower extremity prosthetics and orthotics: a review. *J. Neuroeng. Rehabil. 12*(1).

[110] Tzu-wei, P. H., K. A. Shorter, P. G. Adamczyk, and A. D. Kuo (2015). Mechanical and energetic consequences of reduced ankle plantar-flexion in human walking. *Journal of Experimental Biology 218*(22), 3541–3550.

[111] Varol, H., F. Sup, and M. Goldfarb (2010). Multiclass real-time intent recognition of a powered lower limb prosthesis. *IEEE Trans. Biomed. Eng. 57*(3), 542–551.

[112] Villarreal, D. and R. Gregg (2016). Unified phase variables of relative degree two for human locomotion. *IEEE Int. Conf. Eng. Med. Biol. Soc.*, 6262–6267.

[113] Villarreal, D. J., H. Poonawala, and R. D. Gregg (2017). A robust parameterization of human joint patterns across phase-shifting perturbations. *IEEE Trans. Neural Sys. Rehab. Eng. 25*(3), 265–278.

[114] Villarreal, D. J., D. Quintero, and R. D. Gregg (2017). Piecewise and unified phase variables in the control of a powered prosthetic leg. In *IEEE Int. Conf. Rehab. Robot.* IEEE.

[115] Westervelt, E. R., J. W. Grizzle, C. Chevallereau, J. H. Choi, and B. Morris (2007). *Feedback Control of Dynamic Bipedal Robot Locomotion.* Boca Raton, Florida: CRC Press.

[116] Winter, D. (1991). *Biomechanics and Motor Control of Human Gait* (2 ed.). Ontario: University of Waterloo Press.

[117] Wu, M., T. Driver, S.-K. Wu, and X. Shen (2014). Design and preliminary testing of a pneumatic muscle-actuated transfemoral prosthesis. *Journal of Medical Devices 8*(4), 044502.

[118] Yang, T., E. Westervelt, A. Serrani, and J. P. Schmiedeler (2009). A framework for the control of stable aperiodic walking in underactuated planar bipeds. *Autonomous Robots 27*(3), 277.

[119] Young, A. J., A. M. Simon, N. P. Fey, and L. J. Hargrove (2014). Intent recognition in a powered lower limb prosthesis using time history information. *Annals of Biomedical Engineering 42*(3), 631–641.

[120] Zehr, E., T. Komiyama, and R. Stein (1997). Cutaneous reflexes during human gait: electromyographic and kinematic responses to electrical stimulation. *J Neuropsychol 77*(6), 3311–3325.

[121] Zelik, K. E. and P. G. Adamczyk (2016). A unified perspective on ankle push-off in human walking. *Journal of Experimental Biology 219*(23), 3676–3683.

[122] Zhang, F., M. Liu, and H. Huang (2015a). Effects of locomotion mode recognition errors on volitional control of powered above-knee prostheses. *IEEE Transactions on Neural Systems and Rehabilitation Engineering 23*(1), 64–72.

[123] Zhang, F., M. Liu, and H. Huang (2015b). Investigation of timing to switch control mode in powered knee prostheses during task transitions. *PLOS one 10*(7), e0133965.

[124] Zhang, J., P. Fiers, K. A. Witte, R. W. Jackson, K. L. Poggensee, C. G. Atkeson, and S. H. Collins (2017). Human-in-the-loop optimization of exoskeleton assistance during walking. *Science 356*(6344), 1280–1284.

[125] Zhao, H., J. Horn, J. Reher, V. Paredes, and A. D. Ames (2017). First steps toward translating robotic walking to prostheses: a nonlinear optimization based control approach. *Autonomous Robots 41*(3), 725–742.

[126] Zhu, H., J. Doan, C. Stence, G. Lv, T. Elery, and R. Gregg (2017). Design and validation of a torque dense, highly backdrivable powered knee-ankle orthosis. In *IEEE Int. Conf. Robot. Autom.*

[127] Ziegler-Graham, K., E. J. MacKenzie, P. L. Ephraim, T. G. Travison, and R. Brookmeyer (2008). Estimating the prevalence of limb loss in the united states: 2005 to 2050. *Arch. Phys. Med. Rehab. 89*(3), 422–429.

[128] Zmitrewicz, R. J., R. R. Neptune, J. G. Walden, W. E. Rogers, and G. W. Bosker (2006). The effect of foot and ankle prosthetic components on braking and propulsive impulses during transtibial amputee gait. *Archives of physical medicine and rehabilitation 87*(10), 1334–1339.

BIOGRAPHICAL SKETCH

David Quintero received his B.S. degree in Mechanical Engineering with a Minor in Mathematics from Texas A&M University, College Station in 2006. He went on to complete his M.S. degree in Mechanical Engineering at Stanford University in 2008. In the meantime, he spent a few years as a robotics and controls engineer in industry before returning to pursue his M.S. and Ph.D. degrees at The University of Texas at Dallas in Mechanical Engineering.

CURRICULUM VITAE

David Quintero

EDUCATION:

The University of Texas at Dallas
Ph.D., Mechanical Engineering, 2018
M.S., Mechanical Engineering, 2016

Stanford University
M.S., Mechanical Engineering, 2008

Texas A&M University
B.S., Mechanical Engineering, 2006

PUBLICATION:

Peer-Reviewed Journal Articles

Quintero, D., Villarreal, D. J., Lambert, D. J., Kapp, S., and Gregg, R. D., "Continuous-Phase Control of a Powered Knee-Ankle Prosthesis: Amputee Experiments Across Speeds and Inclines," IEEE Transactions on Robotics, accepted, 2018.

Quintero, D., Martin A. E., and Gregg, R. D., "Towards Unified Control of a Powered Prosthetic Leg: A Simulation Study," IEEE Transactions on Control Systems Technology, vol. 26, pp. 305–312, 2018.

Villarreal, D. J., **Quintero, D.**, and Gregg, R. D., "A Perturbation Mechanism for Investigations of Phase-Dependent Behavior in Human Locomotion," IEEE Access, vol. 4, pp. 893-904, 2016.

Peer-Reviewed Conference Papers

Quintero, D., Lambert, D. J., Villarreal, D. J., and Gregg, R. D., "Real-Time Continuous Gait Phase and Speed Estimation from a Single Sensor," IEEE International Conference on Control Technology and Applications, 2017.

Villarreal, D. J., **Quintero, D.**, and Gregg, R. D., "Piecewise vs. Unified Phase Variables in the Control of a Powered Prosthetic Leg," IEEE International Conference on Rehabilitation Robotics, 2017.

Quintero, D., Villarreal, D. J., and Gregg, R. D., "Preliminary Experiments with a Unified Controller for a Powered Knee-Ankle Prosthetic Leg Across Walking Speeds," IEEE International Conference on Intelligent Robots and Systems, 2016.

Quintero, D., Martin A. E., and Gregg, R. D., "Unifying the Gait Cycle in the Control for a Powered Knee-Ankle Prosthetic Leg," IEEE International Conference on Rehabilitation Robotics, 2015.

Villarreal, D. J., **Quintero, D.**, and Gregg, R. D., "A Perturbation Mechanism for Investigations of Phase Variables in Human Locomotion," IEEE International Conference on Robotics and Biomimetics, 2015.

Conference Abstracts

Quintero, D., Martin A. E., and Gregg, R. D., "Giving Up the Finite State Machine in the Control of Lower-Limb Wearable Robots?," IEEE Conference on Robotics & Automation, 2015.